ISSN 2435-1288

Nikon Research Report

Vol.5 2023

Purpose of publication

This publication is being created to widely introduce the achievements of research and development activities conducted by Nikon Corporation. This is a result of R&D based on Nikon's core technologies of "opto-electronics" and "precision" technologies that have been incorporated in new products and/or often valued by external organizations such as academic societies.

Foreword

Representative Director
President

Toshikazu Umatate

We are facing various challenges in an unsettled world. Amid this global context, we aspire to offer solutions that are conducive to realizing a sustainable world, not just for our customers but also for society and the environment.

In April 2022, we announced our Medium-Term Management Plan with our Vision 2030 - becoming “a key technology solutions company in a global society where humans and machines co-create seamlessly.” To achieve this, we continue to steadfastly strengthen our main businesses in imaging and precision equipment, while simultaneously pushing forward commercialization and scaling of our strategic businesses in healthcare, components, and digital manufacturing. Through these businesses, we will strive to meet society’s expectations with “trust” and contribute to society with our “creativity.”

With this report, we hope to give you a glimpse of the technology development taking place in Nikon. This includes product development for ongoing businesses, key foundational technologies for the future, environmentally-conscious materials processing technologies, and more.

Executive Fellow
General Manager
Advanced Technology
Research & Development Division

Masaaki Doi

In these times of rapid change and unpredictability, technology development is expected to be more diverse, adaptive, and rapid than ever. At Nikon, our R&D teams are constantly exercising our ingenuity, striving to meet the diversifying needs of our customers and bring our 2030 Vision to life. We are starting to see tangible fruits of our ongoing efforts in technology development, especially in the strategic domains of business, defined in our Medium-Term Management Plan.

With a focus on technological developments in these strategic domains, we have put together technical descriptions of products launched or announced as well as subjects covered in papers published and well-received at conferences during fiscal year 2022. Continuing our tradition, we are delighted to share these achievements from Nikon Group’s R&D once again this year. While this annual report captures only a fraction of the technologies developed at Nikon, I hope it will help you get acquainted with what we do here at Nikon and give Nikon’s technology momentum to further benefit society and the environment.

Nikon Research Report Vol.5
目次／ CONTENTS

技術解説/Technical Reports

1 燃費改善，CO_2 排出量削減を実現する，航空機向けリブレット技術の開発
小野明人，懸田隆史
Development of Riblet Technology for Aircraft to Improve Fuel Efficiency and Reduce CO_2 Emissions
Akito ONO and Takafumi KAKEDA

7 大規模歪に対応した Roll-to-Roll マスクレス露光装置の開発
堀　正和，内藤一夫，中野貴之，伊倉良幸，橋場成史，鬼頭義昭
Development of Roll-to-Roll Maskless Exposure System for Large-Scale Pattern Deformation
Masakazu HORI, Kazuo NAITO, Takayuki NAKANO, Yoshiyuki IGURA, Seiji HASHIBA and Yoshiaki KITO

16 SPPC アレイ検出器を用いた共焦点超解像イメージング
大川潤也，小森谷大介，楠井雄太
Confocal Super-Resolution Imaging using SPPC Array Detector
Junya OHKAWA, Daisuke KOMORIYA and Yuta KUSUI

24 産業用カメラ「LuFact」シリーズの開発
笹井義史，大河内潤，中野雅弘，吉岡玄史，金丸謙介，本　佳弥，近藤俊介
Development of Industrial Camera “LuFact” Series
Yoshifumi SASAI, Jun OKOCHI, Masahiro NAKANO, Genshi YOSHIOKA, Kensuke KANAMARU, Yoshiya MOTO and Shunsuke KONDO

研究開発論文/Research and Development Reports

28 ガスタービン用 TBC へのレーザー加工によるリブレット形成と熱サイクル耐久性評価
綿引健二，蘆田憲一，土橋晋太郎，土橋広和
Riblet Patterning by Laser Ablation on the Thermal Barrier Coating (TBC) for Gas Turbines and Evaluation of Its Resistance to Cyclic Heating
Kenji WATAHIKI, Kenichi ASHIDA, Shintaro TSUCHIHASHI and Hirokazu TSUCHIHASHI

34 広角ダブレットメタレンズに於ける誘電体メタサーフェス素子の種類の違いによる影響
鳥羽英光，髙木英嗣，大橋道雄，大滝　桂，瀧川雄一
Influence on Wide-Angle Doublet Metalenses Due to Different Types of All-Dielectric Metasurfaces
Hidemitsu TOBA, Hidetsugu TAKAGI, Michio OHASHI, Katsura OTAKI and Yuichi TAKIGAWA

46 スポーツフィールドにおける自己校正を使った観客の注視領域推定
阿部和広，髙山侑也，大坪洋介，小池哲也
Estimating Attention Area of Spectator using Self-calibration in Sports Fields
Kazuhiro ABE, Yuuya TAKAYAMA, Yosuke OTSUBO and Tetsuya KOIKE

52 リアルタイムシステム同定法に基づくモデル構築（制御系の異常検知に適したモデル構築手法の提案）
箱田文彦
Model Construction Based on Real-Time System Identification Method (Proposal of a Model Construction Method for Anomaly Detection of Control Systems)
Fumihiko HAKODA

58 プロセス機能展開表を活用した光学ガラスの溶解技術開発
佐藤幸太，嘉指伸一
Development of Optical Glass Melting Technology using a Process Task Visualization Chart
Kota SATO and Shinichi KAZASHI

技術解説

Technical Reports

燃費改善，CO_2 排出量削減を実現する，航空機向けリブレット技術の開発

小野明人，懸田隆史

Development of Riblet Technology for Aircraft to Improve Fuel Efficiency and Reduce CO_2 Emissions

Akito ONO and Takafumi KAKEDA

リブレットはサメ肌構造を模した生物模倣技術の一種であり，流体機器表面の流線に沿って設けられた微細な溝により，乱流境界層の粘性抵抗が低減することが知られている．これを輸送機器や回転機器に応用することにより，その燃費改善や CO_2 排出量削減を実現することができる．とりわけ表面積が大きく高レイノルズ数領域で乱流摩擦抵抗の寄与が大きな航空機においては，実用化に向けた取り組みが盛んに進められているが，いまだ本格的な実用化には至っていない．我々は，レーザーによるリブレット施工技術を開発し，その実用化を目指している．本稿では，航空機へのリブレット技術適用に向けた我々の取り組みについて紹介する．

Riblets are a type of biomimetic technology with shark-skin structure. Riblets reduce the skin friction in a turbulent boundary layer due to the fine grooves provided along the streamlines on the surface of objects in fluids. Applying this technology to transportation and rotating devices, for example, can improve fuel efficiency and reduce CO_2 emissions. For aircraft in particular, where the surface area is large and the contribution of skin friction is significant at high Reynolds number, efforts to practical use of riblets are actively progressing. However, this is yet to be achieved. We have developed a riblet processing technology using laser and our goal is to put it into practical use. In this paper, we introduce our efforts towards the application of riblet technology to the aircrafts.

Key words リブレット，レーザー加工，粘性抵抗低減，CO_2 排出量削減，航空機
riblet, laser processing, drag reduction, CO_2 emissions reduction, aircraft

1 Introduction

In the context of high-speed movements, such as aircraft, resistance is categorized into pressure drag (inertial drag) and frictional drag (viscous drag). In turbulent conditions with high Reynolds numbers, a powerful hairpin vortex forms within the wall boundary layer. Simultaneously, a continuous longitudinal vortex emerges close to the wall owing to a structure known as a low-speed streak. In this scenario, a substantial wall turbulent frictional drag arises, surpassing that of laminar flow. Minimizing this frictional drag to enhance aircraft energy efficiency poses a major challenge [1]. Notably, fast-swimming sharks are known to possess small longitudinal grooves, approximately 35–100 μm in size, on the surface of their scales [2], [3]. These grooves, known as riblets, run parallel to the flow direction. Experiments have demonstrated that these riblets can lead to a remarkable 8–10% decrease in turbulent frictional drag compared to a smooth surface [4]. Moreover, riblets efficiently separate longitudinal vortices from the walls and suppress wall interactions [5]. Fig. 1 shows a schematic diagram of the interaction between riblets and longitudinal vortices. The dimensions of the longitudinal vortices near the wall depend on the wall shear stress. Hence, the optimum riblet pitch (the interval between the tops of the riblet ridges) depends on the wall shear stress, with a larger wall shear stress resulting in a smaller optimum riblet pitch. The reduction in frictional drag owing to riblets depends on

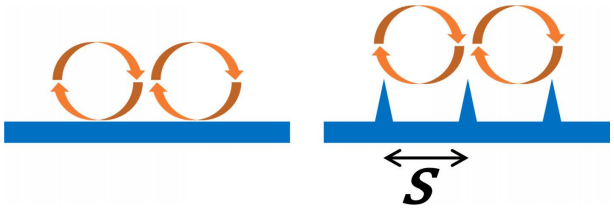

Fig. 1 Eddy-wall interaction without and with riblets. The flow is in the depth direction of the paper.

the dimensions of the longitudinal vortex, specifically the flow velocity. This effect is most pronounced when considering the dimensionless riblet pitch s^+, where s represents the riblet pitch. The maximum reduction in frictional drag occurs when s^+ is around 17, as shown in the following equation:

$$s^+ = \frac{s\sqrt{\frac{\tau_w}{\rho}}}{\nu} \quad (1)$$

where τ_w is the wall shear stress, ρ is the density of the fluid, and ν is the kinematic viscosity of the fluid. Therefore, as the flow velocity decreases or the riblet pitch becomes smaller, the reduction in frictional drag gradually diminishes, eventually reaching zero. Conversely, with an increase in flow velocity or a larger riblet pitch, the effect of reducing the frictional drag decreases, and furthermore, the frictional drag increases when compared to the state without riblets. This behavior is illustrated in Fig. 2 [6]. Research on riblets is advancing in various fields, including aircraft and wind turbine blades. Owing to their extensive surface area, these surfaces significantly influence turbulent frictional drag in high Reynolds number environments [7], [8]. Moreover, the effectiveness of riblets extends to applications in turbomachinery such as industrial compressors and jet engines [9]-[11]. The optimum riblet pitch for civil aircraft flight conditions is approximately 100 μm, roughly equivalent to a human hair's thickness.

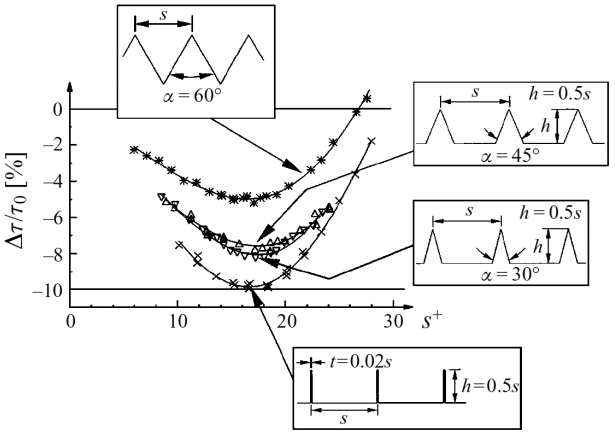

Fig. 2 Drag reduction effect by riblets with various cross section. The number s^+ is a dimensionless riblet size.

2 Aircraft and riblets

The impact of riblets on aircraft has garnered prolonged interest, prompting ongoing technical developments. Notably, Boeing and Airbus conducted real-world tests in the 1990s [7]. However, despite these efforts, the technology has not yet achieved widespread practical implementation owing to challenges related to feasibility and longevity. Viscous drag accounts for over 50% of the aerodynamic drag during transonic cruising flights [12]. Riblets may reduce viscous drag by approximately 6%. If riblet treatment covers 80% of the fuselage surface, a total drag reduction of approximately 2% may be achieved. Moreover, if applied across an entire fleet of aircraft for a major domestic airline, riblet treatment may facilitate an annual jet fuel saving of 95,000 tons, equating to an estimated fuel cost reduction of 8 billion yen and a decrease in CO_2 emissions by 300,000 tons per year. This is equivalent to an average annual fuel cost reduction effect of tens of millions of yen per aircraft. In the context of the growing emphasis on achieving carbon neutrality, riblet processing stands out as an environmentally friendly technology. Another key benefit of riblet techniques is their adaptability, as riblet films or direct surface processing can be applied to existing aircraft, allowing for retrofits.

Bringing riblet technology to real-world aviation applications necessitates a careful equilibrium between workability, aerodynamic efficacy, and durability. Nikon is actively engaged in collaborative partnerships with research institutions, airlines, and other companies to advance the development of these technologies. In the subsequent sections, we will introduce our initiatives addressing each of these critical technical aspects.

3 Workability

The operating profit generated through riblet technology factors in the reduction in fuel consumption relative to the construction costs. Hence, maintaining reasonable construction expenses is crucial. Furthermore, extended aircraft downtime leads to substantial operational losses. As a result, ensuring swift riblet processing is crucial, especially for large-sized or high-surface-area objects.

The current practical implementation of riblet films requires approximately two weeks for application, accompanied by a cost in the tens of millions of yen. This emphasizes the need for efficient methods that minimize downtime and cost.

We successfully developed a technology for forming riblets of a predetermined shape using laser ablation to achieve large-surface area processing for aircraft. Laser ablation is a technology that non-thermally removes material from the surface of a material by using an ultra-short pulse laser with a pulse width of nanoseconds, picoseconds, or femtoseconds [13], [14].

Fig. 3 shows a schematic diagram of riblet processing using laser ablation. Laser riblet processing involves focusing a laser beam to a few dozen micrometers using an $f\theta$ lens and applying it to a workpiece. This causes rapid melting, vaporization, and removal of the irradiated material. Using a galvanometer mirror to swiftly scan the beam spot in the riblet direction, precise riblet shapes can be created with specific dimensions and depths.

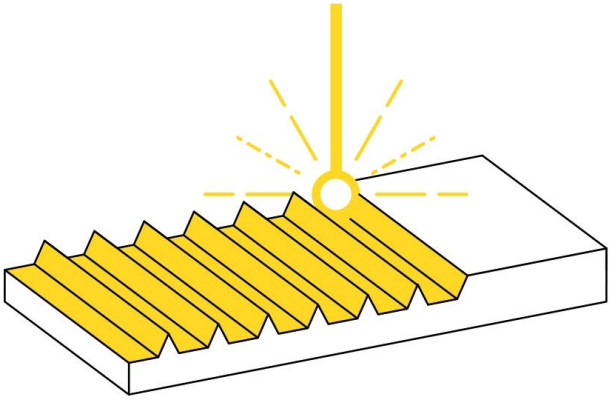

Fig. 3 Schematic diagram of a laser processing for forming riblets on the surface of an object

Laser riblet processing offers several advantages.

For example, highly accurate removal processing can be achieved on various materials such as paints, films, and metals by selecting the optimum laser light source (e.g., wavelength, power, pulse width).

Devising the scan pattern of the galvanometer mirror enables the creation of various riblet shapes. Computational fluid dynamics (CFD) is a valuable tool for designing riblets, allowing for the generation of straight-line riblets and optimized streamlines, as depicted in Fig. 4. This approach enables the creation of not only traditional trapezoidal groove riblets but also advanced next-generation riblets that offer improved efficiency and performance.

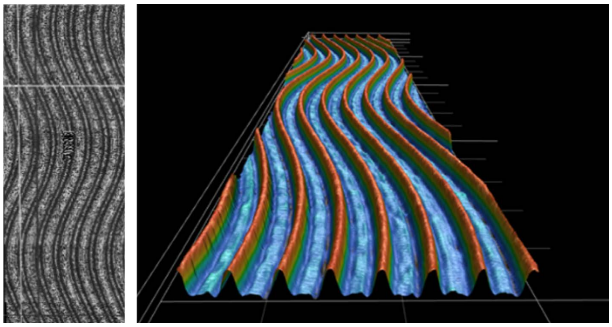

Fig. 4 Smooth curved riblets generated by laser processing

Furthermore, there is substantial flexibility in the shape of the workpiece for processing, allowing riblet formation to be aligned with the specific object's geometry. This is realized by strategically designing an optimal processing path that follows the contour of the curved workpiece surface. By simultaneously guiding the laser beam along this path and continuously adjusting the focal point, precise riblet processing can be achieved. Fig. 5 shows an example of riblet processing for complex shapes.

Fig. 5 Riblet processing on a 3D curved surface

Laser ablation induces minimal thermal impact, ensuring that riblet processing preserves the inherent material durability, including coatings and films, without compromising material quality. This characteristic allows for the retention of long-term riblet effects, even in components with extended replacement cycles. Moreover, laser processing offers a non-contact approach to the workpiece without exerting any reaction force, making it highly compatible with automation. Utilizing a large-scale manipulator in tandem with a laser processing head allows for autonomous control, enabling the processor to independently approach the aircraft and execute riblet processing automatically (Fig. 6). We are currently developing various elemental technologies intending to achieve large-surface area riblet processing using a laser.

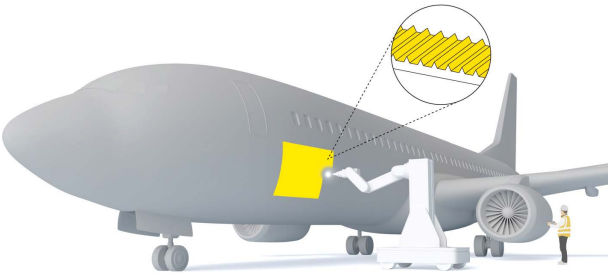

Fig. 6 Conceptual diagram of riblet processing on a large object

We are currently making significant progress in developing an optical system for the laser processing head that significantly enhances the processing speed of existing riblet processors. The conventional optical system, which relies on a single laser beam like many laser processing machines,

faces limitations in removal volume per unit time and processing speed. To address this issue, we are actively engaged in developing a technology that utilizes multiple beams for riblet processing. Our ultimate aim is to utilize this technology to achieve riblet processing for an entire aircraft, such as a Boeing 737–800, within a single day.

Ensuring processing accuracy at the scale of a few micrometers necessitates effective vibration mitigation strategies. When performing riblet processing on an aircraft fuselage within a maintenance area using a processor combining a large manipulator and laser processing head, vibrations from the environment can be amplified by the manipulator, leading to relative vibrations between the processing head and the fuselage. This presents a potential risk of compromising processing accuracy. Therefore, we are currently conducting a vibration response analysis of the manipulator using floor vibration data collected at the maintenance area and are studying the optimal configuration of the manipulator. Moreover, we are developing an active vibration isolation system that cancels relative vibration (Fig. 7).

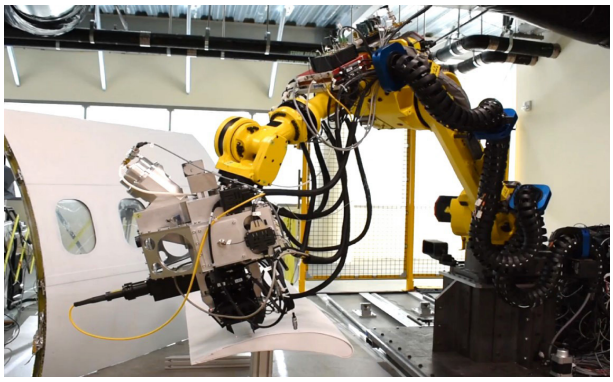

Fig. 7 Riblet processing technology development for large objects

4 Aerodynamic performance evaluation (Wind tunnel test)

The effectiveness of riblet processing in reducing fuel consumption is closely linked to the aerodynamic performance achieved. This performance relies on factors like riblet shape, accuracy, application locations, and coverage areas. Researchers have extensively investigated riblet shapes that combine high effectiveness with strong workability and durability [15], [16]. Shape accuracy has also received significant attention, with both experimental and analytical studies delving into the implications of deviations from the ideal shape [17].

Efforts have also been directed towards advanced CFD analysis techniques that enable the optimization of riblet shapes tailored to specific locations. This is particularly crucial for maximizing the impact of riblets in areas where their effects are most pronounced. Concurrently, advancements in processing technologies are being pursued to facilitate extensive and precisely shaped riblet application across wide surface areas. A study has indicated that if riblet processing can be employed on any part of an aircraft's surface, the main wing exhibits a more significant drag reduction effect per unit of riblet processing area compared to the fuselage [18].

Nikon has partnered with the Japan Aerospace Exploration Agency (JAXA) to validate the drag reduction benefits of laser-engraved riblets. Collaboratively, JAXA has designed a specific riblet shape, which Nikon has then realized using laser processing techniques. The evaluation of the resulting drag reduction effect is being carried out within JAXA's wind tunnel facility (Fig. 8). The assessment employs velocity distribution measurements within the boundary layer, using a Pitot rake for data collection. Moreover, we are currently verifying the effects of next-generation high-efficiency riblet shapes designed by JAXA using direct numerical simulation (DNS). To date, we have confirmed that the conventional trapezoidal grooved riblets have a drag reduction effect of at least 5%, and we are working to improve the riblet shape accuracy to further improve this effect.

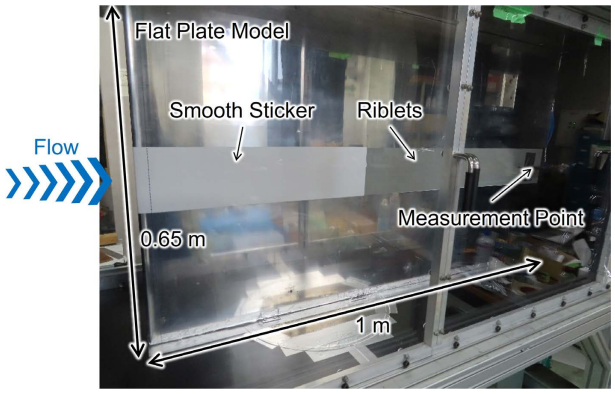

Fig. 8 Riblets on the flat plate model installed in the wind tunnel test section

5 Durability evaluation (Flight test)

As mentioned in the previous section, the aerodynamic performance of riblets is known to be influenced by their specific shape. Consequently, the long-term enhancement in fuel efficiency hinges on the riblet's ability to maintain its original shape throughout the aircraft's operational environment. The conditions to which fuselage riblets are exposed are uniquely challenging. Operating at an altitude of 10,000 meters, the aircraft reaches speeds around 900 km/h while enduring temperatures as low as −50°C and intense ultravio-

let radiation. In addition to environmental factors, the fuselage encounters pollutants like oil, engine exhaust, and debris, as well as the impacts of takeoff and landing. The aircraft's surface must also withstand regular washings. To assess riblet durability under these real-world conditions, we are conducting flight demonstrations in collaboration with two major domestic airlines and JAXA.

Starting in October 2022, Nikon and All Nippon Airways Co., Ltd. (ANA) have initiated operational tests on two Boeing 787 aircraft (JA871A for international flights and JA874A for domestic flights) equipped with riblet films on their surfaces. These flights aim to assess the films' durability by periodically measuring their shape. ANA is the first Japanese airline to operate aircraft with riblet films. Using Nikon's laser technology, six 155 mm square riblet film sheets were applied on each aircraft in key areas like the "vicinity of the base of the main wing" and "upper surface of the fuselage," where air currents are prominent during flight. This trial involves a total of 12 sheets (Fig. 9). Over the coming years, we will gather extensive data from long-term operations and undertake continuous verification, including assessing the riblet film's durability. Notably, no significant shape changes were observed even after 100 days from the riblet installation (JA871A: January 2023, JA874A: March 2023).

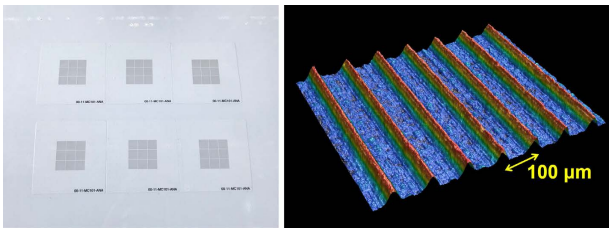

Fig. 9 Riblet film attached to the fuselage and its surface shape

Furthermore, starting in October 2022, Nikon, in collaboration with Japan Airlines Co., Ltd. (JAL) and JAXA, initiated the world's first flight demonstration test using an aircraft where riblets are directly applied to the coating surface of the outer panel using laser technology. JAXA, focused on riblet shapes, leveraged Nikon's laser processing expertise to drive the application of riblets to actual aircraft, leveraging the JAL Group's operational and painting knowledge. We employed Nikon's laser processing technology on a Boeing 737–800 aircraft (JA334J) and applied 75 mm square riblets on both sides of the fuselage's bottom service panel (Fig. 10). Durability flight tests were conducted, involving periodic shape measurements. As of April 2023, more than 150 days have passed since installation, and we confirmed no significant shape changes owing to flight. For this evalulation, Nikon developed a portable laser processing machine for riblet processing on service panels at airport maintenance areas. We conducted essential evaluations, including coating film adhesion, aesthetics, and heat damage tests, using samples from this processor, confirming no adverse impact on the coating film due to laser processing. Based on this outcome, Boeing has provided positive feedback, indicating no technical concerns about fuselage application.

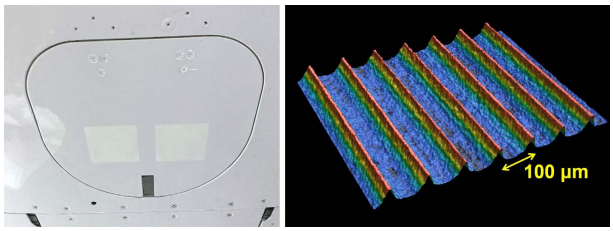

Fig. 10 Riblet application area (2 locations) and its surface shape

6 Conclusion

Nikon has been actively pursuing the application of riblet technology to aircraft and other objects. Leveraging our advanced laser processing technology, we are capable of directly implementing riblets on various surfaces, including those of aircraft and turbine blades, to enhance energy efficiency. Our approach also encompasses the installation of riblet-processed films to further reduce energy loss. Looking ahead, Nikon envisions a future where optical and laser processing strengths converge to enable autonomous processors to seamlessly engage in riblet processing for large structures like aircraft and wind turbine blades. Our commitment extends to the development of business solutions driven by riblet processing, contributing to the realization of a sustainable society through enhanced fuel efficiency and reduced CO_2 emissions.

References

[1] Y. Miyake, "Vortices in near wall turbulence," (in Japanese), *Nagare*, vol. 22, no. 1, pp. 29–34, 2003.

[2] Y. Suzuki and N. Kasagi, "Intelligent active control of wall turbulence," (in Japanese), *Savemation Review*, *Special Issue on Micro Flow Sensor*, pp. 50–57, 2001.

[3] D. W. Bechert, G. Hoppe and W.-E. Reif, "On the drag reduction of shark skin," in Proc. *23rd Aerospace Sciences Meeting*, 1985, doi: 10.2514/6.1985-546.

[4] D. W. Bechert, M. Bartenwerfer, G. Hoppe and W.-E. Reif, "Drag reduction mechanisms derived from shark skin," in *Proc. 15th Congr. ICAS*, Sep.1986, pp. 1044–1068.

[5] B. Dean and B. Bhushan, "Shark-skin surfaces for fluid-drag reduction in turbulent flow: A Review," *Phil. Trans. Roy. Soc. A*, vol. 368, no. 1929, pp. 4775–4806, 2010.

［6］ D. W. Bechert, M. Bruse, W. Hage, J. G. T. van der Hoeven and G. Hoppe, “Experiments on drag-reducing surfaces and their optimization with an adjustable geometry,” *J. Fluid Mech*., vol. 338, pp. 59–87, 1997.

［7］ “Strategic Innovation Program for Energy Conservation Technologies, Research for the Important technologies of Energy Efficiency Projects, Investigation Research on Energy Saving Technology for High-Speed Transportation Systems by an Innovative Riblet,” Results Report, (in Japanese), New Energy and Industrial Technology Development Organization (NEDO), 2018.

［8］ P. A. Leitl, V. Stenzel, A. Flanschger, H. Kordy, C. Feichtinger, Y. Kowalik, S. Schreck and D. Stübing, “Riblet surfaces for improvement of efficiency of wind turbines,” in *Proc. AIAA Scitech 2020 Forum*, 2020, doi: 10.2514/6.2020-0308.

［9］ P. A. Leitl, E. Göttlich, A. Flanschger, A. Peters, C. Feichtinger, A. Marn and B. Reschenhofer, “Numerical investigation of optimal riblet size for TCF strut flow and their impact on the performance,” in *Proc. AIAA Scitech 2020 Forum*, 2020, doi: 10.2514/6.2020-0307.

［10］ P. A. Leitl, M. L. Garcia De Albeniz and A. Flanschger, “Nano- and microstructured riblet surfaces for centrifugal industrial compressors,” in *Proc. Conf. SUstainable PolyEnergy Generation and HaRvesting* (*SUPEHR*), 2019, pp. 32–38.

［11］ S. Inasaki, S. Sato, G. Ichinose, P. A. Leitl, A. Flanschger, S. Schreck and R. Benauer, “Numerical and Experimental Investigation of Laser Processed Riblets on Ultra-small Jet Engines and the Impact on the Performance,” (in Japanese), *The 49th Annual Conference of Gas Turbine Society of Japan*, A-25, 2021.

［12］ “Aerodynamic technology for eco-friendly aircraft,” (in Japanese), International Aircraft Development Fund (IADF), 2011.

［13］ B. N. Chichkov, C. Momma, S. Nolte, F. von Alvensleben and A. Tünnermann, “Femtosecond, picosecond, and nanosecond laser ablation of solids,” *Appl. Phys. A*, vol. 63, no. 2, pp. 109–115, 1996.

［14］ M. C. Richardson, “New opportunities with intense ultrashort-pulse lasers,” in *Proc. of SPIE*, vol. 1410, 1991.

［15］ Kie OKABAYASHI, “Direct numerical simulation for modification of sinusoidal riblets,” *JFST*, vol. 11, no. 3, 2016.

［16］ B. R. Smith, P. Yagle and P. D. McClure, “Computational simulation of staggered 3-D riblets for skin friction drag reduction,” *AIAA SCITECH 2023 Forum*. doi: 10.2514/6.2023-1763.

［17］ P. A. Leitl, C. Feichtinger, G. Schatzdorfer and A. Flanschger, “Numerical study of riblet defects and their impact on performance,” *AIAA SCITECH 2023 Forum*. doi: 10.2514/6.2023-1764.

［18］ P. A. Leitl, A. Flanschger, *et al* (2021) “Investigation of the impact of different Riblet layouts on a long- and medium-range Aircraft model,” *AIAA SCIETECH 2022 Forum*. doi: 10.2514/6.2022-0919.

小野明人　Akito ONO
次世代プロジェクト本部 第一開発部
1st Development Department
Next Generation Project Division

懸田隆史　Takafumi KAKEDA
次世代プロジェクト本部 第二開発部
2nd Development Department
Next Generation Project Division

小野明人
Akito ONO

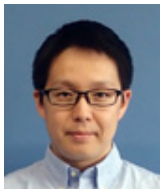

懸田隆史
Takafumi KAKEDA

大規模歪に対応したRoll-to-Rollマスクレス露光装置の開発

堀　正和，内藤一夫，中野貴之，伊倉良幸，橋場成史，鬼頭義昭

Development of Roll-to-Roll Maskless Exposure System for Large-Scale Pattern Deformation

Masakazu HORI, Kazuo NAITO, Takayuki NAKANO, Yoshiyuki IGURA,
Seiji HASHIBA and Yoshiaki KITO

フレキシブル基材の上に電子デバイスを作製したフレキシブルエレクトロニクスは，その柔軟性により従来のシリコンプロセスでは実現できなかった新しい機能が実現でき，多くの研究・応用がなされている．その製造技術として基材を連続的に処理するRoll-to-Roll技術を用いると基材のハンドリング難易度が下がり歩留まり・生産性の向上が見込まれている．さらにRoll-to-Roll技術は長さ方向のサイズ制限を受けず，長大なデバイスが生産できるため，鋭意研究・開発が進んでいる．

ところが，ポリマー材料を始めとするフレキシブル基板は従来のガラス，シリコン等と比較して熱的・機械安定性が格段に低く，電子デバイスの製造工程で従来と比較して100倍以上の大きな変形が生じることが分かっている．従来の露光装置ではこの大きな変形量を補正できず，フレキシブル基材上に電子デバイスを作製することは困難であった．

そこで，基材の変形量に対応できる補正ストロークの大きなマスクレス露光装置の開発を行った．この露光装置は基材の変形計測と露光を並列処理し連続的に露光が行える．開発した装置を使用して，A3サイズフィルムとRoll-to-Rollフィルムに対して露光評価を実施した．A3サイズ基板で実際のデバイス作製に近い条件において重ね合わせ±1.8 μm，Roll-to-Roll基板で重ね合わせ±4.0 μmの精度を達成したので詳細を報告する．

Flexible electronics, which is fabricated with electronic devices on flexible substrates, have been researched and applied, because of flexibility which was not realized in conventional silicon processes. By using Roll-to-Roll (R2R) technology, which continuously processes the substrate material, it is expected to reduce the difficulty of handling the substrate material and improve yield and productivity. In addition, R2R technology has merits for long-sized devices which is not subject to size restrictions in the length direction. However, flexible substrates such as polymer materials can be easily deformed during electronic device manufacturing process, like 100 times larger than conventional glass or silicon substrates, because of mechanical and thermal instability. It is difficult to fabricate electronic devices on flexible substrates with conventional exposure apparatuses, because they cannot compensate for large amount of deformation.

We have developed a maskless exposure system with a large correction stroke that can correspond to the amount of base material deformation. This exposure apparatus processes deformation measurement of the base material and exposure in parallel, and exposure is performed continuously. Exposure evaluation was performed for A3 size film and Roll-to-Roll film. We have achieved an overlay accuracy of ±1.8 μm for A3 size substrates and ±4.0 μm for R2R substrates, so we will report the details.

Key words 露光装置，マスクレス露光装置，フレキシブルエレクトロニクス，重ね合わせ，ロールトゥロール
exposure system, maskless exposure system, flexible electronics, overlay accuracy, roll-to-roll

1 Introduction

Conventional electronic devices rely on rigid substrates to host electronic components, whereas those assembled on soft substrates are considered flexible electronics. These devices are characterized by their lightweight, slim profile, flexibility, and stretchability, making them suitable for applications where traditional electronics would be unsuitable [1]. For instance, the adaptability of a substrate allows for bending, contraction, and excellent biocompatibility, enabling its integration as artificial skin to gather human body information [2]–[4]. Their lightweight nature and resistance to cracking also make them ideal for mobile and curved displays, leading to extensive research across various domains [5]–[7].

However, the thin and flexible nature of the polymer sub-

strate (“film substrate”) introduces handling challenges. An approach to address this issue is to fabricate the device using standard procedures, bonding it to a rigid substrate, and subsequently peeling it off [8]–[10]. However, this method necessitates an additional detachment step, and the stress incurred during both device fabrication and detachment is concentrated during the detachment process itself. Consequently, the design of a film configuration becomes crucial, thereby contributing to increased costs. An alternative solution under consideration involves the utilization of roll-to-roll transfer technology, a technique long employed in printing and other industries. This technology entails unwinding a substrate in a roll shape, guiding it using rollers, and rewinding it into a roll after processing. This approach allows for continuous handling of the substrate, preventing issues like wrinkling or buckling, thereby enhancing both productivity and yield. Moreover, the roll-to-roll process ensures the uninterrupted handling of the film, freeing the feeding direction of the film substrate from constraints posed by device size. This capability opens up the possibility of fabricating devices of unprecedented dimensions [11]–[13]. Numerous attempts have been made to fabricate devices on film substrates using roll-to-roll technology; however, these efforts have primarily focused on single-layer wiring procedures and the construction of expansive electrode structures. Examples of prototype electronic devices remain scarce. This is largely owing to film substrates exhibiting significantly lower thermal and mechanical stability compared to traditional materials like glass and silicon. Consequently, these substrates are prone to substantial deformation during the electronic device manufacturing process. Notably, conventional exposure devices cannot compensate for this large amount of deformation, making it difficult to fabricate electronic devices directly on the film substrate [14].

Therefore, to resolve this issue, we have successfully engineered a maskless exposure device capable of accommodating significant deformations in film substrates. Fig. 1 shows a photograph of the developed device. This exposure device is designed to enable roll-to-roll transfer of the film substrate, allowing for parallel processing of deformation and exposure measurements. Moreover, the device ensures continuous processing without necessitating to halt the transfer process.

However, creating patterns on the film substrate remains challenging. In this document, we delve into the technical challenges encountered during device development and present our proposed solutions. We then provide an overview of the developed device, detailing its exposure and alignment systems, along with the evaluation results. Finally, we discuss the outcomes of roll-to-roll exposure and showcase a sample device prototype produced using the newly developed maskless exposure device.

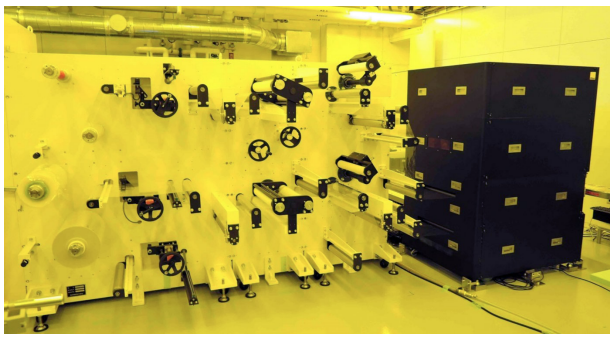

Fig. 1 Photograph of the developed direct drawing exposure device and transfer unit

2 Technical issues and solutions

To achieve precise exposure on flexible substrates, our device was developed based on the following key concepts:

(1) Issues with film handling

Given their low mechanical strength, flexible films are susceptible to deformation owing to even minor changes in tension during transfer. Consequently, any external force applied to the film during the transition from alignment to exposure can lead to deformation, hindering the attainment of high-precision overlay exposure. Therefore, it is essential to maintain the film’s integrity and prevent deformation during the transfer process between alignment and exposure. In typical exposure devices, alignment and exposure are performed by securing the substrate onto a flat stage. However, when applied to thin and flexible films, this method can lead to significant deformations and wrinkles owing to surface adhesion. To overcome this challenge, we have adopted an alternative approach where the film is wrapped around a large roller, utilizing frictional force to secure it. The film is then transferred by rotating the roller. Upon initial contact with the roller, the film is fixed through line contact, effectively minimizing deformation. Alignment measurements are conducted directly on the roll’s surface, and exposure takes place in situ. To accommodate this configuration, all sensors are positioned along the roller’s curvature. Moreover, these rollers serve as a transfer mechanism, enabling continuous roll-to-roll processing of the film.

(2) Issues with large film deformation

Film substrates exhibit deformations at a significantly higher rate of approximately 1000 ppm owing to heat and

film stress, which is 100 times greater than that of glass. Moreover, local stress is induced during pattern fabrication processes, resulting in nonlinear deformation specific to the pattern's shape. Hence, we opted for a maskless direct writing exposure technique capable of accommodating such deformations and substantial correction distances. Multiple options for maskless direct writing exposure methods are available. However, given the curved surface of the roller where exposure takes place, surface-based techniques are anticipated to result in the ends beyond the ridgeline of the roll falling out of the depth of focus. Therefore, we adopted a scanning method using polygons, enabling exposure along a one-dimensional straight line without relying on surface exposure.

(3) Issues regarding productivity

The maskless exposure device operates by utilizing image data, where the device assesses film substrate deformations, digitally adjusts the original image, and subsequently performs exposure, allowing for substantial corrections. However, there is a time lag from measurement to image generation and development, posing a challenge for continuous processing. Furthermore, digital image corrections might cause quantization and misalignment issues, potentially disrupting wiring. While enhancing image resolution can alleviate quantization effects, it concurrently increases data size exponentially, thereby prolonging image processing. Thus, we adopted a technique that mechanically and optically transforms the exposure pattern while retaining the original exposure image data. Furthermore, a target exposure speed that can be feasibly attained in mass production is established. Details are given in the device description.

3 Details of developed device

3.1. Overview of overall device structure

Fig. 2 shows the overall structure of the developed roll-to-roll direct drawing exposure device.

The film is unwound from the roll, passes through the exposure unit, and is then rewound onto another roll. Both the unwinding and winding rolls are positioned on the same side, forming a U-shape transfer configuration that minimizes the device's overall length. A sensor measures the film's edge right after it leaves the roll, and the unwinding roll is adjusted to maintain a constant edge position relative to the device. This ensures a stable film position during exposure, reducing any potential deviations. The device can accommodate roll films up to 200 meters in length, assuming a film thickness of 100 μm. Film substrates become charged

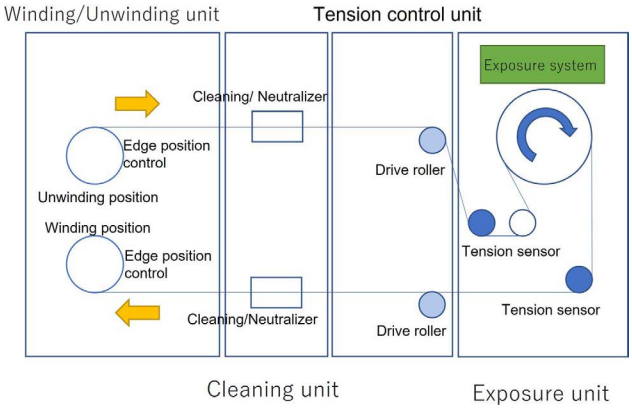

Fig. 2 Overview of overall exposure device configuration

by rubbing against the roll and peeling. A charged film destroys devices on the film and attracts particles in the air, causing defects. Therefore, we installed a unit that removes static electricity from the film and a cleaning unit that removes dust. The film substrate is a non-conductor and is transferred by multiple rollers; hence, the elimination of static electricity is particularly important.

The rotation speed of the roller within the exposure unit, referred to as the main roller, determines the transfer speed of the entire device. Maintaining a constant rotation speed for the main roller ensures the stability of the exposure position and the amount of exposure. Rollers with tension sensors attached in the front and backside of the main roller are installed, and the tension of the film introduced to the main roller is measured. Moreover, the tension of the film is controlled by the tension adjustment unit, which controls the difference in speed between the main roller and the drive roller and keeps the expansion and contraction of the film constant in the transfer direction.

The exposure system measures the alignment of the continuously transferred film in parallel and exposes it according to the position of the pattern measured by the alignment. Details of the exposure system are described below.

3.2. Exposure system

Fig. 3 shows a schematic of the developed exposure system. The exposure system was comprised of several components: an exposure module responsible for performing the exposure process, an alignment microscope used for measuring the film's shape, and an encoder read head along with an encoder ring, which were utilized to detect the precise position of the main roller. Components such as sensors were arranged along the curved surface of the main roller.

To increase the overall exposure width, we arranged six exposure modules into two rows with a staggered configuration. Each individual exposure module had a width of 50

mm, collectively providing a combined exposure area of 300 mm in width. Employing a direct writing exposure technique utilizing polygons, the exposure modules were capable of applying linear patterns, ensuring accurate exposure on curved rollers without encountering any defocusing problems.

The unit pixel size for direct exposure was set to 2 μm square. A total of seven alignment microscopes were placed at the joints of each module, facilitating alignment measurement over the entire exposure width.

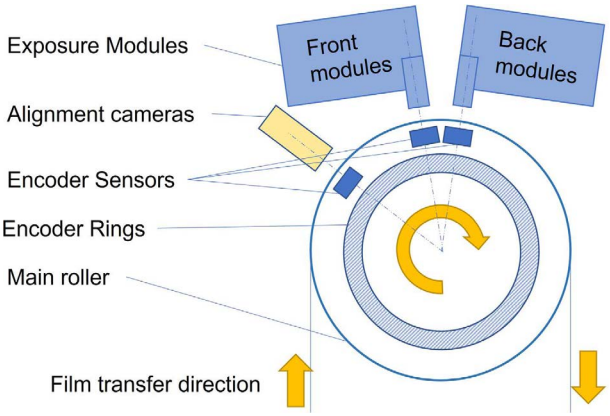

Fig. 3 Schematic side view of exposure system

Encoder rings were positioned on either side of the main roller to monitor its rotation. The encoder heads were aligned in two rows corresponding to the arrangement of the exposure module, ensuring adherence to Abbe's principle and minimizing measurement inaccuracies. Employing a three-phase design, each encoder head utilized the shared Z-phase on the encoder ring to establish calibration origins for each encoder. Please refer to Fig. 4, an expansion of Fig. 3 on a plane, for visual reference.

When employing the direct drawing exposure technique with a polygon mirror, exposure is hindered when the exposure light encounters the corners of the polygon mirror. This limitation prevents the polygon mirror from being utilized to its full extent. Fig. 5 shows a schematic diagram of the usable angle of the polygon and the exposure timing chart. In the example below, if only one-third of the octagonal polygon's surface area can be allocated for exposure, the efficiency of light source utilization becomes limited to one-third. To enhance the efficiency of light source utilization, a time-division method is employed, whereby the light source is shared among the three polygons. This is achieved by shifting the phase of each polygon by 15 degrees to ensure that their exposure angles do not align temporally. Consequently, one polygon is consistently in the exposed state, resulting in nearly 100% light source utilization efficiency and enhanced productivity.

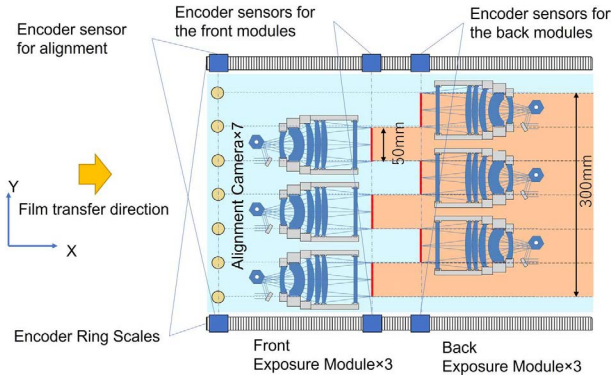

Fig. 4 Schematic diagram of exposure system development

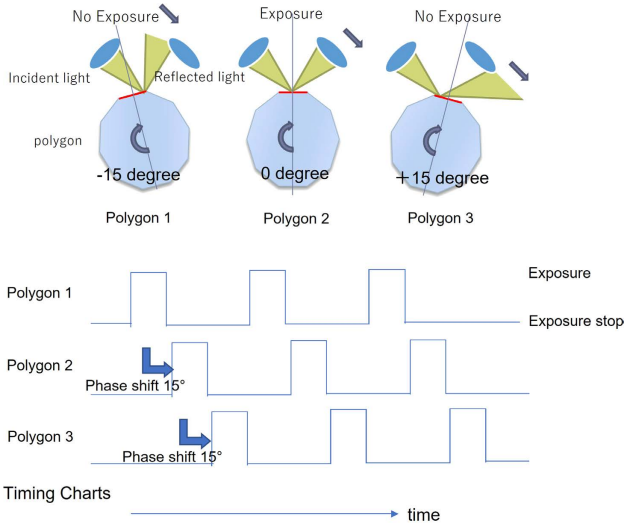

Fig. 5 Highly efficient utilization of polygons

3.3. Exposure results

Fig. 6 displays an image of the resolution chart that was exposed using the developed exposure system. The procedure involved applying a 1-μm layer of photoresist OFPR-5000LB (Tokyo Ohka Kogyo Co., Ltd., Kanagawa, Japan) onto a poly ethylene terephthalate (PET) film, which was further coated with a 100-nm layer of vapor-deposited Cu. Subsequently, exposure took place. Following exposure, the film was subjected to one-minute development using a 2.38% concentration of tetramethylammonium hydroxide (TMAH). Notably, the exposure process was based on the bitmap image (BMP) format image data stored in the device, and that each module achieved a minimum resolution of 4 μm line/space (L/S). The results confirmed that practical patterns, with an L/S of 6 μm, could effectively be generated within a 300 mm width using arbitrary image data.

3.4. Exposure pattern deformation method

The newly developed exposure device facilitates a real-

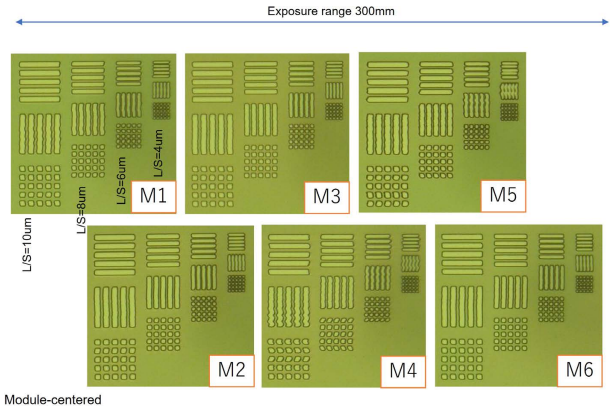

Fig. 6 Resolution chart pattern exposure result

time transformation of the exposure pattern by altering the drawing position optically and mechanically while preserving the original exposure image data. This is achieved by dynamically adjusting the exposure lines scanned by the polygon mirror within the regions delimited by each of the six exposure modules. This real-time correction addresses intricate and substantial deformations effectively. As shown in Fig. 7, there are four components to be changed (shift Y/Y magnification/X magnification/rotation). The deformation method for each component is described below.

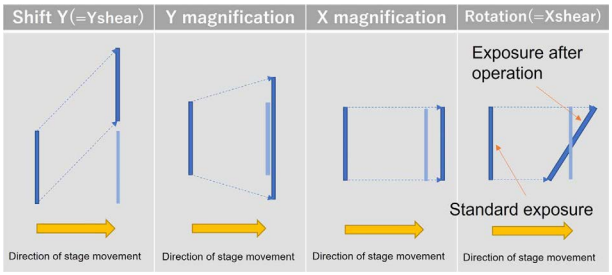

Fig. 7 Diagram of each correction operation

3.4.1. Shift Y (=Y shear)

The Y direction corresponds to the polygon scanning direction. Shifting the exposure position in the Y direction involves introducing a time offset to the polygon scan initiation time. The combination of roller rotation and the Y shift operation permits the induction of Y shear deformation. The vector diagram of the exposure outcomes with continuous Y shift alterations is shown in Fig. 8(a).

3.4.2. Y Magnification

Y magnification induces slight alterations in the exposure interval by modifying the light emission cycle of the light source, resulting in overall scaling changes. The periodic modulation can be adjusted for each polygon face, enabling exposure while smoothly varying the magnification. Fig. 8(b) portrays a vector diagram illustrating the outcomes of continuous Y magnification adjustments.

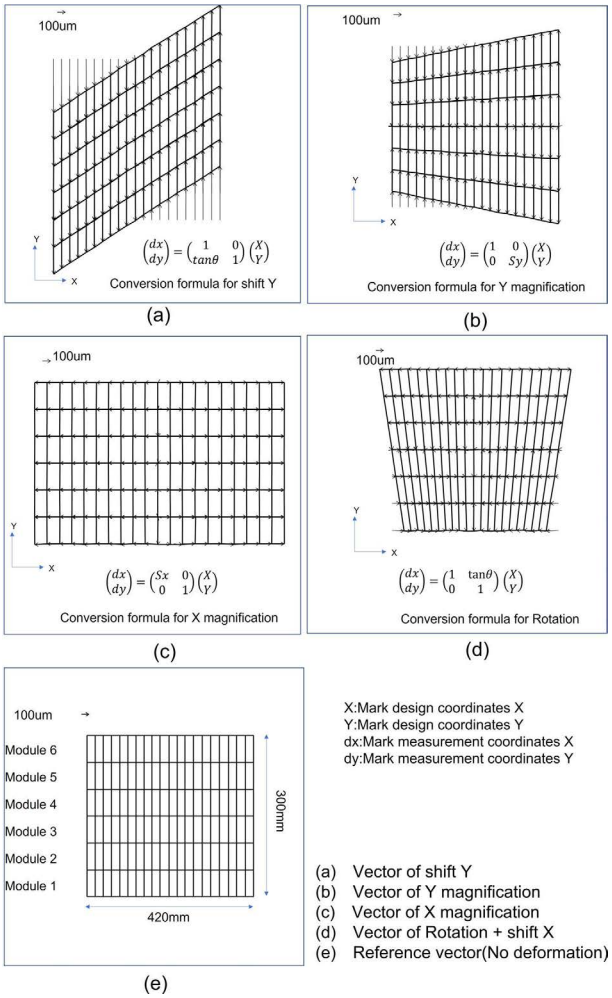

Fig. 8 Vector diagram of pattern deformation exposure result

3.4.3. X Magnification

The X direction corresponds to the roller rotation direction. The X magnification is altered by adjusting the correlation between the roller and rotation speeds of the polygon mirror. For instance, if the stage maintains a constant speed, elevating the polygon's rotation speed heightens the exposure density, resulting in pattern contraction. Conversely, decreasing the rotation speed elongates the pattern. Fig. 8(c) shows a vector diagram illustrating the outcomes of implementing adjustments to X magnification.

3.4.4. Rotation (= X shear)/Shift X

The device incorporates a mechanism capable of mechanically rotating the module around its center, using the 50 mm exposure range of the module as a pivot reference. This rotational capability allows for the manipulation of the exposure pattern. When combined with the roller-driven film transfer motion, this mechanism facilitates deformation in the X shear direction. Furthermore, each module is furnished with an optical element that introduces an exposure position shift along the X axis. Activating this element during exposure enables individualized shift adjustments (X-shift)

for each module. In Fig. 8(d), the vector diagram illustrates the results obtained from continuous module rotation. Although the amount of rotation is consistent for each module, the integration of rotation with an X-shift introduces a transformation of the trapezoidal shape.

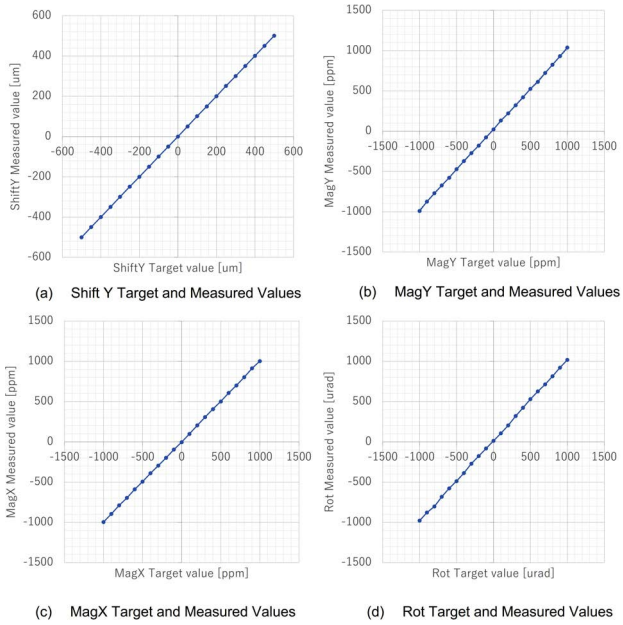

Fig. 9 Relationship between the exposure indication and measured values

Fig. 9 shows the linearity measurement results corresponding to each deformation motion shown in Fig. 8. The X axis shows the exposure machine target value, whereas the Y axis shows the actually measured deformation amount. Fig. 9(a) demonstrates the linear operation within the scope of −500 μm to 500 μm for shift Y. In Fig. 9(b), the Y magnification operates linearly between −1000 ppm and 1000 ppm. Similarly, Fig. 9(c) showcases the linear operation of X magnification within a range of −1000 ppm to 1000 ppm. Finally, Fig. 9(d) portrays the linear behavior of rotation, ranging from −1000 μrad to 1000 μrad.

4 Overlay exposure

The alignment measurement process of the developed device is outlined as follows. The film's X-direction position is measured by taking measurements synchronized with the encoder's position during the film's transfer. Aligned along the Y direction, the alignment microscope measures the film's Y-direction position. The magnitude of film deformation can be ascertained by comparing the alignment microscope's measured mark position with its designated value. Although this procedure is performed within each module, the alignment camera is shared among neighboring modules. This arrangement enables seamless calculations across modules, maintaining pattern consistency even in cases where exposure module joints or alignment rows are switched.

Following the computation of correction values for each pattern deformation component from the alignment measurements, the exposure unit then proceeds to conduct exposure based on these correction values. Fig. 10 shows the alignment calculation model. The correction amount is calculated using the model formula from the measurement results of the alignment microscope and the design coordinates. Continuous patterns such as the roll-to-roll case are handled by repeating this calculation for each column.

4.1. Overlay accuracy evaluation and results

The results of evaluating the alignment measurement and overlay exposure are described. The results of fabricating a laminated structure on an A3-sized film and the results of fabricating a laminated structure by transferring the film by a roll-to-roll method are shown.

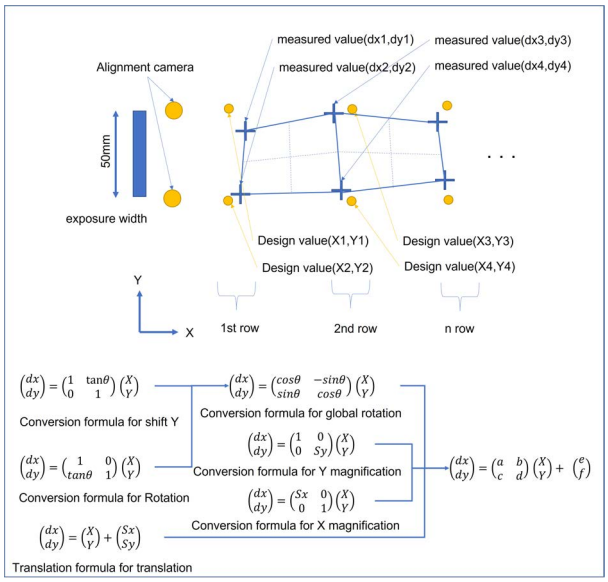

Fig. 10 Alignment calculation model

4.1.1. Evaluation results for A3 size film

A multilayer structure consisting of Al/SiO_2/Al/protective film was fabricated on an A3-size PI film. Photolithography was used to process metal wiring and open patterns on each layer. Additionally, an intermediate layer was annealed at 200 °C for one hour. Fig. 11(a) shows the vector diagram of the shape of the film when processing the protective film, and Fig. 11(b) shows the vector diagram of the measurement error amount when conducting overlay exposure.

The film's shape in Fig. 11(a) exhibits contraction along the longitudinal and expansion along the lateral direction due

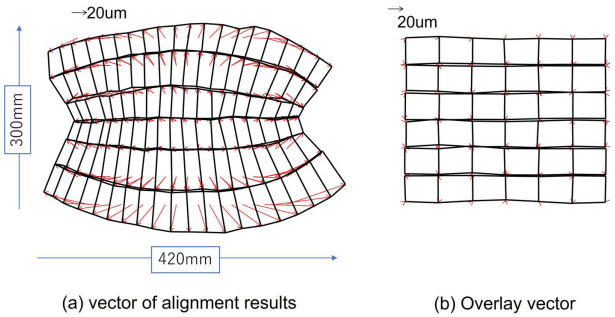

Fig. 11 Evaluation result of overlay accuracy on A3 film

to film stress and annealing. Achieving overlay exposure on such a shape using conventional exposure devices is challenging. However, the exposure device developed in this context demonstrates the capability to perform exposure while accommodating the film's deformation. Fig. 12 shows the histogram of the overlay error amount of the exposed film. The overlay accuracy has a mean of $+3\sigma$ and is $\pm 1.8\ \mu$m for both X and Y. Furthermore, the device was verified to successfully track the film's deformation and execute overlay exposure for all other layers.

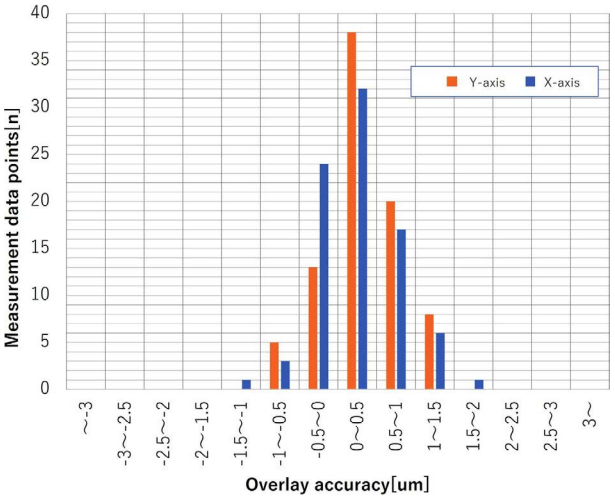

Fig. 12 Histogram of A3 film overlay error amount

4.1.2. Roll-to-roll evaluation results

After continuously forming Al wiring for 20 m using the roll-to-roll method, an insulating layer was formed and annealed. An aperture pattern was formed by photolithography while aligning the film in this state. Fig. 13 shows the film shape and measurement results of overlay exposure when alignment exposure was conducted on the film.

The alignment results indicate elongation in the X direction and a meandering component in the Y direction. Moreover, deformation is possibly caused by the process. However, the overlay outcomes have been adequately rectified, and the histogram presented in Fig. 14 demonstrates that the overlay accuracy remains within a range of $\pm 4\ \mu$m. In a previous report, we presented the findings of film patterning, confirming the successful fabrication of highly precise long-distance patterning under conditions that closely resemble actual processing [15].

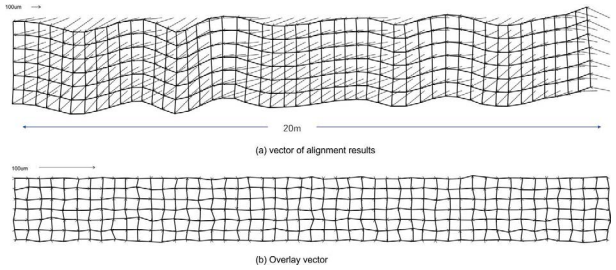

Fig. 13 Overlay accuracy evaluation results during roll-to-roll exposure

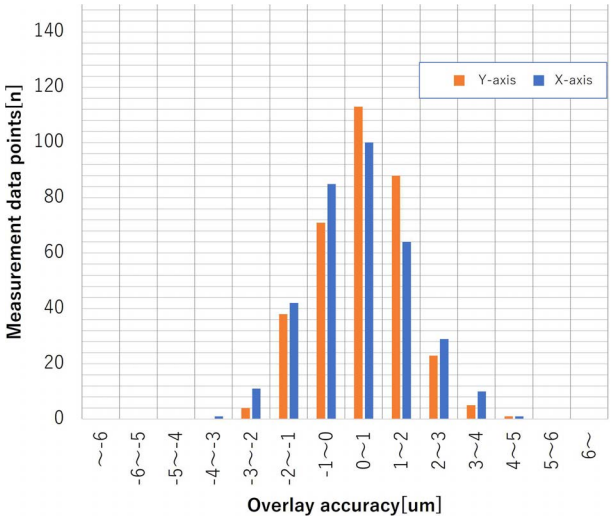

Fig. 14 Histogram of roll-to-roll overlay error amount

5 Pattern fabrication example

We have successfully validated the feasibility of generating a wide range of patterns on films using the exposure device, encompassing laminated structures and monolayer wiring patterns. In Fig. 15, we illustrate an actual prototype of an extended pattern. Our efforts have extended beyond refining the exposure process; we have also designed equipment that supports the roll-to-roll process, enabling the creation of continuous patterns spanning at least 20 meters in all roll-to-roll procedures. During the device prototyping phase, iterative checks and adjustments are typically necessary in each process, impacting patterns. However, given that this device operates as a maskless direct drawing exposure system, adjustments can be seamlessly implemented by altering the computer aided design (CAD) data, leading to an enhanced prototyping cycle and increased frequency of trials. Moreover, when producing devices that harness flexible proper-

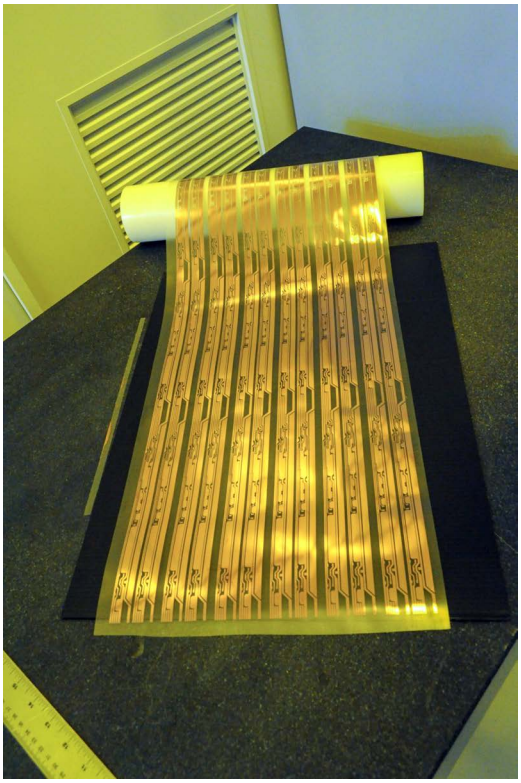

Fig. 15　Prototyped long pattern

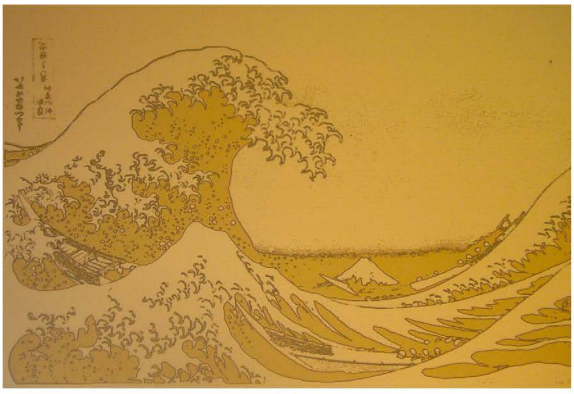

(a)

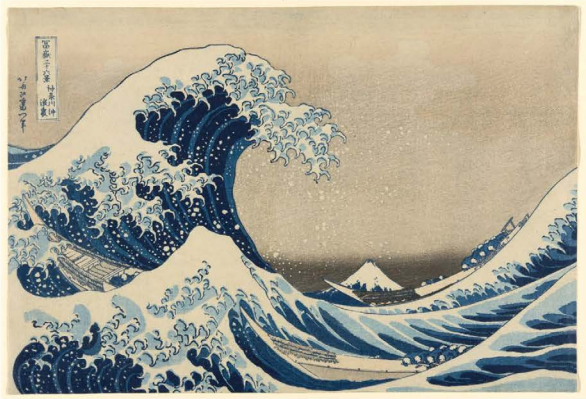

(b)

Artist Katsushika Hokusai
Title Under the Wave off Kanagawa ,also known as The Great Wave, from the series Thirty-Six Views of Mount Fuji (Fugaku sanjūrokkei)
Place Japan (Object made in)
Date 1826–1836
The Art Institute of Chicago

Fig. 16　Thirty-Six Views of Mt. Fuji exposed by maskless exposure machine

ties, such as flexible electronics, precision in shaping the devices to match their intended form and function is crucial. With a maskless approach, the potential for on-demand manufacturing emerges, allowing for tailored fabrication based on specific applications through image data updates. This flexibility also enables the prototyping of devices with diverse shapes within an extended film. To illustrate this capability, Fig. 16 presents an exposure demonstration of an arbitrary pattern derived from the image "Thirty-Six Views of Mt. Fuji". In Fig. 16(b), the original image is depicted, whereas Fig. 16(a) demonstrates the exposed image with dimensions of 800 μm × 600 μm. Notably, a highly intricate pattern has been achieved, even capturing subtle details such as water splashes in miniature regions.

6 Conclusion

In summary, our development of a maskless exposure device capable of achieving high-precision overlay exposure on films with significant deformation achieved promising results. We successfully demonstrated the creation of laminated films requiring precise alignment, ranging from A3-sized films to continuous films extending over 20 meters. Notably, for A3-sized films, we verified the attainment of sub-2 μm accuracy for overlaying patterns as fine as 6 μm L/S (Line/Space) on extensively deformed films subjected to deposition and annealing processes.

An additional advantage lies in the adaptability of the exposure pattern through simple modifications of CAD data. This capability proved highly valuable for rapid prototyping and the realization of on-demand patterns. Moreover, the exposure device holds particular promise for the roll-to-roll method, enabling the flexible production of a diverse array of electronic devices. We anticipate that our device will significantly contribute to the advancement of flexible electronics.

References

[1] K. Kuribara *et al.* "Organic transistors with high thermal stability for medical applications," *Nature Communications,* Vol. 3, 723, 2012.

[2] B. Wang *et al.* "Foundry-compatible high-resolution patterning of vertically phase-separated semiconducting films for ultraflexible organic electronics," *Nature Communications*, Vol. 12, 4937, 2021.

[3] M. Kaltenbrunner *et al.* "Ultrathin, highly flexible and stretchable PLEDs," *Nature Photonics*, Vol. 7, pp. 811–816, 2013.

[4] K. Nomura, H. Ohta, A. Takagi, T. Kamiya, M. Hirano and

H. Hosono, “Room-temperature fabrication of transparent flexible thin-film transistors using amorphous oxide semiconductors,” *Nature*, Vol. 432, pp. 488–492, 2004.

[5] L. Zhou, A. Wanga, S. Wu, J. Sun, S. Park and T. N. Jackson, “All-organic Active Matrix Flexible Display,” *Appl. Phys. Lett*, Vol. 88, 083502, 2006.

[6] I. Yagi *et al.* “A Full-Color, Top-Emission AM-OLED Display Driven,” *SID 07 DIGEST*, Vol. 63–2, pp. 1753–1757, 2007.

[7] M. Mizukami *et al.* “Flexible AM OLED Panel Driven by Bottom-contact OTFTs,” *IEEE Electron. Dev. Lett*, Vol. 27, pp. 249–251, 2006.

[8] Y. Nakajima *et al.* “Improvement in Image Quality of a 5.8-in. OTFT-Driven Flexible AMOLED Display,” *Journal of the SID*, Vol. 19, pp. 94–99, 2011.

[9] M. Nakata *et al.* “Development of Flexible Displays Using Back-channel-etched In–Sn–Zn–O Thin-film Transistors and Air-stable Inverted Organic Light-emitting Diodes,” *Journal of the SID*, Vol. 24–1, pp. 3–11, 2016.

[10] T. Aoyama *et al.* “An 8.34-inch 1058-ppi 8K x 4K Flexible OLED Display,” *SID 2017 DIGEST*, Vol. 24–3, pp. 338–341, 2017.

[11] J. Yoon *et al.* “World 1st Large Size 18-inch Flexible OLED Display and the Key Technologies,” *SID 2015 DIGEST*, Vol. 65–1, pp. 962–965, 2015.

[12] J. Hong *et al.* “The First 9.1-inch Stretchable AMOLED Display Based on LTPS Technology,” *SID 2017 DIGEST*, Vol. 5–5, pp. 47–50, 2017.

[13] H. Shin *et al.* “Advanced OLED Display Technologies for Large-Size Semi-Flexible TVs,” *SID 2017 DIGEST*, Vol. 45–2, pp. 609–612, 2016.

[14] Y. Kito *et al.* “Direct Imaging Exposure Equipment with High Overlay Accuracy for Flexible Substrate in Roll-to-Roll Method,” *Proceeding of IDW 16*, pp. 515–518, 2016.

[15] Y. Kito *et al.* “Novel Direct Imaging Exposure System with High Productivity for Flexible Substrate in Roll-to-Roll Method,” *Proceeding of IDW 17*, pp. 500–512, 2017.

堀　正和　Masakazu HORI
FPD 装置事業部開発統括部 先端技術開発部
Advanced Technology Development Department
Development Sector, FPD Lithography Business Unit

伊倉良幸　Yoshiyuki IGURA
FPD 装置事業部開発統括部 先端技術開発部
Advanced Technology Development Department
Development Sector, FPD Lithography Business Unit

内藤一夫　Kazuo NAITO
FPD 装置事業部開発統括部 先端技術開発部
Advanced Technology Development Department
Development Sector, FPD Lithography Business Unit

橋場成史　Seiji HASHIBA
FPD 装置事業部開発統括部 先端技術開発部
Advanced Technology Development Department
Development Sector, FPD Lithography Business Unit

中野貴之　Takayuki NAKANO
FPD 装置事業部開発統括部 先端技術開発部
Advanced Technology Development Department
Development Sector, FPD Lithography Business Unit

鬼頭義昭　Yoshiaki KITO
FPD 装置事業部開発統括部 先端技術開発部
Advanced Technology Development Department
Development Sector, FPD Lithography Business Unit

SPPC アレイ検出器を用いた共焦点超解像イメージング

大川潤也，小森谷大介，楠井雄太

Confocal Super-Resolution Imaging using SPPC Array Detector

Junya OHKAWA, Daisuke KOMORIYA and Yuta KUSUI

細胞は生き物の体を作る基本的な構成要素である．この数十マイクロメートル程度の大きさの細胞の中には，核，ミトコンドリア，小胞体，ゴルジ体などのたくさんのオルガネラ（細胞内小器官）や，無数の蛋白質が存在し，生命活動を維持するために機能している．オルガネラや蛋白質は蛍光染色が可能で，長年蛍光顕微鏡でイメージングされてきた．近年では，様々な細胞機能や病態生理のメカニズムをより正確に理解するために，より高い空間分解能での観察が求められるようになってきている．

共焦点レーザー顕微鏡システム AX/AX R は，焦点外の不要な光を取り除いた断層像を取得することが出来る蛍光顕微鏡であり，細胞の観察に使用されている．我々は，AX/AX R に超解像検出器ユニット NSPARC（Nikon SPatial ARray Confocal）を新たに搭載した．NSPARC は SPPC アレイという特殊な検出器を用いることで，従来の共焦点顕微鏡の長所を損なうことなく，空間分解能を向上させることが出来る．本稿では，まず NSPARC の空間分解能向上の光学的原理を説明する．続いて，検出器に使用している SPPC アレイ検出器について説明する．最後に，生物サンプルでのアプリケーション例を紹介する．

Cells are the basic elements of living organisms. Cells, which are several tens of micrometers in size, contain numerous organelles such as the nucleus, mitochondria, endoplasmic reticulum, and Golgi apparatus, including countless proteins that function to maintain life activities. Organelles and proteins can be fluorescently stained and have been imaged with a fluorescence microscope for several years. To understand the physiological mechanism more accurately, higher spatial resolution imaging is required.

The confocal laser microscope system AX/AX R is a fluorescence microscope that can acquire thin optical sectioning images without unnecessary out-of-focus light, and is utilized to image cells. We installed a new super-resolution detector unit NSPARC (Nikon SPatial ARray Confocal) on the AX/AX R. NSPARC employs a special detector called an SPPC array to improve spatial resolution without sacrificing the advantages of conventional confocal microscopes. Here, we first explain the optical principle of improving the spatial resolution of the NSPARC, and then explain the SPPC array detector. Finally, we introduce an application model for biological samples.

Key words 共焦点顕微鏡，超解像イメージング
confocal microscopy, super resolution

1 Introduction

Confocal microscopy [1] targets tissue sections and cell clusters with a size of several hundred micrometers to several millimeters, and cells of tens of micrometers (Fig. 1(a)). The smallest target is a microstructure within cells called organelles, which have a size of several hundred nanometers. These organelles can be labeled with different colors with fluorescent proteins or fluorescent dyes, and their intracellular dynamics can be imaged with a confocal microscope (Fig. 1(b-e)). The structures and subcellular localizations of organelles are closely related to the cell function and pathophysiology and are subject to imaging in fields such as life science and drug discovery.

Although conventional confocal microscopes can capture the external shapes of organelles, it is difficult to accurately capture the fine internal structure. There were problems in terms of large trade-offs, such as a significant decrease in temporal resolution and an increase in photo-damage, as described below. Therefore, we developed a super-resolution detector unit called NSPARC that can improve the spatial resolution of conventional confocal microscopy applications without these trade-offs.

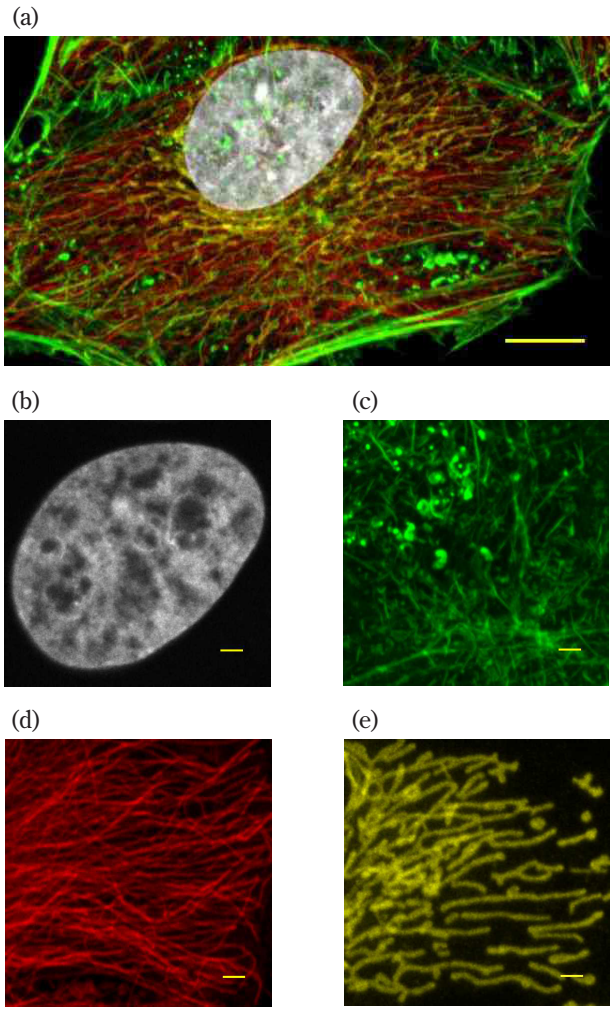

Fig. 1 Multicolor images captured with a confocal microscope
(a) Four types of organelles of HeLa cells were fluorescently labeled and captured with a confocal microscope (AX).
White: Nucleus
Green: Actin (cytoskeleton)
Red: Microtubules (cytoskeleton)
Yellow: Mitochondria
(b-e) Enlarged monochrome image of each organelle
Scale bar (a) 10 μm, (b-e) 2 μm

2 Optical principles of NSPARC

First, an outline of the principles of a confocal microscope is given. A confocal microscope is a type of laser scanning microscope that restricts out of focus light by passing the fluorescence signals from a sample through a confocal pinhole and extracting only the fluorescence signals near the focal plane. In the confocal optical system laser scans the sample surface in a state in which the pinhole and the laser light source always maintain a conjugate relationship. A sample image can be captured by measuring the intensity of fluorescent light that has passed through the pinhole with a photodetector such as a photomultiplier tube (PMT) and creating a light intensity map that associates the position of the scanning mirror with the measured light intensity (Fig. 2). A confocal microscope image is characterized by a high signal-to-noise ratio (S/N) because of the suppression of out of focus light by the pinhole.

To obtain images with a high spatial resolution while ensuring a high S/N, it is necessary to narrow the pinhole diameter to the Airy diameter, which is the spot size calculated from the theoretical calculation of the point spread function (PSF) of the fluorescence signal. In confocal microscopes, it is common to use the values converted to the Airy unit (AU) to express the pinhole diameter, and this expression is also used in this paper.

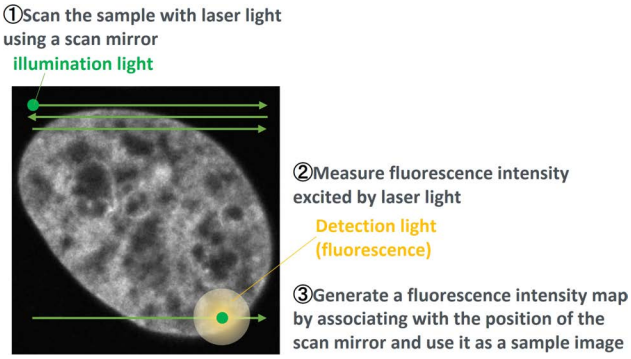

Fig. 2 Fluorescence signal image acquisition scheme of confocal microscope

For general observation, the pinhole diameter is set to a value close to 1 AU (= 1.22 λ/NA), which balances the spatial resolution and S/N. However, when spatial resolution is prioritized, the pinhole may be narrowed to less than 1 AU. If the pinhole diameter is reduced, the spatial resolution improves, but when the pinhole diameter is less than 1 AU, the fluorescence signal is also cut off significantly, resulting in the deterioration of S/N. Comparing the relationship between the spatial resolution and fluorescence intensity with respect to the change in pinhole diameter, it can be seen that the decrease in fluorescence intensity is steeper than the improvement rate of the spatial resolution under the condition of a narrow pinhole with less than 1 AU (Fig. 3). The deterioration of the S/N also adversely affects the results of deconvolution (inverse convolution calculation) image processing. Therefore, if the pinhole size is reduce, it is not always possible to capture a high spatial resolution images. In order to capture high-resolution images, it is necessary to improve the resolution while maintaining the S/N. Therefore, it is necessary to decrease the operation speed or increase the laser power to improve the S/N. However, these measures are accompanied by large trade-offs such as a decrease in temporal resolution and an increase in photodamage to the sample. NSPARC is a microscope device that

has overcome this trade-off relationship between spatial resolution and S/N, and adopts an optical system based on image scanning microscopy [2]–[5] (hereinafter referred to as ISM), enabling image acquisition with both high S/N and high spatial resolution.

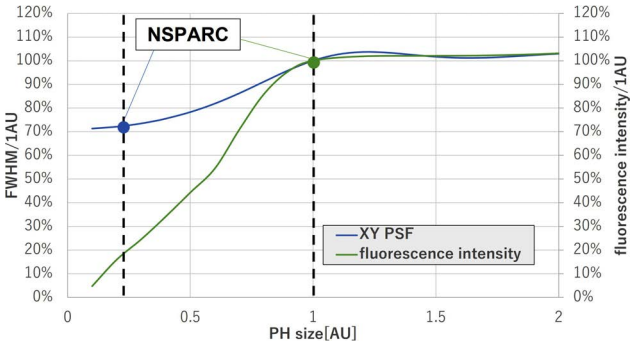

Fig. 3 Relationship between pinhole diameter and fluorescence -spatial resolution
FWHM: Full Width at Half Maximum

Next, ISM, which is the imaging technology used in NSPARC, is explained. In ISM, instead of a pinhole, a two-dimensional array detector is placed at a position at which it can be conjugated with a laser light source. While this detector functions as a pinhole, it also performs light intensity measurements at the same time. In addition, by using an array detector, the fluorescence projected onto the detection surface can be divided and captured by each pixel, and the spatial resolution can be improved by the image processing described below. Under standard observation conditions, projection was performed under the condition that 1 AU is inscribed onto a 5 × 5 pixel array detector, and fluorescence signal for the size of 0.2 AU per pixel is captured (Fig. 4).

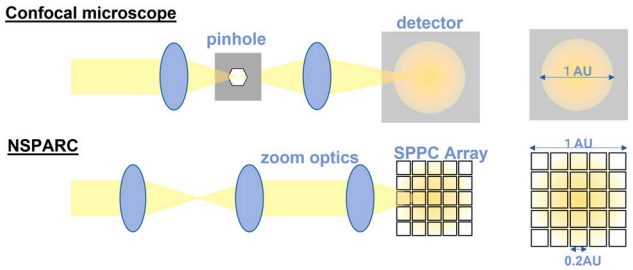

Fig. 4 Comparison of the optical systems of a confocal microscope and NSPARC

Each pixel of an array detector generates a light intensity map from the results of the light intensity measurements, and outputs it as an image. These output images have an improved spatial resolution because each pixel corresponds to a pinhole with a diameter of 0.2 AU, but they are dark and have a poor S/N because these are images captured with small pinhole. However, as a fluorescent signal equivalent to 1 AU can be secured if the images obtained from each pixel are summed up, the S/N of the images can be increased. However, image shifts occur between the images obtained by each pixel, and the spatial resolution then becomes equivalent to 1 AU just by summing up. In ISM, images with both a high resolution and high S/N, which were difficult to obtain with conventional confocal microscopes, can be obtained by performing reassignment processing. This is a process during which images are shifted and summed up while a spatial resolution of 0.2 AU is maintained (Fig. 5).

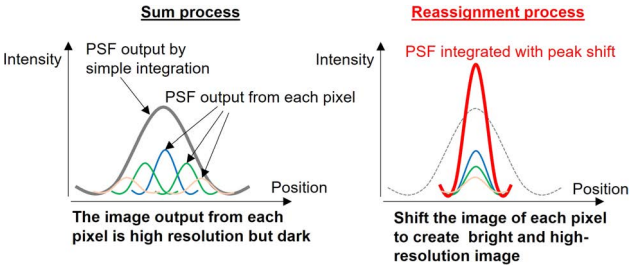

Fig. 5 Relationship between reassignment processing and PSF

The basic principle of reassignment processing, which is the image processing used in ISM, is explained. Effective PSF_{eff}, which represents the imaging performance of a confocal microscope, can be obtained by calculation, and the effective PSF_{eff} of each pixel of an array detector can also be estimated. In reassignment processing, the amount of PSF shift due to each pixel arrangement of the array detector is calculated by a theoretical calculation and is corrected to match the PSF peak position of each pixel by shifting it in the reverse direction during summing up.

The effective PSF_{eff} of a confocal microscope is obtained from Eq. (1) from PSF_{ex}, as determined by the excitation optical system, PSF_{em}, as determined by the detection optical system, and the pinhole function, PH.

$$PSF_{eff}(r) = PSF_{ex}(r)\{PSF_{em}(r) \otimes PH(r)\} \quad (1)$$

In the ISM optical system using an array detector, each pixel acts as a tiny pinhole and moreover, it is at a position shifted from the optical axis by the arrangement of each pixel. Therefore, the effective PSF_{eff} of each pixel is obtained from Eq. (2) when the pinhole is positioned at the position with the same axis shift as the arrangement of the array detector.

$$PSF_{eff}(r) = PSF_{ex}(r)\{PSF_{em}(r) \otimes PH(r-d)\} \quad (2)$$

It can be seen that PSF_{eff} in this case has a peak position

at a position shifted from the optical axis (Fig. 6). As the shift amount and the shift direction also change depending on the position of the pixel, the correction amount of the shift is calculated for each pixel, and the output images from each pixel are moved and summed up. The process of shifting and summing up these images is called reassignment processing, and the images captured at each pixel can be summed up while maintaining a spatial resolution of 0.2 AU. The reassigned image can haven an improved spatial resolution by about 1.3 times while the S/N can also be maintained with respect to the standard 1 AU image.

In addition, it is possible to perform deconvolution of the reassigned image by using the effective PSF_{eff} after reassignment processing. This image processing can remove background light blurring and improve the spatial resolution.

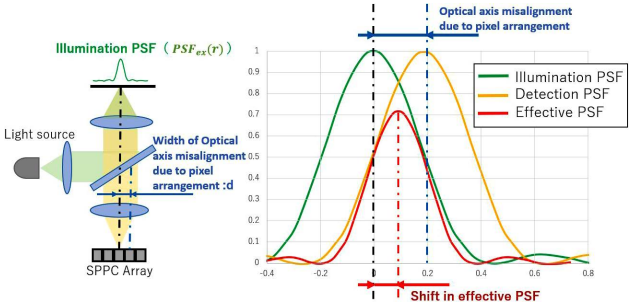

Fig. 6 PSF of ISM

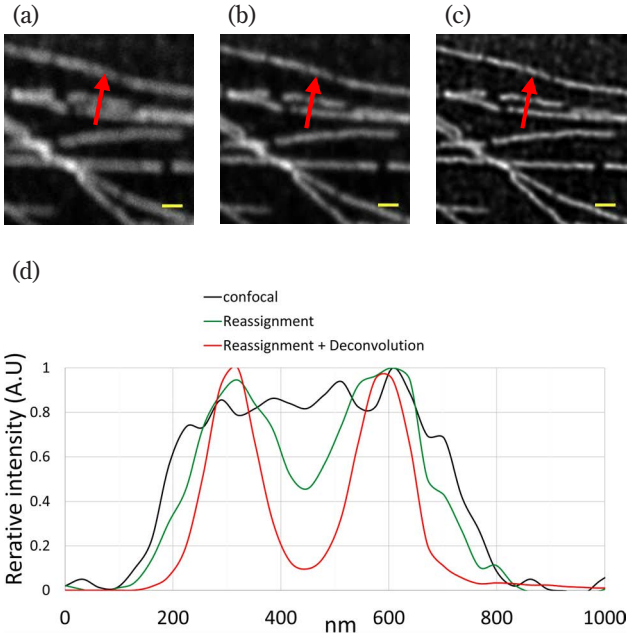

Fig. 7 Spatial resolution in biological samples
Microtubules of HeLa cells captured with PlanAPOλD 60x 1.42
(a) Confocal image
(b) Reassigned image
(c) Reassigned image + Deconvolution processing
Scale bar is 500 nm.
(d) Line profile shown in (a) to (c)

Fig. 7 shows (a) a confocal image, (b) a reassigned image, and (c) a deconvoluted image of the reassigned image. It can be seen that the two linear structures that could not be resolved in the confocal image can be confirmed as the cleavage after the reassignment processing and can be further clearly resolved into two by deconvolution.

3 SPPC Array detector

Next, we explain the single pixel photon counter (SPPC) array detector newly adopted by NSPARC. The detector used in NSPARC is a newly developed SPPC array. The SPPC array is a photon counting device in which avalanche photo diodes (APDs) are arranged in array form. It is sometimes called a single photon avalanche diode (SPAD) array. A two-dimensional array detector was required for ISM. There was also the idea of using a conventional PMT in the early stages of development, but it is difficult to arrange the detection surface in an array in addition to its large size. Therefore, we adopted an SPPC array in which 25-pixel APDs are installed in array form.

The SPPC array used in NSPARC is paved with 25 pixels with a 50 μm × 50 μm square being one pixel (Fig. 8). The light receiving surface of the detector is only 250 μm × 250 μm, even if 25 pixels are combined. It is possible to increase the size of the detector, but increasing the size of the detector would lengthen the optical system required for focusing, which would increase the size of the device. In contrast, in the case of a small detector, a high accuracy is required for alignment adjustments. The pixel size of the detector also affects the sensitivity and noise. After various considerations, it was judged that a pixel size of 50 μm was optimal.

Although the size is smaller than that of a PMT, the parameters directly related to image quality, such as detection efficiency and wavelength range sensitivity have the

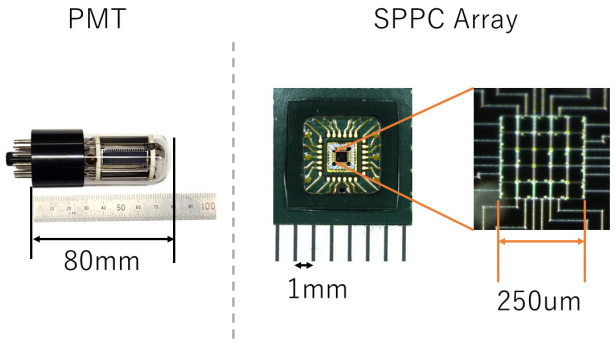

Fig. 8 PMT and SPPC array size comparison
The PMT is approximately 80 mm × 28 mm, while the SPPC array is approximately 7 mm × 7 mm.

same performance as for a PMT. From the images actually captured, it can be seen that the SPPC array images are comparable to those of a PMT (Fig. 9).

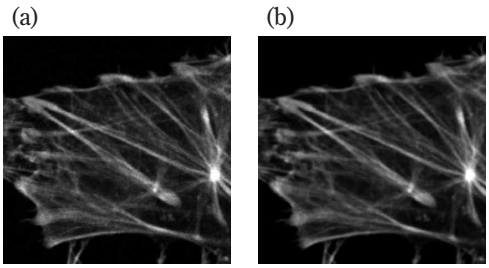

Fig. 9 Comparison between the GaAsP PMT and SPPC array
(a) Confocal image captured by the GaAsP PMT
(b) Confocal image captured by the SPPC array detector

The SPPC array also represents an improvement in terms of usability, although this does not directly affect the image quality. The sensitivity of the PMT may deteriorate when receiving strong incident light. Therefore, it is necessary to be careful to not use intense light during use. The confocal microscope AX was equipped with a safety function to stop imaging when strong light was incident. Compared with the PMT, the SPPC array receives no damage due to incident light and can be used with ease. Therefore, there is no hassle of imaging potentially being interrupted by the safety mechanism.

The process of constructing an image from the signal output of the SPPC array is described. The SPPC array is an array of APDs that multiplies a single incident photon and outputs a single electrical pulse signal. Many detectors, such as a PMT, acquire the voltage value by converting the light to the strength of the voltage and doing an AD conversion. Then, the AD-converted numerical value becomes the brightness value of the image (Fig. 10 top). However, the SPPC array outputs a unique voltage pulse regardless of the magnitude of the light intensity when the photon hits the light receiving surface. It is possible to count the number of incident photons by counting these pulses with an electric circuit. In the SPPC array, this count number becomes the brightness value of the image (Fig. 10 bottom). Thus, the SPPC array is also significantly different from the PMT in terms of the signal output method, and can realize a higher S/N and more stable measurements than a PMT in feeble light measurement.

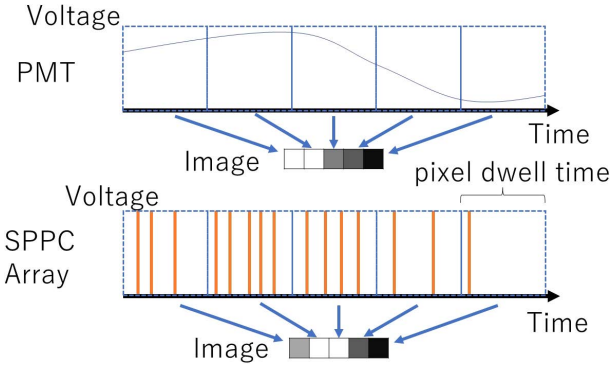

Fig. 10 Difference in image construction methods between the PMT and SPPC array
In the PMT, the strength of the analog voltage becomes the brightness value of the image, but in the SPPC array, the number of pulses counted within the time of one pixel becomes the brightness value of the image.

4 Applications using biological samples

Three applications using NSPARC are introduced. First, the images of multi-color imaging are shown in Fig. 11. The fixed HeLa cell nucleus was labeled with a fluorescent probe called DAPI, the microtubule with Alexa Fluor™ 488 (Thermo Fisher Scientific Inc-JP. Tokyo, Japan), and the mitochondrial outer membrane with Alexa Fluor™ 568 (Thermo Fisher Scientific Inc-JP.) (Fig. 11(a)). Excitation was done sequentially at three excitation wavelengths of 405, 488, and 561 nm, and imaging was captured with NSPARC. Figs. 11(b-d) show reassignment + deconvolution images, and Figs. 11(e-g) show confocal images. In NSPRAC images, the contrast and S/N are remarkably improved, and the microstructure of each organelle is clearly captured. NSPARC can improve spatial resolution in multi-color imaging, which is a conventional application of confocal microscopy, and is expected to play an active role in the study of interactions between organelles and the localization of protein molecules.

Next, images of live cell mitochondria are shown in Fig. 12. Mitochondria are composed of a double membrane consisting of the outer and inner membranes; the inner membrane has a stripe-like structure called the cristae invaginated toward the interior. MitoTracker™ Green FM (Thermo Fisher Scientific Inc-JP.) was used as a fluorescent probe to observe the cristae structure. Fig. 12(a) shows the reassignment + deconvolution image, and Fig. 12(b) shows the confocal image. The cristae, which were blurred in the latter image, could be clearly visualized in the first image with increased contrast. Next, the morphological changes of mitochondria was observed by time-lapse imaging. The morphology of mitochondria is known to change dynamically within the cell, with repeated division and fusion on a second-by-second basis. In Fig. 12(c), the time-lapse images at 1.9 fps in 3-s intervals captured the moment when minute

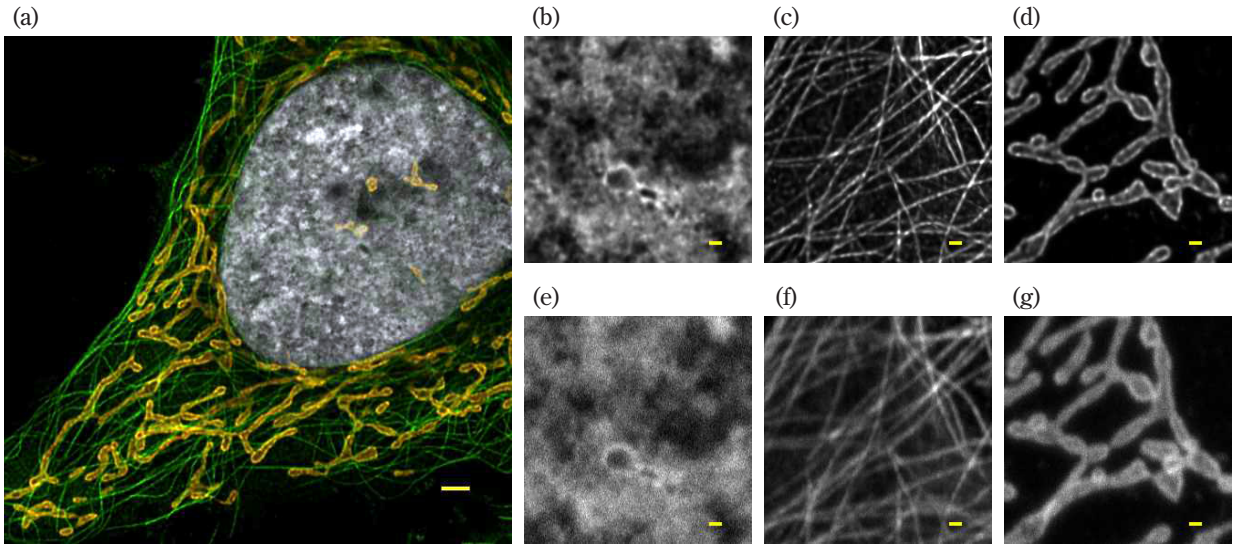

Fig. 11 Multi-color imaging images

(a) Reassignment + deconvolution image of fixed HeLa cell
White: nucleus (405 nm excitation), green: microtubules (488 nm excitation), orange: mitochondria (561 nm excitation)
Captured with a PlanAPOλD 60x 1.42 oil objective lens.
(b-d) Reassignment + deconvolution images. b) nucleus, c) microtubules, d) mitochondria
(e-g) Confocal images e) nucleus, f) microtubules, g) mitochondria
The scale bar is (a) 2 μm, (b-g) 500 nm.

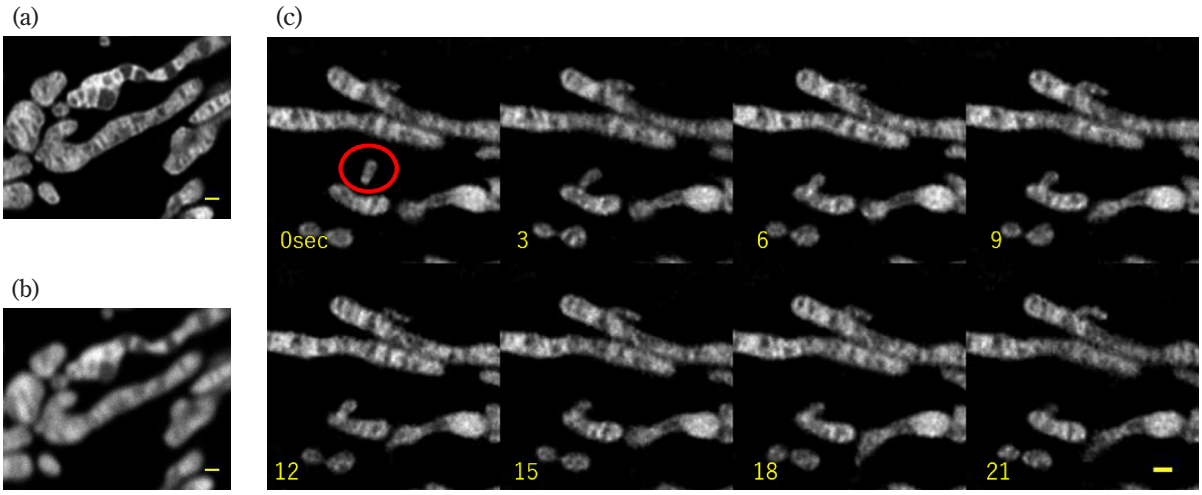

Fig. 12 Live cell imaging of mitochondria

Image of mitochondria labeled with MitoTracker™ Green FM. Captured with a PlanAPOλD 60x 1.42 oil objective lens.
(a) Reassignment + Deconvolution image and (b) Confocal image
(c) Time-lapse image of assignment + deconvolution image
Frame rate of 1.9 fps, captured in 3-s intervals.
The scale bar is 500 nm.

mitochondria of about 500 nm moved around violently and fused into large mitochondria. It is known that there is a correlation between mitochondrial morphology and cell viability, and NSPARC is expected to play an active role in the research focusing on the relationship between mitochondrial morphology and disease.

Finally, the z-stack images of the cleared mouse brain slice are shown in Fig. 13. A 5 × 5 tiling image (Fig. 13(a)) captured with a 10 × objective lens and a partially enlarged image (Fig. 13(b)) are shown. It can be seen that the neurons expressing a fluorescent protein called eYFP are densely packed. Further, the objective lens is switched to a 60x oil immersion objective lens and a z-stack image of the light blue frame part of Fig. 13(b) is captured. The three-dimensional image is shown in Fig. 13(c). The dendrites were observed to form the neural circuits and run in various directions. In addition, spiny structures called spines with a diameter of about several hundred nm could also be con-

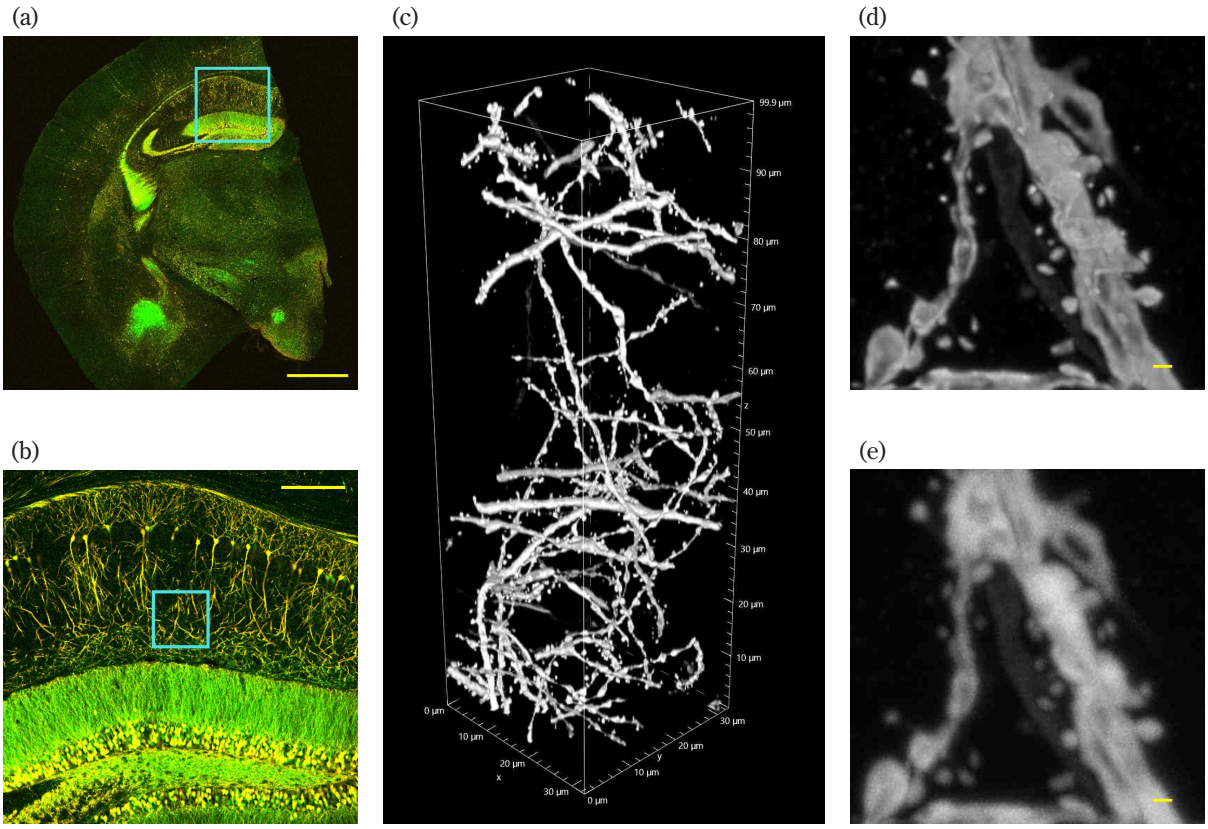

Fig. 13 z-stack images of cleared mouse brain slice

(a) Entire image of a cleared mouse brain slice. A 5 × 5 tiling confocal image captured with PlanApo10x/0.45.
(b) Enlarged confocal image of part of (a)
(c) Three-dimensional image of reassignment + deconvolution image of the light blue frame part of (b)
Captured using PlanApo λD60x 1.42 oil.
(d) Enlargement of max projection of 80–100 µm deep part of (c) (reassignment + deconvolution image)
(e) Enlargement of max projection of 80–100 µm deep part of (c) (confocal image)
Scale bar (a) 1000 µm, (b) 200 µm, (d, e) 500 nm
Sample courtesy: Lin Daniel, PhD. SunJin Lab Co.

firmed on the surface of the dendrites. Fig. 13(d) shows an enlarged part of the max projection image of the 80~100 µm deep part of the z-stack in Fig. 13(c). Compared with the confocal image in Fig. 13(e), it can be seen that the spines are not just spherical, but have various shapes. Thus, NSPARC is also useful in deep z-stack imaging.

As shown in the above three examples, NSPARC can improve the spatial resolution for general applications, such as multi-color imaging, live cell imaging , and deep imaging of confocal microscopy without trade-offs.

5 Conclusion

We believe that NSPARC equipped with ISM technology, which has no trade-offs compared with conventional confocal imaging, will become the standard for confocal microscopy in the future. In addition to the results shown in Section 4, it is possible to greatly improve spatial resolution in many confocal microscope applications. Furthermore, this technique can be expected to be widely used not only in bioimaging in academia, but also in industrial fields, such as in drug efficacy evaluation and toxicity testing in drug discovery. For example, we can image cancer invasion in 3D cultured cells by utilizing the deep imaging capability of NSPARC, and image morphological changes due to drug responses in mitochondria and nerve cells sensitive to light damage by utilizing low phototoxicity. It is expected that new evaluation indices such as morphological changes of organelles and protein localization, which have been unobservable or overlooked so far, will be discovered, leading to an improved efficiency and accuracy of drug efficacy evaluation.

Acknowledgments

We would like to emphasize that NSPARC is the result of joint research with Nanoscopy, and Molecular Microscopy and Spectroscopy Labs at Istituto Italiano di Tecnologia,

Genoa, Italy.

We would like to thank Professor Alberto Diaspro, Dr. Paolo Bianchini, Dr. Giuseppe Vicidomini, and all the Laboratories staff for their great support and cooperation.

We would like to take this opportunity to once again express our gratitude.

References

[1] A. Diaspro, *Confocal and Two-Photon Microscopy Foundations, Applications, and Advances*, New York: Wiley-Liss, 2001.

[2] C. B. Müller and J. Enderlein, "Imaging Scanning Microscopy," *Phys. Rev. Lett.*, Vol. 104, no. 19, 198101, 2010.

[3] C. J. R. Sheppard, "Super-resolution in confocal imaging," *Optik*, Vol. 80, no. 2, pp. 53–54, 1988.

[4] M. Castello *et al.*, "Image scanning microscopy with a quadrant detector," *Optics Letters*, Vol. 40, no. 22, pp. 5355–5358, 2015.

[5] M. Castello *et al.*, "A robust and versatile platform for image scanning microscopy enabling super-resolution FILM," *Nature methods*, Vol. 16, pp. 175–178, 2019.

大川潤也　Junya OHKAWA
ヘルスケア事業部 技術統括部 システム開発部
System Development Department
Technology Solutions Sector
Healthcare Business Unit

小森谷大介　Daisuke KOMORIYA
ヘルスケア事業部 技術統括部設計部
Designing Department
Technology Solutions Sector
Healthcare Business Unit

楠井雄太　Yuta KUSUI
光学本部 第一設計部
1st Designing Department
Optical Engineering Division

産業用カメラ「LuFact」シリーズの開発

笹井義史，大河内潤，中野雅弘，吉岡玄史，金丸謙介，本　佳弥，近藤俊介

Development of Industrial Camera “LuFact” Series

Yoshifumi SASAI, Jun OKOCHI, Masahiro NAKANO, Genshi YOSHIOKA,
Kensuke KANAMARU, Yoshiya MOTO and Shunsuke KONDO

「LuFact（ルファクト）」は，ニコンが長年コンシューマー向けカメラ製品で培ってきた信頼性の高い技術を搭載した産業用カメラである．2022年７月に GigE Vision に対応した A1000-G，USB3 Vision に対応した A1000-U と高感度200万画素のモノクロカメラ AH020-MR，800万画素のモノクロカメラ AH080-MR の２種類のカメラヘッドを発売した．また，2023年３月に GigE Vision，および，AI 処理が可能な処理ユニット A2000-G と800万画素のカラーカメラ AH080-CR，500万画素のグローバルシャッター方式のモノクロカメラ AH050-MG，CH050-MG の３種類のカメラヘッドを開発した．
ここでは，LuFact シリーズの開発要素について説明する．

“LuFact” is an industrial camera equipped with highly reliable technology that Nikon has cultivated over several years under its consumer camera product category.
In July 2022, A1000-G, A1000-U, and two types of camera heads, AH020-MR and AH080-MR, were released. In March 2023, we developed the A2000-G and three types of camera heads: AH080-CR, AH050-MG, and CH050-MG.
This section describes the development elements of the LuFact series.

Key words 産業用カメラ，GigE ビジョン，EtherNet/IP，高信頼性，エッジコンピューティング
industrial camera, GigE Vision, EtherNet/IP, high reliability, edge computing

1 Introduction

“LuFact” is an industrial camera that is equipped with highly reliable technology that Nikon has cultivated over many years in consumer camera products. In July 2022, A1000-G/A1000-U and two types of S-mount camera heads AH020-MR and AH080-MR were released. In March 2023, the AI processing unit A2000-G, two types of S-mount camera heads AH080-CR and AH050-MG, and one type of C-mount camera head CH050-MG were released (Fig. 1).

Here, we explain the development elements of the LuFact series.

2 Compact and separate design

The camera head with the image sensor was separated from the image processing unit with the image processing Integrated Circuit (IC) to achieve an ultra-compact camera head. The dimensions of the S-mount model camera head are 20 mm × 20 mm when viewed from the mount surface. However, through strategic optimization of the board layout and component placement, it remains fully compatible with 1/1.8-inch 8-megapixel image sensors (Fig. 2). This achievement in miniaturization also enhances the adaptability of the camera head for integration into exist-

Fig. 1　LuFact series

Fig. 2　Camera head (S mount)

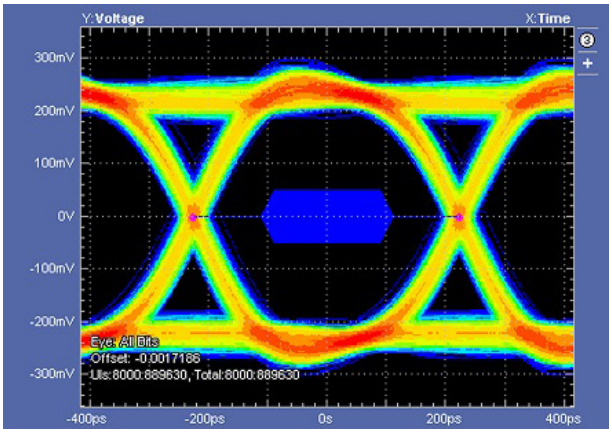

Fig. 3 Differential signal eye pattern (cable length: 10 m)

ing equipment and production lines.

Moreover, advancements in cable design allow for the extension of the cable length between the camera head and the main unit up to 10 meters. This accomplishment is facilitated by an embedded clock type differential signal, engineered to support long-distance transmission. The incorporation of optimized wiring patterns and an equalizing function further counteracts the signal attenuation inherent to extended distances (Fig. 3).

A significant benefit arises from the segregation of the image processing unit, a notable source of heat generation, from the camera head. This separation significantly reduces temperature rise in the camera head, preventing potential instances of overheating-related camera stoppages. Furthermore, this feature renders the camera head suitable for attachment to devices where temperature-related impacts must be minimized or avoided.

3 Supported communication standards

With LuFact, multiple communication standards are supported, and they can be used according to the customer's usage environment and purpose.

Currently, the communication standards supported by the A2000-G are 1. GigE vision standard, 2. RTSP/RTP streaming standard, and 3. EtherNet/IP standard. Here, we describe each standard and its application in A2000-G.

3.1. GigE vision standard

The GigE vision standard is an image transfer standard that is standardized by the Association for Advancing Automation (AAA), an automation ecosystem industry group in the United States. It is mainly intended for applications to industrial digital cameras and their counterparts (e.g., application software running on Personal Computers (PCs). Gigabit Ethernet was used as the lower layer of the communication protocol, facilitating the use of low-cost standard cables and network equipment, as well as long-distance, high-speed image transfer. Standard-compliant products can be interconnected, and hundreds of standard-compliant products are offered by companies worldwide.

The GigE vision standard consists of three parts: device detection, GigE Vision Control Protocol (GVCP), GigE Vision Stream Protocol (GVSP), and format (Fig. 4). GenICam and SFNC were also adopted as software interface standards.

The A2000-G is set so that GigE standard-compliant application software automatically starts when shipped from the factory. Moreover, we provide LuFact Utility application software that runs on a PC, enabling users to operate the A2000-G as a GigE standard camera immediately after purchasing the A2000-G.

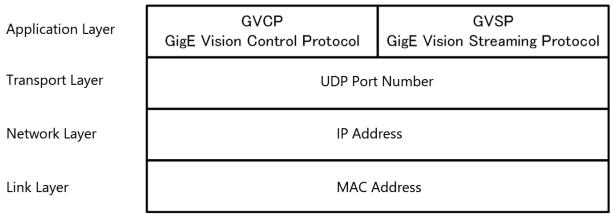

Fig. 4 GigE Vision

3.2. RTSP/RTP Streaming standard

RTSP stands for “Real Time Streaming Protocol” and is a streaming control protocol that is standardized as RFC2326 by Internet Engineering Task Force (IETF). RTP is an abbreviation for “Real Time Transport Protocol”. RTP is standardized as RFC3550 by IETF, and is a data communication protocol that provides real-time delivery of data streams such as voice and video. UDP is used for the lower streaming layer (Fig. 5).

RTP is used together with RTCP, and the main roles of RTP are jitter compensation and data loss detection.

The A2000-G uses the RTSP/RTP protocol for the LuFact Streaming application software. RTSP involves the implementation of only the required methods (DESCRIBE, OPTIONS, PLAY, SETUP, TEARDOWN) on TCP/IP (settings related to images are implemented in a different way).

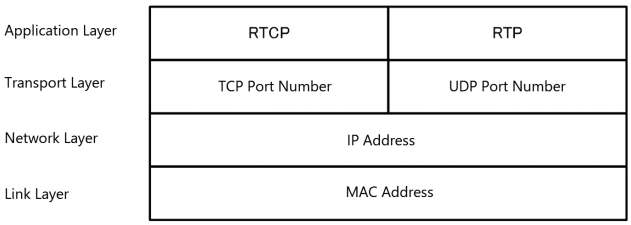

Fig. 5 RTSP/RTP

Notably, RTP has no audio, and the images are transferred after applying the MPEG/AVC (H.264) encoding format.

3.3. EtherNet/IP Standard

EtherNet/IP represents an industrial networking standard built upon the foundation of Ethernet, designed to offer simultaneous connectivity for Internet, enterprise, and industrial automation applications. The architecture incorporates a two-layer structure, with the application layer employing the Common Industrial Protocol (CIP), while the lower layer employs the Transmission Control Protocol (TCP) and User Datagram Protocol (UDP) for data transmission (Fig. 6).

EtherNet/IP is versatile, serving various communication needs across control and information levels. Beyond EtherNet/IP's scope, CIP encompasses additional protocols such as CompoNet, catering to sensor and actuator communication, and DeviceNet, tailored for device-level interactions. These protocols are accompanied by features like communication security, time synchronization, and multi-axis motion control. Leveraging the CIP network's capabilities, developers can create application software capable of comprehensively managing entire systems.

Managing and certifying the CIP standards, including EtherNet/IP, is the responsibility of the Open DeviceNet Vendors Association (ODVA), a non-profit organization headquartered in the United States. Broadly speaking, two types of communication are supported: implicit communication, which is periodic communication; and explicit communication, which allows communication at arbitrary timing such as events. It is characterized by its high compatibility with TCP/UDP/IP compared to other industrial networks.

The A2000-G adopts this EtherNet/IP communication standard and uses EtherNet/IP for communication with a programmable logic controller (PLC).

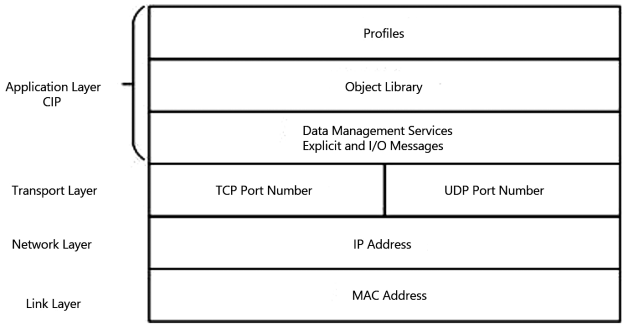

Fig. 6 EtherNet/IP

4 Performance in dark settings

The AH020-MR camera head is equipped with a back-illuminated monochrome high-sensitivity image sensor with 2.13 effective megapixels. A small amount of light can be converted into electrical signals even in environments where lighting equipment cannot be installed. Notably, it is possible to acquire a clear image without installing an illumination device while suppressing noise amplification by gain (Fig. 7).

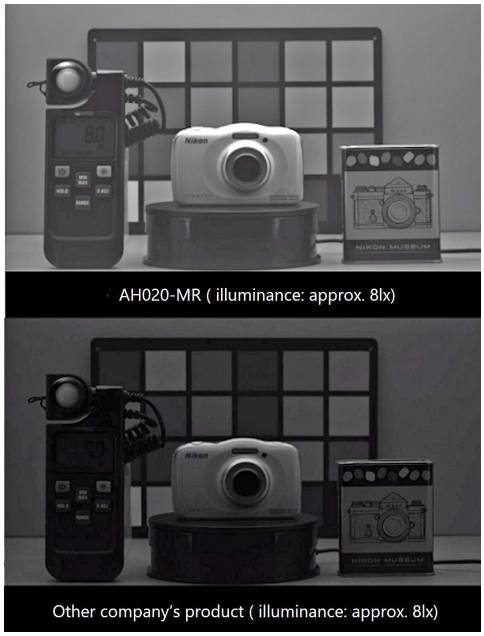

Fig. 7 AH020-MR performance in dark settings

5 High reliability

Industrial cameras must operate continuously 24 hours a day, 365 days a year. Hence, temperature is one of the factors that must be controlled for stable operation. We repeated thermal simulations so that the unit could withstand high-load image processing, and determined the shape of the heat sink and size of the cooling fan (Fig. 8). Stable operation was achieved without stopping operation owing to overheating protection (thermal shutdown), even at maximum load.

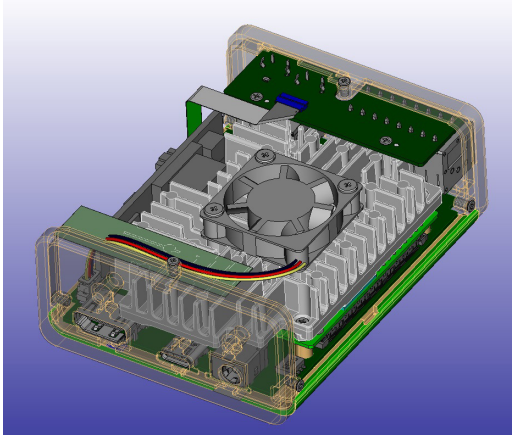

Fig. 8 High reliability

Fig. 9　Inspection of missing parts

6 Edge computing

The LuFact A2000-G incorporates a Central Processing Unit (CPU) with Artificial Intelligent (AI) capabilities, enabling it to inspect missing components without the need to transfer image data to a separate PC or server (Fig. 9). Integration of a barcode reader allows for the retrieval of serial numbers, which can then be correlated with inspection data. Should a defect be detected, the system can trigger actions such as activating PLCs or illuminated signal lights to promptly indicate abnormalities.

7 Conclusion

The LuFact series serves a dual purpose, catering not only to traditional industrial cameras but also facilitating inspection through edge computing. By leveraging Nikon’s image analysis technology and AI capabilities, we aim to contribute to the realization of smart factories. Lastly, we extend our heartfelt appreciation to the numerous individuals who have played a pivotal role in the development of the LuFact series.

笹井義史　Yoshifumi SASAI
デジタルソリューションズ事業部 第二開発・技術部
2nd Development Department
Digital Solutions Business Unit

大河内潤　Jun OKOCHI
デジタルソリューションズ事業部 第二開発・技術部
2nd Development Department
Digital Solutions Business Unit

中野雅弘　Masahiro NAKANO
デジタルソリューションズ事業部 第二開発・技術部
2nd Development Department
Digital Solutions Business Unit

吉岡玄史　Genshi YOSHIOKA
デジタルソリューションズ事業部 第二開発・技術部
2nd Development Department
Digital Solutions Business Unit

金丸謙介　Kensuke KANAMARU
デジタルソリューションズ事業部 第二開発・技術部
2nd Development Department
Digital Solutions Business Unit

本　佳弥　Yoshiya MOTO
デジタルソリューションズ事業部 第二開発・技術部
2nd Development Department
Digital Solutions Business Unit

近藤俊介　Shunsuke KONDO
デジタルソリューションズ事業部 第二開発・技術部
2nd Development Department
Digital Solutions Business Unit

研究開発論文

Research and Development Reports

ガスタービン用TBCへのレーザー加工によるリブレット形成と熱サイクル耐久性評価†

綿引健二，蘆田憲一，土橋晋太郎，土橋広和

Riblet Patterning by Laser Ablation on the Thermal Barrier Coating (TBC) for Gas Turbines and Evaluation of Its Resistance to Cyclic Heating

Kenji WATAHIKI, Kenichi ASHIDA, Shintaro TSUCHIHASHI and Hirokazu TSUCHIHASHI

コンプレッサーブレードやタービンブレードの表面にリブレットを形成すると，ガスタービンの性能を向上させることができる．我々は典型的な遮熱コーティング（TBC）上へのリブレット施工の適用性を調査した．レーザー加工により，所定の形状に沿ったリブレット加工が実現できることが確認できた．リブレット構造の耐久性は，熱サイクル試験を実施して評価した．リブレットがある場合とない場合の結果を比較すると，TBCが剥がれるまでの繰り返し回数にも，熱成長酸化物（TGO）層の成長速度にも有意差は見られなかった．また，試験前後でリブレット形状に変化は見られなかった．以上のことから，高温環境下で使用されるTBCにレーザー加工を施すことで，耐剥離性に影響を与えることなくリブレットを形成できることがわかった．

Forming riblets on the surface of a compressor blade or turbine blade can improve a gas turbine's performance. We investigated the applicability of patterning riblets on a typical thermal barrier coating (TBC). It was verified that a riblet structure conforming to a predetermined shape can be realized by laser processing. We evaluated the riblet structure's durability by conducting a thermal cycle test. Comparing the results obtained with- and without-riblet cases, no significant difference was observed in the number of repetitions until TBC peel off, nor in the rate of growth of the thermally grown oxide (TGO) layer. In addition, no significant change was observed in the riblet shape before and after the test. Accordingly, it was determined that laser processing can produce riblets on TBCs used in high temperature environments without adversely affecting peel resistance.

Key words ガスタービン，リブレット，レーザー加工，熱サイクル試験，遮熱コーティング
gas turbine, riblet, laser processing, cyclic heating test, thermal barrier coating

1 はじめに

ガスタービンをはじめとする流体機器の効率の向上は大きな課題の一つである．流体抵抗は圧力抵抗（慣性抵抗）と摩擦抵抗（粘性抵抗）に大別され，特に高レイノルズ数の乱流領域においては，層流に比べて大きな壁面乱流摩擦抵抗が発生する［2］．乱流摩擦抵抗を低減させるために，流体機器表面に微小な縦溝を施工する手法がある．リブレット（riblet）と呼ばれる，サメの鱗［3］，［4］のような35～100 μm程度の微小な縦溝が表面に存在すると，平滑面に対して，8～10%程度の乱流摩擦抵抗の低減を引き起こすことが実験的にも明らかにされている［5］．

我々は，上記のリブレット形状をレーザーアブレーション加工により形成する技術を開発し，ガスタービンの圧縮機やタービン翼への適用を検討している．レーザーアブレーション（laser ablation）とは，ナノ秒，ピコ秒，フェムト秒のパルス幅を持つ極短パルスレーザーによって非熱的に材料表面の物質を除去する技術である［6］，［7］．この技術を用いて，任意の形状を材料表面に形成する事ができる．また，ガスタービンの圧縮機やタービン翼には，各種合金の他，金属・セラミックの様々なコーティングが用いられる［8］，［9］が，レーザーアブレーション技術を用いれば，それら部材表面にもリブレットの直接加工を行う事が可能である．

我々は，これまでにリブレットの優位性の検証のため，流体解析（CFD）に基づいて設計したリブレットを金属製のタービン翼にレーザー加工で形成し，その効果の実測を行ってきた．タービンテスト設備の出口案内翼（静翼）に

† 本稿は，自著の引用文献［1］に対して，追加の実験結果と考察を加えたものである．

リブレットを形成した評価で，リブレットによる圧損低減効果の実測を行い，その優位性を示す事ができた［10］．さらに，超小型ジェットエンジンの各翼にリブレット加工を行い，推力や燃料効率の向上を実験で確認する事ができた［11］．

ところで，過酷な環境で動作するガスタービン部材に適用する場合，耐久性も重要な要素である．機械特性に関して，これまでに圧縮機部材およびコート材にリブレット加工を施した試験片を準備し，引張・クリープ・疲労試験を実施して，その特性を評価した．その結果，金属部材に直接加工を行うと疲労強度が低下するが 適切なコーティングの選択と施工を行う事で，疲労強度を招く事なく低下を防ぎ，リブレット形状を形成できる事が分かった［12］．

1000℃以上の高温になるガスタービン翼では，遮熱コーティング（TBC）が広く用いられるが，長期間使用するとTBC のトップコートとボンドコートの界面で thermally grown oxide（TGO）と呼ばれる酸化層が徐々に成長して，やがて剥離が生じる．そのため，TBC では剥離挙動の確認や TGO を抑制する事が重要視されている［13］–［16］．トップコートにリブレットを形成した場合，その表面積の増大による酸化特性や遮熱特性の変化により，剥離挙動が変化する可能性がある．そこで我々は，TBC へリブレットを形成したサンプルを作成し，その適用可能性を評価した．また，サンプルに熱サイクル負荷を掛けて，剥離に至るまでの熱サイクル回数比較や負荷前後の試験片を観察する事で，リブレット形成による剥離挙動の影響を評価した．

2 リブレット加工

リブレットの加工にはレーザーアブレーション加工の開発機を用いた．Fig. 1 にその模式図を示す．このレーザー加工機は，波長 532 nm（緑色），パルス幅約 15 ps，最大繰返し周波数 4 MHz，最大出力 50 W の短パルスレーザーを持つ．レーザー光は照射ヘッドに導かれ，ガルバノミラーによって同期してスキャンされる．レーザー光はｆθレンズによって所定の位置に集光される．加工対象物は 3 軸ステージによって所定の XYZ 位置に駆動できる．レーザー光が集光した対象物の表面の物質はアブレーションにより除去され，これを連続的にスキャンすることでリブレットの溝が形成される．各条件を制御する事で，ピッチや深さ，リブレット形状を制御する事が可能である．

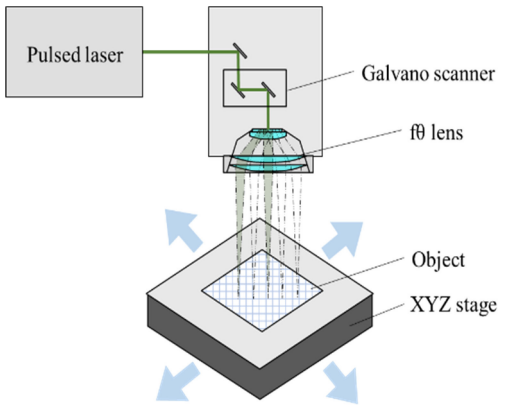

Fig. 1　Schematic diagram of a laser processing machine for forming riblets on the surface of an object

3 実験方法

3.1. 試験片

試験片の模式図を Fig. 2 に示す．基材にボンドコートとトップコートを形成したものを用意し，トップコートの表面にリブレット加工を施した．基材はガスタービン翼で用いられる Ni 基超合金である IN738LC を ϕ25×5 mm の円柱形状に加工したものを用いた．試験に用いた IN738LC の組成は Table 1 の通りである．各コートの組成・厚みは Fig. 2（a）に示す通りである．リブレット加工は，ピッチと深さの目標値をそれぞれ 50 μm，25 μm として加工を行った．この寸法は，流体低減効果を確認しているものの中で，代表的なサイズである．比較のため，リブレット加工を行っていない試料も用意した．

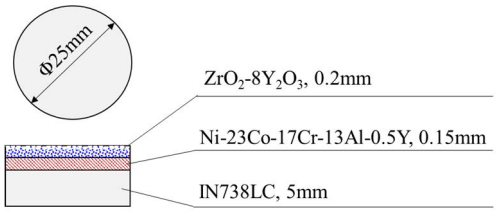

(a) Materials and geometry

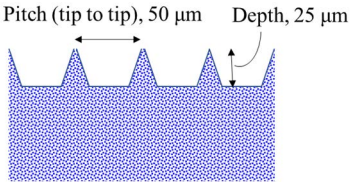

(b) Dimension of riblet

Fig. 2　Test sample

Table 1　Chemical composition of IN738LC（wt%）

C	Si	Mn	Ni	Cr	Mo
0.11	<0.01	<0.01	Bal.	15.9	1.69
Co	W	Al	Ti	Fe	Ta
8.31	2.60	3.46	3.45	0.05	1.74

3.2. 熱サイクル試験

試験は JIS H8451準拠して実施した．Fig. 3に試験機および試験条件の模式図を示す．Fig. 3（a）の通り，円筒状の石英管内に試料台があり，円筒周囲にヒーターと制御用熱電対を備えている．制御温度により，自動でヒーターの

On/Off および位置を動かす事で所定の時間・温度サイクルでの試験が可能である．本試験では，Fig. 3 (b) に示す通り，1100℃と250℃の温度制御で熱サイクルを繰り返し負荷するようにヒーターの動作を調整した．試験機の構成上，円筒軸方向には温度分布が生じうるため，リブレット加工有無の試験片を 4 個ずつ用意し，Fig. 3 (c) のように試料台の上に並べて，同じ温度条件でリブレットの影響を比較できるようにした．Fig. 3 (d) は試験時の様子を示した写真である．

剥離の判定は目視で実施した．夜間を含めて 5 回/1日の頻度で確認を行い，剥離が観察された場合は，前回の確認時回数と剥離確認時回数の中間の回数を剥離回数として採用し，リブレット加工有無で比較した．また，剥離試験後の試験片をレーザー顕微鏡と電子顕微鏡（SEM）での観察，エネルギー分散型X線分析（EDS）による元素分析を行い，試験前後のリブレット形状の変化やボンドコートとトップコートの界面の酸化膜の評価を行った．

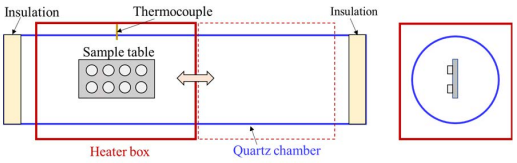

(a) Equipment of the heat cycle test equipment

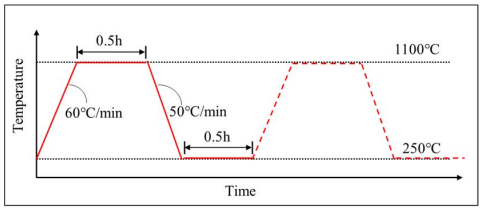

(b) Target temperature profile around the sample table

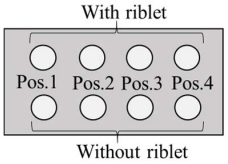

(c) Sample placement

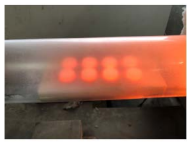

(d) Photographs of the samples during the test

Fig. 3 Schematic diagram of the test bench for evaluation of the thermal cycle resistance

4 実験結果および考察

4.1. TBC へのリブレット加工の適用可能性

Fig. 4 に加工したリブレット形状をレーザー顕微鏡で評価した結果を示す．目標値の深さ 25 μm，ピッチ 50 μm で周期的な溝構造が形成出来ている事が分かる．SUS304，SUS630に加工した結果［12］と比較しても，ばらつきや欠陥が少なく，狙い通りの寸法形状に加工が出来ている事が分かる．

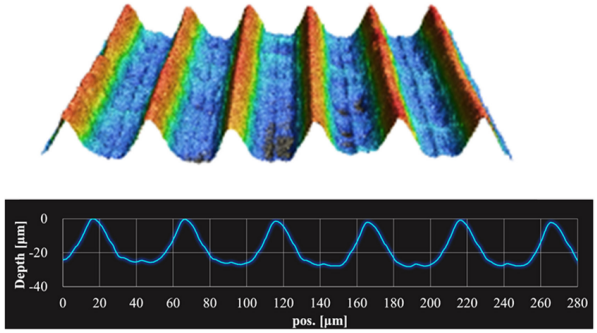

Fig. 4 Microscopic profiles of the lasered riblet TBC sample

4.2. 熱サイクル試験結果

Fig. 5 に熱サイクル試験の結果を示す．1026 サイクルまで試験を実施した所，Pos. 4以外の試験片はボンドコートとトップコートの間で剥離が観察された．剥離に至るサイクル回数は試験片の設置位置により，大きく差異が見られた．一方で，同じ温度条件と考えられる同じ設置位置で比較すると，リブレット加工有無で，剥離回数に差異は見られなかった．

試料位置に温度条件の差異を調べるため，熱サイクル試験後に試料位置付近の温度を計測した結果を Fig. 6 に示す．Pos. 3，4と比較して，Pos. 1，2は低温側の到達温度および降温速度が大きく，熱負荷が大きい条件であると推測される．そのため，より少ないサイクル数で剥離が生じたと考えられる．この事から，試料位置による剥離に至るサイクル数の差異は，熱負荷が異なっていたためと考えられる．

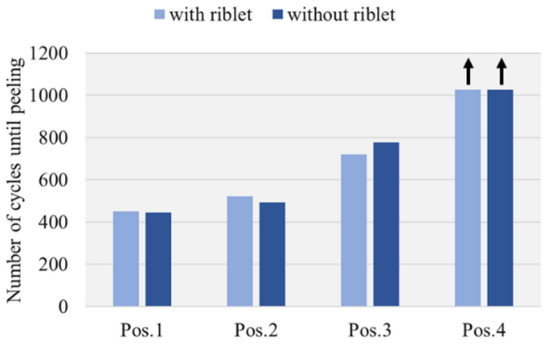

Fig. 5 Comparison of the number of cycles to delamination with riblet and without riblet sample

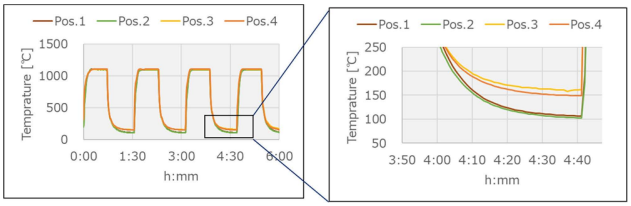

Fig. 6 Differences in temperature profile depending on sample placement position

4.3. リブレットの剥離寿命への影響

剥離した要因を調査するため，剥離が見られなかったPos. 4の試験片を熱サイクル試験後に SEM/EDX にて，断面観察および元素分析を行った．Fig. 7 に SEM 観察結果を示す．リブレット加工有無の試験片のどちらもトップコートとボンドコートの界面付近にき裂が見られた．それぞれき裂が開口していない部分（1）と開口した部分（2）の観察結果を示している．このき裂が進展して，全域が開口した時に剥離が生じると考えられる．Pos. 4の試験片は，開口していない部分が残っており，熱サイクル試験で剥離に至らなかったと考えられる．一方で，リブレット加工有無の試料間を比較すると，トップコート全体および表面やリブレット加工周辺のき裂や空孔の大きさや密度に差異は見られなかった．

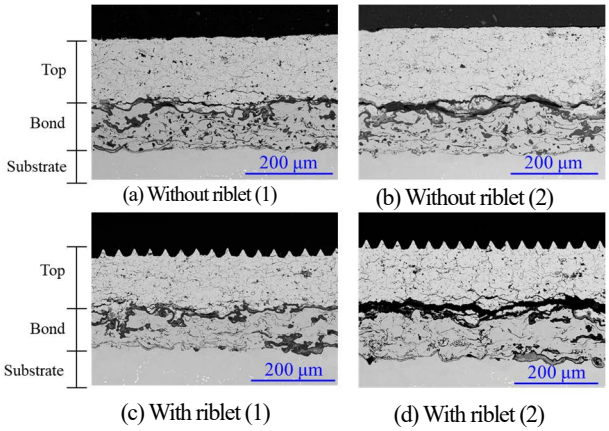

Fig. 7 Cross-sectional microstructure SEM images of lasered riblet TBC sample after heat cycle test (Pos. 4)

Fig. 8 に EDS 分析結果を示す．Fig. 7 の SEM 像の（2）の領域でマッピング分析を行った．Zr が検出される領域がトップコート，Ni，Co，Cr が検出される領域が，ボンドコートと基材に対応している．ボンドコートとトップの界面に Al と O の成分が観察された．これは TBC を長期間高温で加熱する事で生成した界面酸化物（Al_2O_3）と考えられる．一般に，このような熱的に生成成長した酸化物を TGO といい，この TGO が剥離寿命に大きく影響すると言われている［13］−［16］．リブレット加工有無の試料でこの TGO の厚みや生成箇所に明確な差異は見られなかった．

以上の事から，今回の熱サイクル試験での剥離は，一般的な TBC の剥離挙動と同様に熱サイクルを繰り返す事で熱応力が生じ，横方向のき裂が発生・成長し，全面に進展したのちに生じたものと考えられる．Pos. 3，4と比較して，Pos. 1，2では温度勾配が大きく，き裂の発生・進展速度が速いため，少ないサイクル数で剥離が生じたと考えられる．一方で，リブレット加工有無でき裂や TGO の生成・進展に差異は見られず，リブレット加工はこれらに影響を与えなかったため，リブレット加工有無で剥離寿命に差異が生じなかったと考えられる．

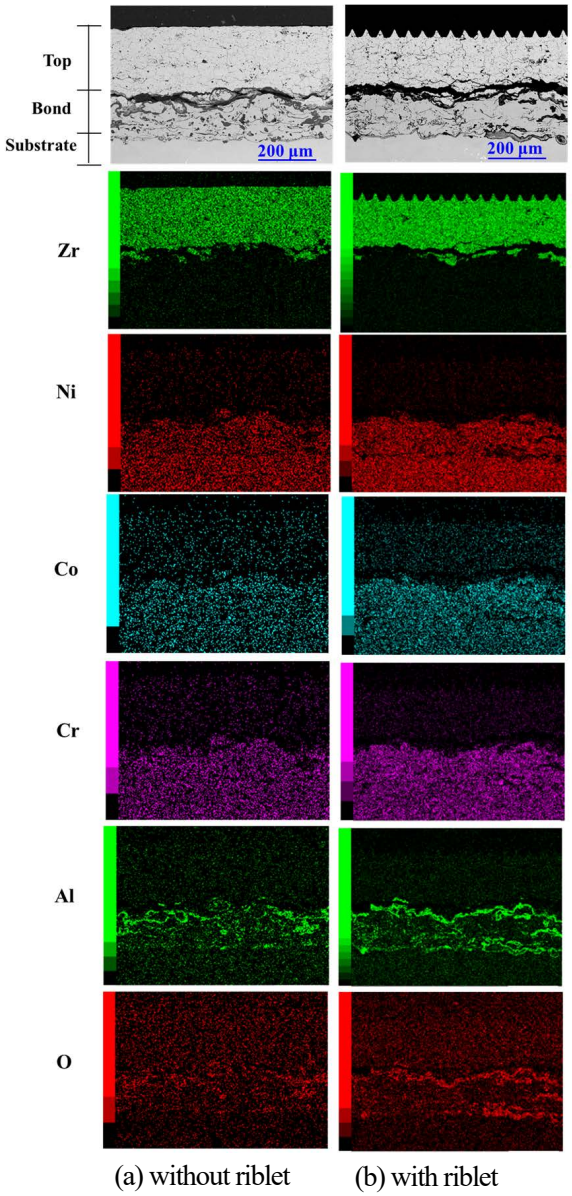

Fig. 8 EDS mapping result of the lasered riblet TBC sample after heat cycle test (Pos. 4)

4.4. リブレットの高温耐久性

高温および熱サイクル負荷によるリブレットの耐久性を評価するため，試験後の試験片をレーザー顕微鏡で評価した．剥離前と剥離後の試験片それぞれ観察を行った．Fig. 9 にその結果を示す．どちらの試験片も Fig. 4 の熱サイクル試験前の形状から変化は見られなかった．1100℃の高温を伴う熱サイクルで剥離が生じるまで負荷を掛けてもリブレット形状に変化が見られなかった事から，熱サイクル環境下に対するリブレット形状の耐久性は十分であると考えられる．

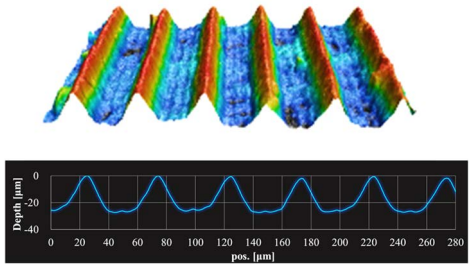

(a) After delamination (Pos. 3 sample)

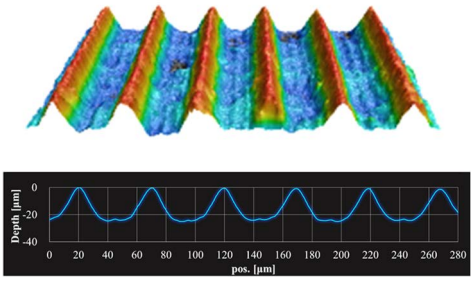

(b) Before delamination (Pos.4 sample)

Fig. 9 Microscopic profiles of the lasered riblet TBC sample after heat cycle test

5 まとめ

レーザー加工により，TBC のトップコート上へのリブレット形成を行い，その加工の適用性および熱サイクルによる耐久性を評価した．TBC 上にリブレットを形成できる事が分かった．また，リブレット有無で剥離寿命および剥離挙動に差異は見られず，熱サイクル負荷後もリブレット形状は維持できる事が分かった．

以上の事から，性能向上が見込めるリブレットを剥離寿命に影響を与えずに TBC 上に形成する事が可能であり，ガスタービンの性能向上策として有用であると考えられる．

引　用　文　献

［1］綿引健二，蘆田憲一，土橋晋太郎，土橋広和，内藤兼行，佐藤真路，一ノ瀬剛，“ガスタービン用 TBC へのレーザ加工によるリブレット形成と熱サイクル耐久性評価，”*第50回日本ガスタービン学会定期講演会*，A-14, 2022.

［2］三宅裕，“壁乱流の渦，”*ながれ*，vol. 22, no. 1, pp. 29–34, 2003.

［3］鈴木雄二，笠木伸英，“壁面乱流の知的能動制御，”*セーブメーション・レビュー　マイクロフローセンサ特集号*，pp. 50–57, 2001.

［4］D. W. Bechert, G. Hoppe, and W.-E. Reif, “On the drag reduction of shark skin,” in *Proc. 23rd Aerospace Sciences Meeting*, 1985, doi: 10.2514/6.1985-546.

［5］D. W. Bechert, M. Bartenwerfer, G. Hoppe, and W.-E. Reif, “Drag reduction mechanisms derived from shark skin,” in *Proc. 15th Congr. ICAS*, pp. 1044–1068, September, 1986.

［6］B. N.Chichkov, C. Momma, S. Nolte, F. von Alvensleben, and A. Tünnermann, “Femtosecond, Picosecond and Nanosecond Laser Ablation of Solids,” *Appl. Phys. A*, vol. 63, no. 2, pp. 109–115, 1996.

［7］M. C. Richardson, “New Opportunities with Intense Ultra-Short-Pulse Lasers,” in *Proc.of SPIE*, vol. 1410, 1991, pp. 14–25, doi: 10.1117/12.43608.

［8］吉岡洋明，土井裕之，武田淳一郎，難波浩一，岡田郁生，武浩司，伊藤健之，“発電用ガスタービンの材料技術，”*日本ガスタービン学会誌*，vol. 32, no. 3, pp. 4–47, 2004.

［9］R. Rajendran, “Gas turbine coatings - An overview,” *Engineering Failure Analysis*, vol. 26, pp. 355–369, 2012, doi: 10.1016/j.engfailanal.2012.07.007.

［10］白石雅之，土橋晋太郎，一ノ瀬剛，柴崎祐一，P. A. Leitl, A. Flanschger，S. Schreck，R. Benauer，S. Pramstrahler, and A. Marn，“タービンテストリグ出口案内翼への最適リブレット効果予測と，そのレーザー加工によるリブレット性能評価，”*第49回日本ガスタービン学会定期講演会*，A-24, 2021.

［11］稲崎慎也，佐藤真路，一ノ瀬剛，P. A. Leitl，A. Flanschger, S. Schreck, and R. Benauer，“超小型ジェットエンジンの最適リブレット計算とそのレーザ加工，およびエンジン性能での効果検証，”*第49回日本ガスタービン学会定期講演会*，A-25, 2021.

［12］綿引健二，蘆田憲一，土橋晋太郎，土橋広和，佐藤真路，一ノ瀬剛，“ガスタービン圧縮機部材へのレーザ加工による，リブレット形成と機械特性評価結果，”*第49回日本ガスタービン学会定期講演会*，B-27, 2021.

［13］岡田満利，“発電用ガスタービン高温部品の寿命評価のための材料技術，”*日本ガスタービン学会誌*，vol. 45, no. 6, pp. 452–457, 2017.

［14］K. M. Doleker, Y. Ozgurluk, and A. C. Karaoglanli, “TGO growth and kinetic study of single and double layered TBC systems,” *Surface and Coatings Technology*, vol. 415, 127135, pp. 1–11, 2021, doi: 10.1016/j.surfcoat.2021.127135.

［15］児島慶享，“ガスタービン耐熱コーティング開発の最新技術動向，”*日本ガスタービン学会誌*，vol. 38, no. 2, pp. 85–90, 2010.

［16］有川秀行，児島慶享，吉岡隆幸，岡田満利，久松暢，“遮熱コーティング（TBC）の高耐久化の検討（柱状組織トップコート及び界面酸化物の成長抑制について），”日本機械学会（No. 04-2）*第 9 回動力エネルギー技術シンポジウム講演論文集*（’04.6.22,23, 東京），pp. 119–122, 2004.

綿引健二　Kenji WATAHIKI
次世代プロジェクト本部 第一開発部
1st Development Department
Next Generation Project Division

蘆田憲一　Kenichi ASHIDA
次世代プロジェクト本部 第一開発部
1st Development Department
Next Generation Project Division

土橋晋太郎　Shintaro TSUCHIHASHI
次世代プロジェクト本部 第一開発部
1st Development Department
Next Generation Project Division

土橋広和　Hirokazu TSUCHIHASHI
次世代プロジェクト本部 第一開発部
1st Development Department
Next Generation Project Division


綿引健二
Kenji WATAHIKI


蘆田憲一
Kenichi ASHIDA


土橋晋太郎
Shintaro TSUCHIHASHI


土橋広和
Hirokazu TSUCHIHASHI

広角ダブレットメタレンズに於ける誘電体メタサーフェス素子の種類の違いによる影響

鳥羽英光，髙木英嗣，大橋道雄，大滝　桂，瀧川雄一

Influence on Wide-Angle Doublet Metalenses Due to Different Types of All-Dielectric Metasurfaces†

Hidemitsu TOBA, Hidetsugu TAKAGI, Michio OHASHI, Katsura OTAKI and Yuichi TAKIGAWA

ダブレットメタレンズは，約30度の入射角度まで回折限界の集光が可能であることが先行文献で示されている．この結果は，メタレンズが斜め入射でも有効に機能することを示している．また，様々なメタアトムが提案されているが，どのようなメタアトムが斜め入射に強いかを比較した報告は私たちの知る限りない．そこで我々はまず，3種類のメタアトムの入射角依存性を数値的に計算した．その結果，導波路型構造が斜め入射に対して最もロバストであることがわかった．次に，円筒形ダブレットメタレンズについて電磁場シミュレーションを行い，マイクロポスト型と導波路型の比較を行った．これらの結果から，導波路型メタサーフェスは，先行文献のダブレットレンズの性能をさらに向上させる可能性があることが分かった．

It has been shown in previous literature that nearly diffraction limited focusing is possible by a doublet metalens up to almost 30 deg. This result indicates that metalenses can work well, even at oblique incidence. Although various meta-atoms have been proposed, as far as we know, there is no report that compares what kind of meta-atom is robust against oblique incidence. Here, we first numerically calculated the incident angle dependence of the three types of meta-atoms. The results show that the waveguide-type structure is the most robust to oblique incidence. Next, we performed rigorous electromagnetic simulations for the cylindrical doublet metalenses to compare the micropost-type and waveguide-type. These results indicate that a waveguide-type metasurface further improves the off-axis performance of the doublet lens previously introduced.

Key words メタサーフェス，メタレンズ，入射角度依存性
metasurface, metalens, incident angle dependence

1 Introduction

Metasurfaces are 2D arrays of subwavelength structures known as “meta-atoms.” Metasurfaces have been shown to enable control of the amplitude, phase, polarization, and orbital angular momentum of reflected or transmitted light. One of the important applications of metasurfaces is wavefront control and especially the metasurface that works as a metalens. Many kinds of meta-atoms have been designed for the phase control of metasurfaces using high-index materials. Lalanne and Chavel classified them into three groups [1]: waveguide-type, resonant-type micropost, and resonant-type nanodisk. The waveguide-type has a single mode in the structure. The period is smaller than the structural cutoff [2] and the aspect ratio is relatively high. Microposts are multimode; Kamali *et al*. reported that at least eight resonant modes contribute to the transmittance and the phase in their micropost [3]. The aspect ratio is weakly relaxed compared to the waveguide-type. The doublet metalens that we focus on in this paper is a micropost-type structure. A nanodisk-type can be understood in terms of Mie resonance [4], [5]. A nanodisk-type metalens consists of periodically arranged disk-like structures whose fundamental electric and magnetic resonances coincide at the same wavelength. The aspect ratio is significantly relaxed and good for manufacturing. The three groups classified by Lalanne and Chavel are simple structures such as square pillars or cylindrical pillars that are polarization-independent for normal incident light

† This paper is reprinted with permission from © Optica Publishing Group of reference [21].

due to their symmetry. Most metalenses are designed for a normal incident beam. However, oblique incident light is important for many applications such as imaging. Arbabi *et al*. showed that doublet metalenses are capable of nearly diffraction-limited focusing up to an incidence angle of 30 deg [6]. Their results indicate that the subwavelength elements designed by Arbabi *et al*. are robust to the oblique incidence. However, the paper does not mention much about oblique incidence characteristics.

Although there are previous studies on the characteristics of oblique incidence on dielectric metasurfaces [1], [7], [8], there is no report, to the best of our knowledge, that compares the phase responses of oblique incidence and how those three types affect lens performances. In this paper, we first calculate the incident angle dependence of the three types of meta-atoms classified by Lalanne and Chavel. Our results indicate that the waveguide-type can be most suitable for wide-angle incidence. We then confirm the effect of structural differences on the performance of a doublet lens with full electromagnetic simulations. There are studies on the optimization of the metasurface for further efficiency improvement [9]–[11], but optimized structures are not covered in this paper.

2 Oblique Incidence Characteristics of The Meta-Atoms

We calculate the transmission characteristics of three types of meta-atoms by rigorous coupled-wave analysis (RCWA) [12], [13]. The angle of incidence is calculated from 0 deg to 30 deg. The transmittance and phase are calculated for both TE and TM polarization for oblique incidence because the response of the structure is different depending on the polarization, even when the structure is polarization independent at normal incidence. For each type, the parameters of the metasurface structure, such as height of the pillar and period, are selected from previous papers. The parameters used in the calculation are summarized in Table 1. Fig. 1 illustrates the dependence on the angle of incidence for the three types of subwavelength elements with TM polarization, and Fig. 2 shows the same for TE polarization. Figs. 1 (a) and 1 (d) are the results for the transmittance and the phase of the waveguide-type [2], respectively. Similarly, Figs. 1 (b) and 1 (e) and Figs. 1 (c) and 1 (f) are those of the micropost-type [6] and the nanodisk-type [5]. The

Table 1 Parameters for Oblique Incidence Characteristic Calculations

Meta-atom Type	Waveguide	Micropost	Nanodisk
Lattice type	Square	Hexagonal	Square
Lattice const.	272 nm	450 nm	666 nm
Pillar shape	Square	Cylindrical	Cylindrical
Pillar height	817 nm	600 nm	220 nm
Pillar material	TiO_2	Amorphous silicon	Silicon
Wavelength	633 nm	850 nm	1340 nm
Material between pillars	Air	SU-8	Embedded in medium with n = 1.66
Substrate	SiO_2	SiO_2	
References	[2]	[6]	[5]

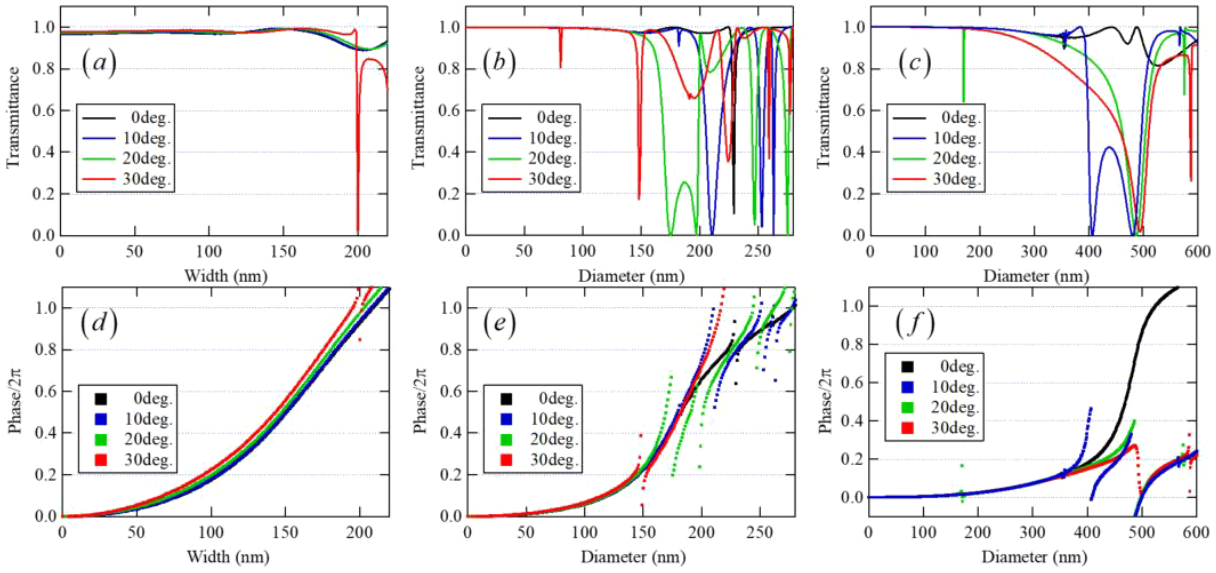

Fig. 1 Incident angle dependence of the transmission coefficient from an infinite 2D array of meta-atoms for TM polarized light: (a)–(c) Transmission coefficients and (d)–(f) phase. (a), (d) Waveguide-type structure [2]. (b), (e) Micropost structure [6]. (c), (f) Nanodisk structure [5].

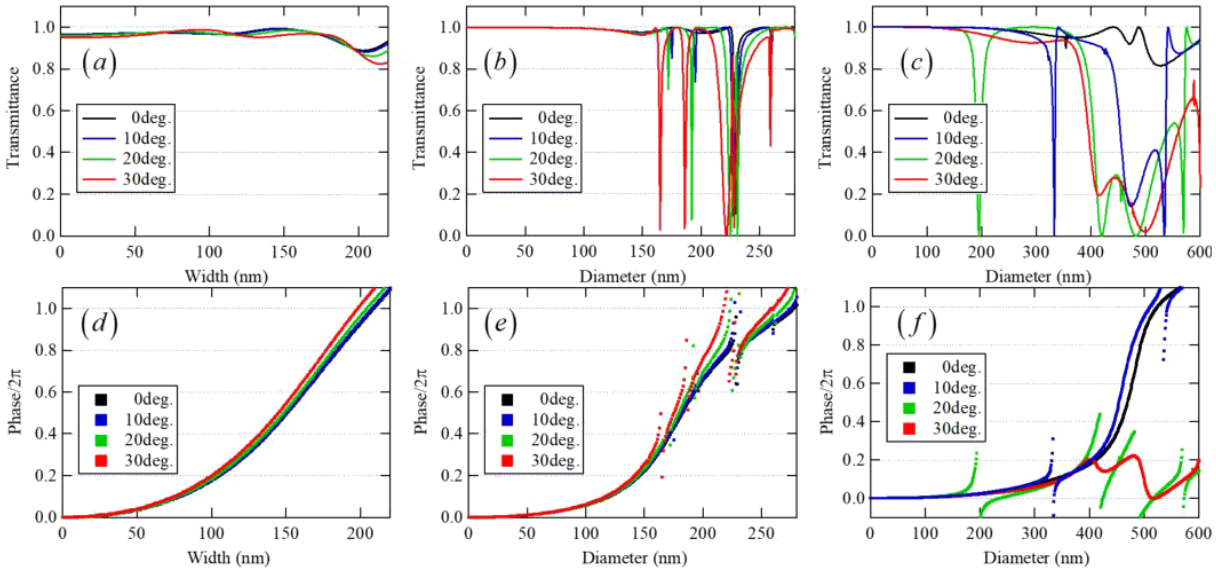

Fig. 2 Incident angle dependence of the transmission coefficient from an infinite 2D array of meta-atoms for TE polarized light: (a)–(c) Transmission coefficients and (d)–(f) phase. (a), (d) Waveguide-type structure [2]. (b), (e) Micropost structure [6]. (c), (f) Nanodisk structure [5].

same applies to Fig. 2 regarding the numbering of subfigures.

The desired features of a meta-atom for lens applications are that the transmittance of the metasurface is close to unity and that the phase covers the range of 2π or more by changing the width of the pillars. Further, it is required that the phase does not change with angle of incidence. In the case of normal incidence, it can be seen in Fig. 1 and Fig. 2 that the phase can be controlled over a range larger than 2π and with high transmittance for all three types. For the micropost-type and the nanodisk-type, however, there are large drops in the transmittance when the incidence angle is 20 deg and 30 deg. These drops are considered to originate from the multiple resonances because multiple resonances can cause destructive interferences. Furthermore, the phases around the drops in transmittance are drastically modulated. Therefore, these will not work well at oblique incidence. In particular, the nanodisk-types cannot cover 2π by changing the diameter at incident angles greater than 10 deg. This is due to the fact that the electrical resonance and magnetic resonance in the nanodisk no longer overlap at oblique incidence, which is clearly seen when the incidence angle is 10 deg in Figs. 1 (c) and 1 (f). Therefore, metalenses made from nanodisks will not have sufficient phase modulation at oblique incidence and good lens performance cannot be expected. On the other hand, the waveguide-type has almost the same transmission phase as normal incidence up to 30 deg. Because the waveguide-type has only a single mode in the structure, the destructive interferences do not happen, even at oblique incidence [7]. These results indicate that the waveguide-type can be superior to the lens performance compared to the other types. Fig. 3 shows examples of the electromagnetic field distributions for the incident angles 0 deg and 20 deg for each type. The electromagnetic field distribution in the waveguide for incident angle 20 deg is almost the same as that of normal incidence because of the single mode; on the other hand, the electric field distributions at 20 deg in the micropost-type and nanodisk-type evidently differ from those at normal incident lights because of multimode.

The doublet metalenses introduced in [6] worked well for oblique incident beams composed of the micropost-type meta-atom. However, from the results of these oblique incident characteristics, it is possible that the performance of the doublet metalenses is further improved by using the waveguide-type instead of the micropost-type.

Since these transmission and phase simulations do not directly indicate what kind of lens performance improvement should expected, we performed lens-focusing simulations to find out.

3 Electromagnetic Simulations for Cylindrical Doublet Metalens

To understand what kinds of lens performance the waveguide-type improves, we simulate focusing with doublet-metalenses composed of micropost-type and waveguide-type meta-atoms by full electromagnetic simulations. The former

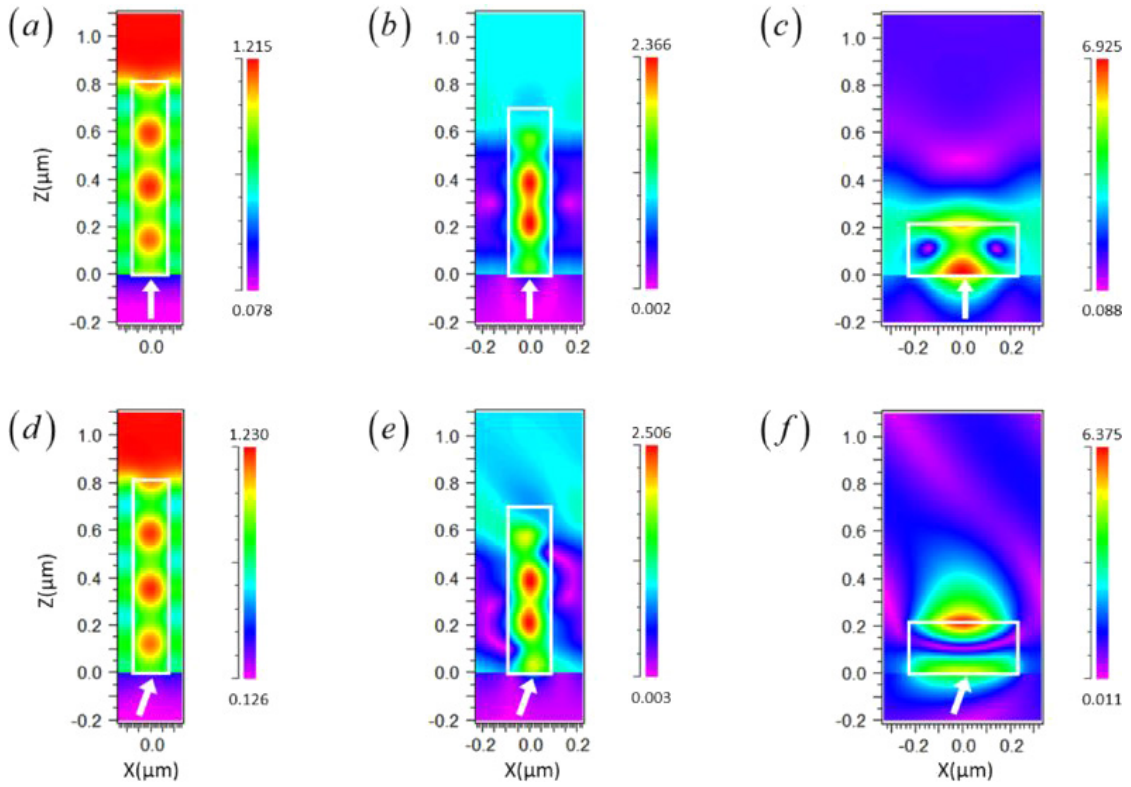

Fig. 3 Examples of the electromagnetic field amplitudes E_y for TE polarized light at Y = 0. (a)–(c) Normal incidence and (d)–(f) incident angle 20 deg. (a), (d) Waveguide-type structure [2] of pillar width 150 nm. (b), (e) Micropost structure [6] of diameter 180 nm. (c), (f) Nanodisk structure [5] of diameter 460 nm. The electronic field component of the incident wave is omitted. Arrows indicate the angle of incidence.

Table 2 Parameters for Oblique Incidence Characteristic Calculations

Meta-atom Type	Waveguide	Micropost
Lattice type	Square	Hexagonal
Lattice const.	280 nm	450 nm
Pillar shape	Cylindrical	Cylindrical
Pillar height	800 nm	600 nm
Material	Amorphous silicon	Amorphous silicon
Wavelength	850 nm	850 nm
Material between pillars	Air	SU-8
Substrate	SiO_2	SiO_2

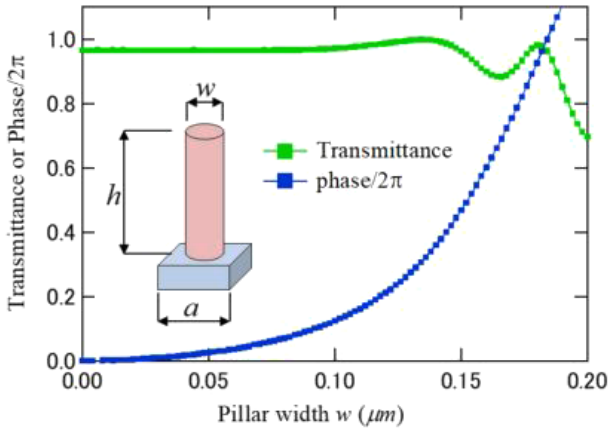

Fig. 4 Transmittance and the phase of the waveguide-type meta-atom we used in the doublet simulations.

is a micropost-type introduced by Arbabi *et al.* [6] and the latter is a waveguide-type that we designed for these cylindrical lens simulations. Table 2 shows the parameters. The diameter used in the cylindrical lens simulations is from 91 nm to 190 nm and the maximum aspect ratio is 8.8. Fig. 4 is the pillar width dependence of the transmittance and the phase for the waveguide-type structure for normal incidence. The inset of the graph in Fig. 4 is a schematic illustration of the unit cell of the meta-atom. The amorphous silicon cylindrical pillars are aligned periodically on a 2D square lattice on the fused silica substrate with a height of h = 800 *nm* and a lattice constant a = 280 *nm*. In our simulations, we use the design of the doublet metalens introduced by Arbabi *et al.*, whose phase profile parameters are shown in Table 1 of the supplementary material in [6]. The cross section is depicted in Fig. 5. The doublet metalens consists of two flat lenses. We refer to the first one as a correcting lens and the second one as a focusing lens. This doublet lens is designed for a single wavelength of 850 nm.

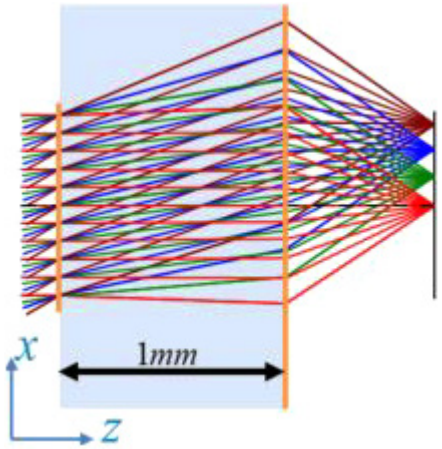

Fig. 5 Doublet metalens introduced by Arbabi *et al*. Phase profile parameters for this doublet metalens are shown in Table 1 in the supplementary material in [6].

There are various electromagnetic simulation methods to study the behavior of electromagnetic fields in structures of the order of wavelength size or below. In particular, the finite-difference time-domain (FDTD) method [14], [15] and the RCWA is widely used. The RCWA is most typically applied to solve scattering from periodic structures. Therefore, we chose RCWA to calculate the transmittance and phase of the periodic element of a metasurface for Figs. 1 and 2. On the other hand, FDTD is more flexible than RCWA, and FDTD can be used for a nonperiodic structure, so we chose FDTD for the doublet metalens simulations below. FDTD grid element sizes are typically from 1/10 to 1/20 of the wavelength to avoid numerical dispersion. However, the grid size to simulate a metalens must be much smaller to represent the change of the pillar diameter of the meta-atom in metasurfaces and a much larger scale simulation is required. As a result, a tremendous amount of time and PC memory will be required to simulate a metalens of a size for practical use. In this paper, we simulate the doublet metalens designed by Arbabi *et al*. [6] (see Fig. 5). The diameter of the lens is ϕ = 1.6 *mm* and the thickness is t = 1 *mm*. If we simulate such a double metalens by simple FDTD with a 5 nm grid element size, the simulation requires 320,000 × 320,000 × 200,000 grid elements. This means that we need much more than petabyte memories to simulate the doublet metalens—and it is unrealistic.

There are several ways to simulate the mm size doublet lens and avoid this difficulty. One approach is to proportionally reduce the simulation size [16]. Lenses under those kinds of simulations are scaled by some scaling factor with parameters such as NA or F/no kept constant. It is reasonable to assume that the focusing features are unchanged because the spot size for ideal focusing depends only on the wavelength and the NA. However, the wavefront aberrations are proportional to the scaling factor and, in this situation, the wavefront aberrations will be underestimated and the balance between the wavefront aberration and the other effects will change. Hence, the lens should be simulated in the same scale as we use in practice, if we want to know the imaging quality in terms of the aberration. Another approach is that the metalens is treated as a phase mask. The response at each position on the metalens is defined by the transmittance and its phase obtained by numerical calculation of individual elements [17]. This method allows us to efficiently simulate many features of the metalenses. However, interactions between subwavelength elements are neglected in this method. In the dielectric meta-surface, a material with a high refractive index is used for the meta-atom so that the electromagnetic field is localized in the meta-atoms and the interactions between neighboring meta-atoms are suppressed to a small level. Therefore, the assumption that the meta-atom can be treated as an independent element might hold to some extent, but the interaction is not zero. In particular, the interaction is likely to be very different at regions where the phase changes rapidly. Byrnes *et al*. proposed another good method that takes advantage of the fact that the phase profile away from the center of the lens can be approximated as a collection of deflector cells [9]. The propagation components from each cell are obtained by RCWA and then the electric fields immediately after transmission through the lens are constructed by the components. This method can calculate a large lens with a good approximation, but the complicated calculations are then required when the incident light is not a simple plane wave, as is the case at the focusing lens of the doublet metalens.

We adopt yet another approach. We simulate a cylindrical lens instead of a rotationally symmetric aspherical lens [18]. Fig. 5 can be considered as the cross section of the corresponding cylindrical lens as well as that of the rotationally symmetric aspherical lens and the wavefront profile on the meridional plane of the spherical lens is identical to the wavefront profile for the cylindrical lens. In a cylindrical lens simulation, we can only know the behavior of the wave on the meridional plane, but the balance between the wavefront aberration and the other effects are the same as in the original lens and we can get useful information from the results. Because the meta-atoms on the cylindrical metalenses are aligned periodically along the cylindrical axis, we can use a periodic boundary condition. And the periodic lat-

tice constants of meta-atoms are smaller than the wavelength. This means that a cylindrical lens configuration can reduce the simulation size smaller than the wavelength along the cylindrical axis. In the case of a doublet metalens, however, the distance between the two metalenses is as large as 1 mm. Hence, even if there is a cylindrical configuration with a periodic boundary condition, the simulation size is still too large to simulate along the optical axis. We must therefore adopt an additional means to reduce the calculation time. One of the ways to reduce the calculation size is subgridding [15]. The space between the two metalens of the doublet is a uniform medium and the grid element size can be larger than needed by metasurface elements. Still, the calculation size with subgridding remains huge. So instead of subgridding, we calculate the propagation from the first metalens surface to the second with Rayleigh–Sommerfeld (RS) diffraction that is usually used for scalar diffraction. The medium between the first metalens and the second one is isotropic, homogeneous, and source free. Each six components of the electromagnetic field obey the RS diffraction formula independently in the medium (see Appendix A). Therefore, an exact full electromagnetic solution can be calculated by the RS diffraction between the two metalens. Then the FDTD calculation is needed only in the vicinity of the two metalenses and the calculation size along optical axes becomes only several micrometers if the wavelength used in the simulations is 850 nm. As described above, by adopting a combination of an RS diffraction calculation and FDTD with a cylindrical lens configuration, it is possible to perform the imaging simulation of the doublet lens in a realistic time. We calculate the fields on the focal plane by following steps:

Step 1: FDTD calculation for the correcting lens.

Input plane wave is excited in the plane just before the correcting lens. The outputs are Ex, Ey, Hx, and Hy in the plane just after the correcting lens.

Step 2: RS diffraction calculation between correcting lens and focusing lens.

Calculate the RS diffraction for each field distribution outputted by FDTD calculation in Step 1. The outputs of these diffraction calculations are the field distributions just before the focusing lens. These calculations can be calculated independently for each field.

Step 3: FDTD calculation for the focusing lens.

Input source is excited in the plane just before the focusing lens using the field distributions calculated by RS diffraction in Step 2. Outputs are Ex, Ey, Hx, and Hy in the plane just after the focusing lens, just like in Step 1.

Step 4: RS diffraction calculation from focusing lens to focal plane.

Calculate the RS diffraction as in Step 2 from the plane just after the focusing lens to the focal plane. The focal spot and the modulation transfer function (MTF) can be calculated from the outputs.

It is important to note that the multiple reflections between the two metalenses do not appear in the results since the back- ward wave is excluded from the calculation of the RS diffraction in Step. 2. However, if there is 10% reflection from a metasurface, noise originated from the multiple reflections will be only about 1% and there will be no significant effect on the simulation results. Multiple reflections will be discussed further at the end of Section 4.

We adopt the FFT–DI method [19] to numerically calculate the RS diffraction formula. The sampling periods and the calculation size on the input plane do not change at the output plane and the output region can be shifted perpendicular to the optical axis by shifting the center of the transfer function kernel $h(x, y)$ in Eq. (A3) of the FFT–DI calculation. In our calculations, since the structures along the cylindrical axis are smaller than the wavelength, propagated wave fields (not evanescent wave fields) are constant along the cylindrical axis. Therefore, we adopt as the transfer function kernel Eq. (A3) instead of Eq. (A2) for the cylindrical doublet metalenses simulations.

4 Results and Discussion

Here, we show the simulation results of the doublet metalenses made of micropost-type and waveguide-type meta-atoms. Simulations are performed with both TM and TE polarization, and the incidence angles are from 0 deg to 30 deg in 10 deg steps. The grid size in the FDTD simulation is $\Delta x = \Delta y = \Delta z = 5\ nm$. Perfectly matched layers (PML) are used in the Z axis direction and the periodic boundary conditions are used in the X axis and Y axis directions.

Fig. 6 and 7 show focal spots on the focal plane at 0 deg, 10 deg, 20 deg, and 30 deg incident angles, and the corresponding MTF. Fig. 6 is for TM polarization and Fig. 7 is for TE polarization. Figs. 6 (a) and 6 (c) shows the focal spots for the micropost-type and waveguide-type, respectively. Figs. 6 (b) and 6 (d) are the MTFs. The same applies to

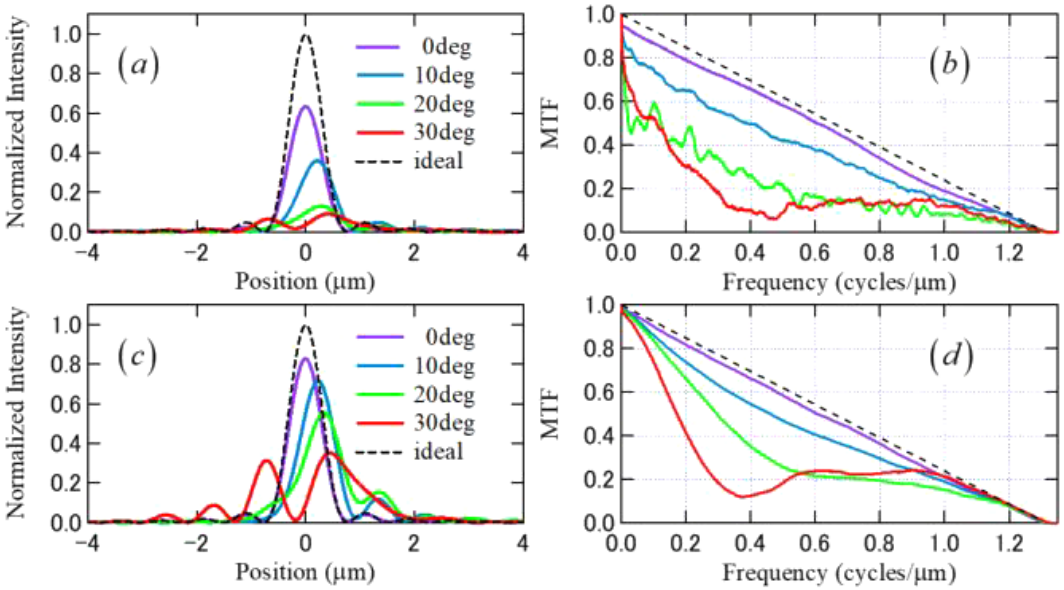

Fig. 6 Focal spots and MTFs for TM polarization: (a) Focal spots of micropost-type, (b) MTF for micropost-type, (c) focal spot of waveguide-type, and (d) MTF for waveguide-type. Dotted line represents ideal focal spot and the corresponding MTF.

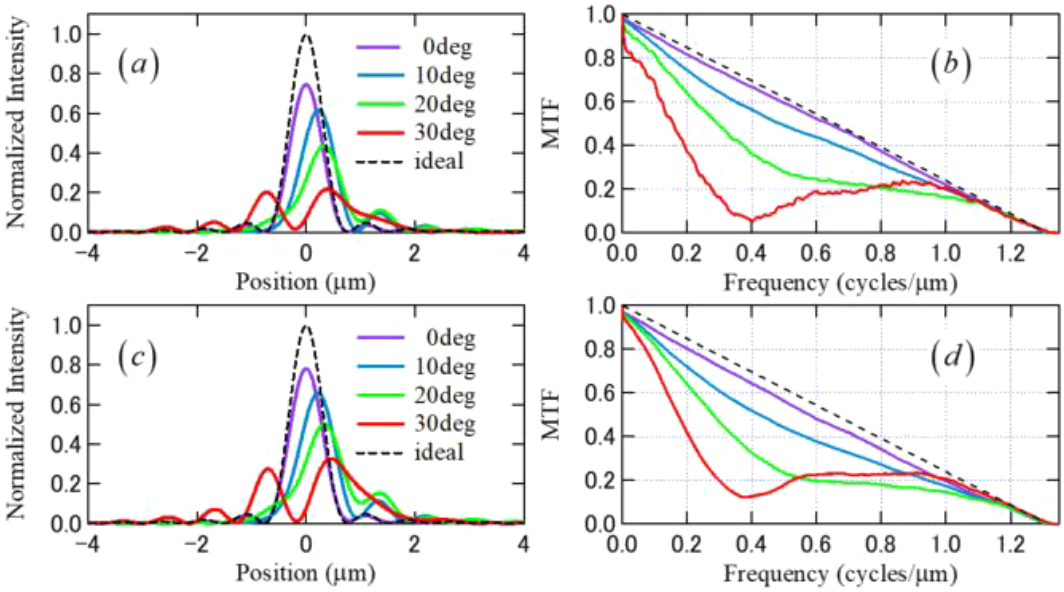

Fig. 7 Focal spots and MTFs for TE polarization: (a) Focal spots of micropost-type, (b) MTF for micropost-type, (c) focal spot of waveguide-type and (d) MTF for waveguide-type. Dotted line represents ideal focal spot and the corresponding MTF.

Fig. 7 regarding the numbering of subfigures. Intensity distributions are calculated by $I = |S_z| = |E_xH_y - E_yH_x|$ and are normalized so that the maximum value of an ideal spot without loss due to scattering or reflection is unity. The chief ray heights calculated by ray tracing are set at the origin of the horizontal axis for oblique incident focal spots.

The difference between the results of the micropost-type and those of the waveguide-type is not large for the TE polarized incident light. Similarly, the difference in results is not large in the case of normal incidence for TM polarization. However, we can see differences in the MTF between the two types at low frequencies below 0.2 cycles/μm for the oblique incidence, especially at 20 deg and 30 deg of TM polarization. Obviously, the waveguide-type is superior to the micropost- type. Moreover, the MTF for incident angles of 20 deg and 30 deg of the micropost-type is very noisy. This is because speckle-like noise is distributed around the spot. Note that the intensities of the speckle are too small to be seen in Fig. 6 (a). We can understand it from the viewpoint that the MTF is defined as the magnitude of the Fourier

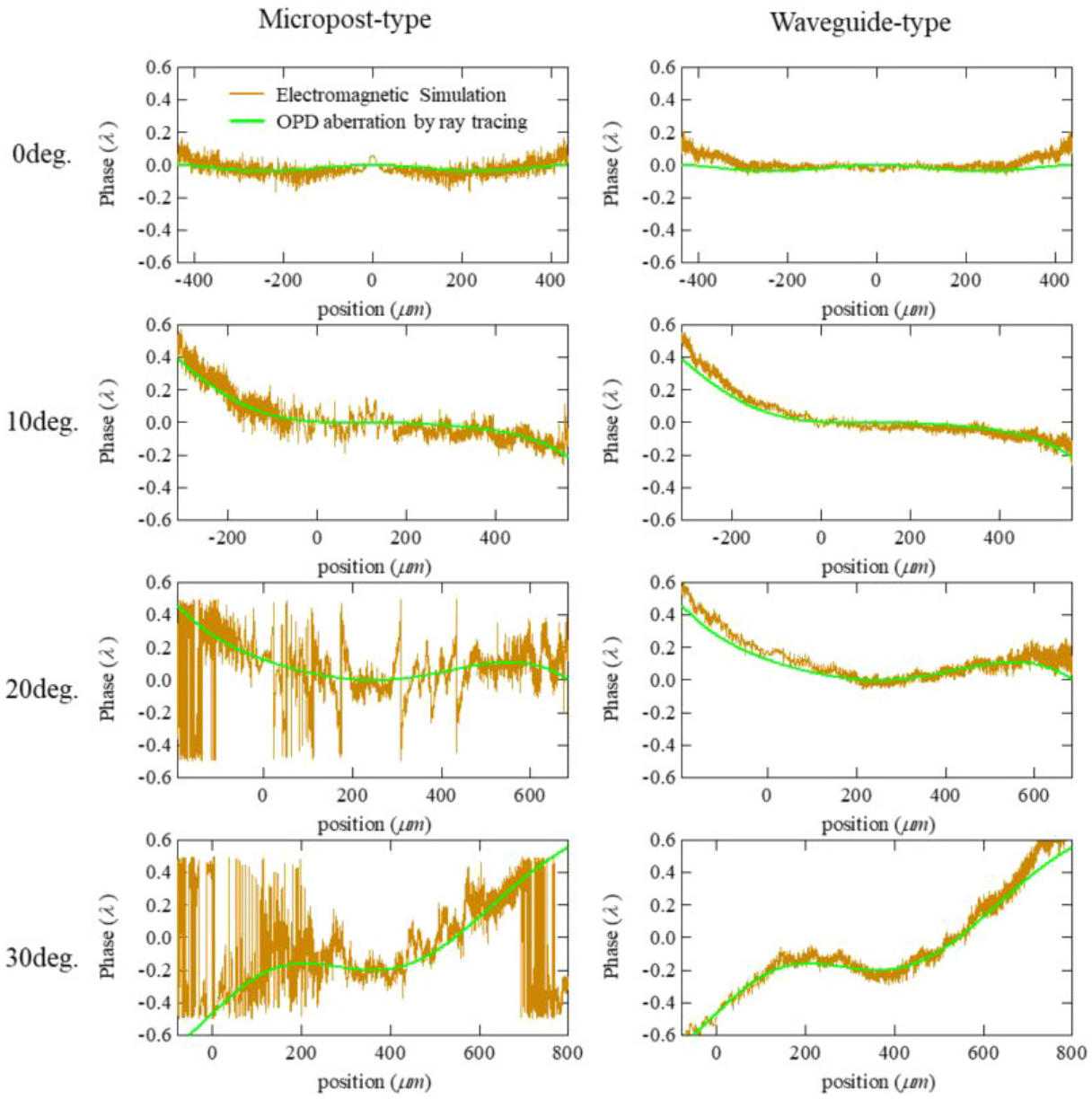

Fig. 8 Wavefront aberrations for each incident angle with TM polarization. Results for the micropost-type are shown in the left column, and those of the waveguide-type are in the right column. Electromagnetic simulations are plotted in light brown, and OPD aberrations are plotted in light green.

transform of the point- spread function. The speckle-like noise appears as flare under incoherent illumination.

Figs. 8 and 9 show the wavefront aberrations of the micropost-type and the waveguide-type. These are our main results. Fig. 8 is for TM polarization and Fig. 9 is for TE polarization. The left column is the micropost-type and the right column is the waveguide-type.

The light brown lines are the wavefront aberrations by electromagnetic field simulations that are the difference from the ideal spherical wavefront on the plane immediately after the focusing metalens. The green lines are the designed wavefront aberration calculated by ray tracing (CODE V, Synopsys, Inc.) as the optical path difference (OPD) aberrations. Metalenses can be defined as phase profiles with even-order polynomials of the radial coordinate in ray tracing calculations. For the waveguide-type, it can be seen that the wavefronts of ray tracing and those of electromagnetic simulations are in good agreement in all cases. For the micropost-type, good agreement is shown when all the cases are of TE polarized light and also in the cases of TM polarized light at small angles of incidence. However, when the incident angle is as large as 20 deg and 30 deg, we can see very large fluctuations in the wavefront and large deviations from the wavefront by ray tracing. In this way, the waveguide-type can suppress the jaggedness of the wavefront aberrations for oblique incident TM polarized light.

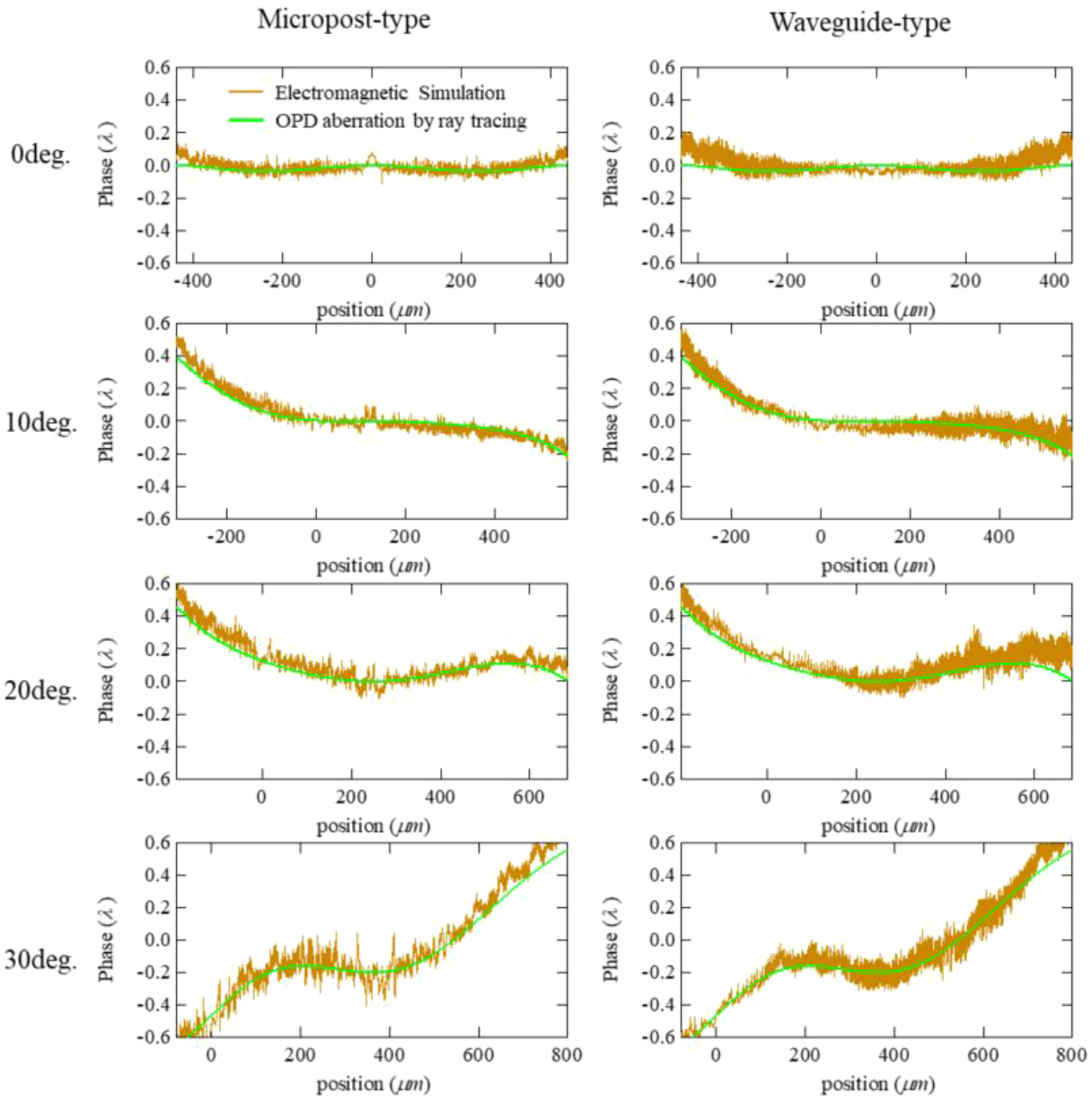

Fig. 9 Wavefront aberrations for each incident angle with TE polarization. Results for the micropost-type are shown in the left column, and those of the waveguide-type are in right column. Electromagnetic simulations are plotted in light brown, and OPD aberrations are plotted in light green.

The main difference between the micropost-type and the waveguide-type is whether it has multimode or single mode, as we can see in Fig. 3. Note that multimode can cause destructive interferences at oblique incidence. They can be seen in the results of the transmittance and transmission phase of the meta-atom itself at oblique incidence, as shown in Figs. 1 and 2, and can result in the jaggedness of the wavefront for the micropost-type metalens.

The difference between the two types can be clearly seen by looking at the wavefront aberration rather than the focal spots or MTF. In addition, the speckle-like noise that appeared at 20 deg and 30 deg of TM polarized light when discussing the MTF can be understood from the disturbance of these wavefronts.

Fig. 10 shows the total power immediately after the correcting lens, the total power immediately after the focusing lens, and the focusing efficiency at the focus position when the power of the incident light on the correcting lens is unity. We define the focusing efficiency as the fraction of the incident light that focused within six times the FWHM spot size.

It can be seen that the focusing efficiencies of the waveguide-type are clearly better than those of the micropost-type. There is not a big difference between the waveguide-type and the micropost-type in terms of wavefront aberration for TE polarization (Fig. 9), but the focusing efficiencies are better than those of the micropost-type. From this result, it

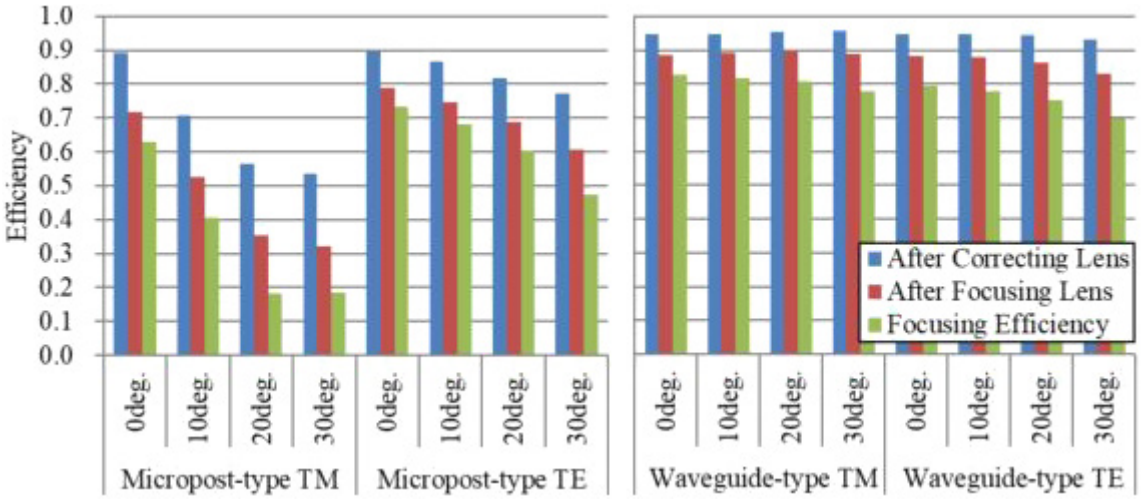

Fig. 10 Efficiency just after the two metasurfaces and focusing efficiencies for: (left) micropost-type doublet metalens and (right) waveguide-type doublet metalens.

is clear that the efficiencies are greatly improved using the waveguide-type metalens compared to the micropost-type metalens when the angle of incidence is large. As we mentioned above, in our simulations the multiple reflections will not have a significant effect if there is 10% reflection from a metasurface. All reflectance from each waveguide metalens are below 10%, except the condition when the incident angle is at 30 deg of TM polarized light whose reflectance for the focusing metalens is 11%; therefore, we can neglect the multiple reflections. As for the micropost-type, however, some reflectance for each metalens are more than 30% and multiple instances of reflected light may appear on the image plane as noise or flare. Therefore, the image quality for a micropost-type metalens can be worse in terms of multiple reflections.

5 Conclusion

It is shown that the wavefront aberrations estimated by full electromagnetic simulations for a waveguide-type metasurface are in good agreement with those found by ray tracing. On the other hand, when the incident angle is large, the wavefront of the micropost-type metalens has large fluctuations. Then, the difference from ray tracing becomes large and those fluctuations cause flare. These results show that the waveguide-type can improve the lens performance of Arbabi's doublet in terms of efficiency, wavefront aberration, and flare.

Because our simulations do not take fabrication errors into account, we cannot mention how tight the tolerance is. The waveguide-type structure is not easy to manufacture, and tight tolerance might be required, which will increase the manufacturing costs. Therefore, a lens with nanodisk-type or micropost-type might be more desirable when using only normal incidence or when the incident angle is not so large. However, from our results, it is better to select the waveguide-type to make a metalens with a large angle of view for a single wavelength, which will have a small aberration and high efficiency. In addition, it is important to check whether the oblique incident characteristics meet the desired lens specifications when designing a sub-wavelength element.

APPENDIX A: Rayleigh–Sommerfeld Diffraction

Let's review the Rayleigh–Sommerfeld (RS) diffraction. When the medium is isotropic, homogeneous, and source free, the time-independent 3D Helmholtz equation for a single frequency is derived from Maxwell's equations:

$$(\nabla^2 + k^2)\mathbf{E}(\mathbf{x}) = 0$$
$$(\nabla^2 + k^2)\mathbf{H}(\mathbf{x}) = 0 \tag{A.1}$$

where **E** and **H** are the electric and magnetic field, and k is wave number. From this formula, we know that each component of the electric or magnetic fields can be expressed independently from the other components. The Rayleigh–Sommerfeld formula of the first kind is

$$U(x,y) = \int U(x',y')h(x-x',y-y')\mathrm{d}x'\mathrm{d}y'$$
$$h(x,y) = \frac{\partial}{\partial z}\left(\frac{\exp(\mathrm{i}k\sqrt{x^2+y^2+z^2})}{\sqrt{x^2+y^2+z^2}}\right) \tag{A.2}$$

where $U(x, y)$ is a complex amplitude of a field. It is an exact solution to the Helmholtz equation from an initial (x', y') plane

to a parallel (x, y) plane with distance z [20]. Therefore, if we know the six components of the electromagnetic field in an initial plane, we can independently calculate each field in the planes parallel to the initial plane using Eq. (A2). If the field distribution does not change along that y axis, as in our simulations, the Rayleigh–Sommerfeld formula in Eq. (A2) is reduced to

$$\begin{aligned} U(x) &= \int U(x')h(x-x')\mathrm{d}x' \\ h(x) &= \frac{kz}{2\mathrm{i}\sqrt{x^2+z^2}} H_1^{(2)}\left(k\sqrt{x^2+z^2}\right) \end{aligned} \tag{A.3}$$

where $H_1^{(2)}$ is a Hankel function of the second kind.

Acknowledgment. The authors wish to thank Dr. Daniel G. Smith of Nikon Research Corporation of America, and Hironobu Makitsubo, Satoshi Yashiki, Hiroyuki Tsukamoto, Daisuke Mori, Hiroshi Konishi, and Seiki Yoshikawa of Nikon Corporation for their great help. Portions of this work were presented in 2021 at META 2021 as "Influence on wide-angle metasurface doublet due to different types of all-dielectric metasurface."

References

[1] P. Lalanne and P. Chavel, "Metalenses at visible wavelengths: past, present, perspectives," *Laser Photon. Rev.* vol. 11, pp. 1600295, 2017.

[2] P. Lalanne, S. Astilean, P. Chavel, E. Cambril, and H. Launois, "Design and fabrication of blazed binary diffractive elements with sampling periods smaller than the structural cutoff," *J. Opt. Soc. Am. A* vol. 16, pp. 1143–1156, 1999.

[3] S. M. Kamali, A. Arbabi, E. Arbabi, Y. Horie, and A. Faraon, "Decoupling optical function and geometrical form using conformal flexible dielectric metasurfaces," *Nat. Commun.* vol. 7, pp. 11618, 2016.

[4] J. Cheng, D. Ansari-Oghol-Beig, and H. Mosallaei, "Wave manipulation with designer dielectric metasurfaces," *Opt. Lett.* vol. 39, pp. 6285–6288, 2014.

[5] M. Decker, I. Staude, M. Falkner, J. Dominguez, D. N. Neshev, I. Brener, T. Pertsch, and Y. S. Kivshar, "High-efficiency dielectric Huygens' surfaces," *Adv. Opt. Mater.* vol. 3, pp. 813–820, 2015.

[6] A. Arbabi, E. Arbabi, S. M. Kamali, Y. Horie, S. Han, and A. Faraon, "Miniature optical planar camera based on a wide-angle metasurface doublet corrected for monochromatic aberrations," *Nat. Commun.* vol. 7, pp. 13682, 2016.

[7] C. Gigli, Q. Li, P. Chavel, G. Leo, M. L. Brongersma, and P. Lalanne, "Fundamental limitations of Huygens' metasurfaces for optical beam shaping," *Laser Photon. Rev.* vol. 15, pp. 2000448, 2021.

[8] D. Arslan, K. E. Chong, D. N. Neshev, T. Pertsch, Y. S. Kivshar, and I. Staude, "Silicon Huygens' metasurfaces at oblique incidence," in *Conference on Lasers and Electro-Optics Europe European Quantum Electronics Conference*, 2017, paper EH_6_2

[9] S. J. Byrnes, A. Lenef, F. Aieta, and F. Capasso, "Designing large, high-efficiency, high-numerical-aperture, transmissive meta-lenses for visible light," *Opt. Express* vol. 24, pp. 5110–5124, 2016.

[10] J. Yang and J. A. Fan, "Topology-optimized metasurfaces: impact of initial geometric layout," *Opt. Lett.* vol. 42, pp. 3161–3164, 2017.

[11] D. Sell, J. Yang, S. Doshay, R. Yang, and J. A. Fan, "Large-angle, multifunctional metagratings based on freeform multimode geometries," *Nano Lett.* vol. 17, pp. 3752–3757, 2017.

[12] M. G. Moharam and T. K. Gaylord, "Rigorous coupled-wave analysis of metallic surface-relief gratings," *J. Opt. Soc. Am. A* vol. 3, pp. 1780–1787, 1986.

[13] L. Li, "New formulation of the Fourier modal method for crossed surface-relief gratings," *J. Opt. Soc. Am. A* vol. 14, pp. 2758–2767, 1997.

[14] K. Yee, "Numerical solution of initial boundary value problems involving Maxwell's equations in isotropic media," *IEEE Trans. Antennas Propag.* vol. 14, pp. 302–307, 1966.

[15] A. Taflove and S. C. Hagness, *Computational Electrodynamics: The Finite-difference Time-domain Method*, 3rd ed. Norwood: Artech House, 2005.

[16] A. Arbabi, Y. Horie, A. J. Ball, M. Bagheri, and A. Faraon, "Subwavelength-thick lenses with high numerical apertures and large efficiency based on high-contrast transmitarrays," *Nat. Commun.* vol. 6, pp. 7069, 2015.

[17] C. Xu, M. Novak, D. Herrmann, L.-C. Hu, E. Heller, and M. Bahl, "Effective approach for design and simulation of metalens structures," in *META* 2019 *Lisbon—Portugal The* 10*th International Conference on Metamaterials, Photonic Crystals and Plasmonics*, 2019, pp. 1828.

[18] F. Aieta, M. A. Kats, P. Genevet, and F. Capasso, "Multi-wavelength achromatic metasurfaces by dispersive phase compensation," *Science* vol. 347, pp. 1342–1345, 2015.

[19] F. Shen and A. Wang, "Fast-Fourier-transform based numerical integration method for the Rayleigh–Sommerfeld diffraction formula," *Appl. Opt.* vol. 45, pp. 1102–1110, 2006.

[20] L. Mandel and E. Wolf, *Optical Coherence and Quantum Optics*, Cambridge: Cambridge University, 1995.

[21] H. Toba, H. Takagi, M. Ohashi, K. Otaki, and Y. Takigawa, "Influence on wide-angle doublet metalenses due to different types of all-dielectric metasurfaces," *Appl. Opt.* vo. 61, pp. 597–606, 2022.

鳥羽英光　Hidemitsu TOBA
光学本部 要素開発部
Fundamental Technology Development Department
Optical Engineering Division

髙木英嗣　Hidetsugu TAKAGI
光学本部 第一設計部
1st Designing Department
Optical Engineering Division

大橋道雄　Michio OHASHI
光学本部 第二設計部
2nd Designing Department
Optical Engineering Division

大滝　桂　Katsura OTAKI
光学本部 要素開発部
Fundamental Technology Development Department
Optical Engineering Division

瀧川雄一　Yuichi TAKIGAWA
光学本部 要素開発部
Fundamental Technology Development Department
Optical Engineering Division

スポーツフィールドにおける自己校正を使った観客の注視領域推定†

阿部和広，高山侑也，大坪洋介，小池哲也

Estimating Attention Area of Spectator using Self-calibration in Sports Fields

Kazuhiro ABE, Yuuya TAKAYAMA, Yosuke OTSUBO and Tetsuya KOIKE

スポーツ映像ソリューションにおいて，観戦者の注視領域を推定することは重要なシーンを抽出する上で有用である．注視領域は観客の視線の先のコート上の領域として特定される．スポーツフィールドの周囲に配置された観客を撮影するカメラを使って注視領域推定をするためには，視線ベクトルをカメラ座標系からコート座標系に変換するためにカメラ校正が必要である．一方で，観客をズームアップで写す観客カメラは校正ターゲットとなるコートなどのマーカーが映っていないため校正が難しい．そこで，本研究では，観客を撮影するカメラと俯瞰撮影するカメラの組み合わせから自己校正して注視領域を推定する手法を提案する．さらに，観客カメラ画像は低解像度であり一人ひとりの正確な視線推定は難しいため，複数の頭部方向を合計することにより最終的な注視領域を算出した．実際に行われた3×3バスケットボールでの撮影映像での検証により，リーズナブルな注視領域推定結果が得られることを示す．

In sports video solutions, estimating the attention area of spectators is useful for extracting important scenes. The attention area is identified as the area on the court corresponding to the gaze direction based on the spectator's gaze. To do this from cameras installed around the sports field that capture the spectators, camera calibration is required to convert the coordinate system of the camera that shoots the spectators and the coordinate system of the court. However, it is difficult to apply the general camera calibration to the camera capturing spectators because the court is not reflected in the camera. Therefore, in this study, we propose a method to estimate the attention area by self-calibrating the combination of the camera capturing the spectators and the camera capturing the overhead view. Since it is difficult to estimate the gaze accurately from low-resolution images of spectators, we approximate the gaze direction as the head direction and reduce the error by aggregating multiple head directions. Verification using the shooting data of an actual 3 x 3 basketball game shows that a reasonable attention area map can be obtained based on three camera inputs.

Key words コンピュータービジョン，スポーツ映像分析，視線推定
computer vision, sports video analysis, gaze estimation

1 はじめに

近年，スポーツ映像ソリューションにおいて，機械学習や画像認識の応用が進んでいる．特に，スポーツ映像撮影の自動化において有用であり，製品化も進んでいる［10］．バスケットボールやサッカーなどの球技スポーツの映像撮影を自動化する試みにおいて，「スポーツフィールド（コート）上のどの領域を撮影するか？」は大きな課題である．このために，まずボールの位置や選手の位置に基づいて撮影領域を決定することが考えられる．しかし，ボールは動きも速く，大きさやオクルージョンの点で検知が非常に難しく，また，選手の位置検知・動作認識もそれ自体が難しいため，そこから撮影領域を決定するには課題が多い．そこで，観客の注視領域に基づいて撮影領域を決定するアプローチを考える．これは，映像を見る人が「どこが見たいか？」を直接認識するアプローチであり，フィールド上の選手やボールに依存しない解析であることから，特定のスポーツに特化しない汎用的な方法になり得る．また，観客の注視領域推定は，観客の嗜好性を反映していると考えられ，ハイライトシーン生成［11］，カメラコントロール［12］，仮想カメラシステム［13］などへの応用や，エンターテイメント（音楽ライブ，舞台演劇）などのスポーツ以外の幅広い適用シーンがある．さらに，注視領域は対象に関する注意や関心の度合いと密接に関係していることか

† 本稿は，著者の引用文献［19］の人工知能学会より許諾を得ている．

ら，注視領域推定それ自体が広告の効果測定［14］，教育の集中度合い計測や視線操作［15］などにも応用できる．このような背景から，本研究では観客の注視領域推定の方法を提案する．

注視領域の推定は，観客の視線方向を推定し，観客の視点から視線方向に投影したコート上の領域を推定することで達成できる．そのために，まずは，観客の視線推定について考える．スポーツを観戦している観客は複数人が集合しており，多くの観客が 1 画角に捉えられているため，一人ひとりの顔が低解像度で撮影されている状況で視線推定できることが望ましい．従来の視線推定は，ターゲットに装着する専用のデバイスを必要とし，スポーツを観戦する観客に装着させるのは大きな負担となり現実的ではない．他方，近年，画像から視線推定を行う手法も研究されている［16］が，高解像度の顔画像で瞳領域を必要とするため，本研究で対象とする観客画像には適していない．そこで本研究では，低解像度顔画像からでも推定が可能な頭部方向推定を用いることで，視線方向を頭部方向と近似することとした．一方で，観客一人ひとりの頭部方向は，観客の集中度合いなどによってばらつくため，複数人の観客の合計をとることで頑健な注視領域推定を実現した．

次に，視線方向のフィールド上への投影について考える．観客を撮影するカメラ（＝観客カメラ）から推定した視線方向は観客カメラの座標系で推定されたものであるため，コート上に投影して注視領域を得るためには，視線ベクトルをコート座標系に変換する必要がある．この変換は，観客カメラのカメラ校正で実現できる．カメラ校正なしで注視領域を直接学習する手法も提案されている［17］が，全員が同じ対象を注視しているという限定的な仮定に基づいており，カメラ校正による手法の重要性は依然として高い．コートを俯瞰する画角を持つカメラ（＝俯瞰撮影カメラ）を用いる場合は，コートを参照物体とし，画像内のコートと参照コートとの対応からホモグラフィーを推定し，カメラ校正を行うことができる．一方，観客カメラではコートが映っていないため，この手法を使うことができない．そこで，コート外の物体の対応を用いて，観客カメラと俯瞰撮影カメラとの自己校正を行った．

以上から，本研究では，スポーツフィールドにおいて，1 台の観客カメラと 2 台の俯瞰撮影カメラの組み合わせから自己校正を行い，複数観客の注視領域の合計をとることによって，スポーツフィールド上の注視領域を推定する手法を提案する．そして，実際の 3 × 3 バスケットボール試合の撮影データを用いた検証によって，3 台のカメラ入力をもとに合理的な時空間の注視領域マップを得ることができることを示した．

2 手　法

本研究で提案する注視領域推定は，カメラ校正，視線推定，視線投影からなる．本手法では，観客をズームで撮影する「観客カメラ」1 台と，コート全体を撮影する「俯瞰カメラ」2 台を用いる．この構成を，Fig. 1 に示す．また，全体のアルゴリズムフローを Fig. 2 に示す．

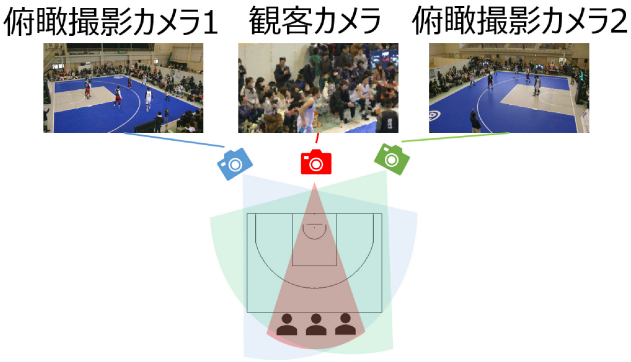

Fig. 1　カメラの構成

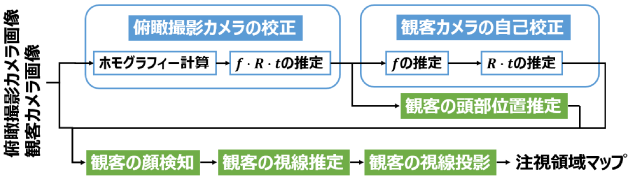

Fig. 2　注視領域推定のアルゴリズムフロー

2.1. カメラ校正

カメラ校正では，コート座標系における，内部パラメーターである校正行列 K と外部パラメーターである回転 R，位置 $\boldsymbol{t}$ を推定する．ここで，アスペクト比を 1，スキュー歪を 0，レンズ歪みが無く，principal point を画像中心（x_0, y_0）と仮定すると，内部パラメーターのうち推定すべきパラメーターは焦点距離 f のみとなり，校正行列 K は

$$K = \begin{bmatrix} f & 0 & x_0 \\ 0 & f & y_0 \\ 0 & 0 & 1 \end{bmatrix} \tag{1}$$

となる．

2.1.1. 俯瞰カメラの校正

俯瞰カメラは，コートが映っているため，4 点の対応から参照コートとのホモグラフィー H が計算できる．このとき，ホモグラフィー $H = [\boldsymbol{h}_1 \quad \boldsymbol{h}_2 \quad \boldsymbol{h}_3]$，校正行列 K，回転 $R = [\boldsymbol{r}_1 \quad \boldsymbol{r}_2 \quad \boldsymbol{r}_3]$ と位置 $\boldsymbol{t}$ の関係は，

$$\begin{bmatrix} \boldsymbol{h}_1 & \boldsymbol{h}_2 & \boldsymbol{h}_3 \end{bmatrix} = \lambda \boldsymbol{K} \begin{bmatrix} \boldsymbol{r}_1 & \boldsymbol{r}_2 & \boldsymbol{t} \end{bmatrix} \tag{2}$$

である［1］．また，r_1, r_2が正規直交であることから，

$$\boldsymbol{h}_1^{\top} \boldsymbol{K}^{-\top} \boldsymbol{K}^{-1} \boldsymbol{h}_2 = \boldsymbol{0} \tag{3}$$

$$\boldsymbol{h}_1^{\top}\boldsymbol{K}^{-\top}\boldsymbol{K}^{-1}\boldsymbol{h}_1=\lambda^2 \tag{4}$$

$$\boldsymbol{h}_2^{\top}\boldsymbol{K}^{-\top}\boldsymbol{K}^{-1}\boldsymbol{h}_2=\lambda^2 \tag{5}$$

が導かれる．式（2）より，焦点距離 f は，

$$f=\sqrt{-\frac{(h_{11}-x_0h_{13})(h_{21}-x_0h_{23})+(h_{12}-y_0h_{13})(h_{22}-y_0h_{23})}{h_{23}h_{13}}} \tag{6}$$

と求めることができる．ここで，$[h_{11}\quad h_{12}\quad h_{13}]^{\top}=\boldsymbol{h}_1$，$[h_{21}\quad h_{22}\quad h_{23}]^{\top}=\boldsymbol{h}_2$，である．回転 $R=[\boldsymbol{r}_1\quad \boldsymbol{r}_2\quad \boldsymbol{r}_3]$ と位置 $\boldsymbol{t}$ は，式（2）−（5）より，

$$\boldsymbol{r}_1=\lambda^{-1}\boldsymbol{K}^{-1}\boldsymbol{h}_1 \tag{7}$$

$$\boldsymbol{r}_2=\lambda^{-1}\boldsymbol{K}^{-1}\boldsymbol{h}_2 \tag{8}$$

$$\boldsymbol{r}_3=\boldsymbol{r}_1\times\boldsymbol{r}_2 \tag{9}$$

$$\boldsymbol{t}=\lambda^{-1}\boldsymbol{K}^{-1}\boldsymbol{h}_3 \tag{10}$$

$$\lambda=\left\|K^{-1}\boldsymbol{h}_1\right\|=\left\|K^{-1}\boldsymbol{h}_2\right\| \tag{11}$$

と求めることができる．

2.1.2. 観客カメラの自己校正

観客カメラは，コートが映っていないため，参照コートとの対応点を特定できず，直接校正することができない．そこで，観客カメラと一部画角がオーバーラップしている校正済み俯瞰撮影カメラを使い，俯瞰撮影カメラ画像と観客カメラ画像との対応点から，自己校正する．まず，5点以上の対応点から，5点法［2］により，Essential matrix を求める．次に，特異値分解により R と $\boldsymbol{t}$ を復元する．このとき，可能な解が4通りあるが，chirality constraint によって1通りに決定する［2］．ここで，$\boldsymbol{t}$ はスケール倍の不定性がある．

焦点距離 f は，撮影時の機材情報から得ることもできるが，映像編集過程でのメタデータの消失，撮影中の調整による変更，などの理由から必ずしも利用できない．そこで，本研究では，画像情報から校正する手法を4通り試した．画像対応点のみから自己校正する手法として，2カメラ（俯瞰撮影カメラ1，2のどちらかと観客カメラ）を用いる①Fundamental matrix から求める手法と，3カメラ（俯瞰撮影カメラ1，2と観客カメラ）を用い②角度を用いる手法を試した．一方で，これらの方法は実用的なシナリオでは適用が難しいことが知られているため，③シーンの知識を利用する方法と④頭部の大きさを使ったヒューリスティックによる手法を試した．

①Fundamental matrix から求める方法

8点以上の対応点から8点法により Fundamental matrix を求め，それを使って f を求める方法である．本研究では，Bougnoux の手法［9］と Hartley の手法［3］を試した．

Bougnoux の手法によれば，俯瞰撮影カメラの焦点距離を f' として，観客カメラの焦点距離 f は

$$f=\sqrt{-\frac{\boldsymbol{p}'^{\top}[\boldsymbol{e}']_{\times}\tilde{\boldsymbol{I}}\boldsymbol{F}\boldsymbol{p}\boldsymbol{p}^{\top}\boldsymbol{F}^{\top}\boldsymbol{p}'}{\boldsymbol{p}'^{\top}[\boldsymbol{e}']_{\times}\tilde{\boldsymbol{I}}\boldsymbol{F}\tilde{\boldsymbol{I}}\boldsymbol{F}^{\top}\boldsymbol{p}'}} \tag{12}$$

と求められる．ここで，$\boldsymbol{p},\boldsymbol{p}'$ はそれぞれ観客カメラ，俯瞰撮影カメラの principal point，$\boldsymbol{e}'$ は俯瞰撮影カメラのエピポール，$\tilde{\boldsymbol{I}}=\mathrm{diag}(1,1,0)$ である．Hartley の手法は，Kruppa 方程式を解くことにより f を決定する．ただし，これらの方法は実用的なシナリオでは適用が難しいことは注意が必要である［4］．

②角度を利用する方法

コート座標における2点 $\boldsymbol{X}_1,\boldsymbol{X}_2$ が観客カメラに投影される点が $\boldsymbol{x}_1,\boldsymbol{x}_2$ とすると，$\boldsymbol{x}_1,\boldsymbol{x}_2$ を逆投影したときに作る線がなす角度 α は，カメラ幾何から，

$$\cos\alpha=\frac{\boldsymbol{x}_1^{\top}\boldsymbol{\omega}^{*}\boldsymbol{x}_2}{\sqrt{\boldsymbol{x}_1^{\top}\boldsymbol{\omega}^{*}\boldsymbol{x}_1}\sqrt{\boldsymbol{x}_2^{\top}\boldsymbol{\omega}^{*}\boldsymbol{x}_2}} \tag{13}$$

と導ける［4］．これを f について解くことにより f を求めることができ，α は，観客カメラのカメラ中心 $\boldsymbol{C}$ と，$\boldsymbol{X}_1,\boldsymbol{X}_2$ から求めることができる．コート座標における $\boldsymbol{C}$ は，エピポールがカメラ中心の像であることを利用して，俯瞰撮影カメラ1に対する観客カメラのエピポール $\boldsymbol{e}_1$ と俯瞰撮影カメラ2に対する観客カメラのエピポール $\boldsymbol{e}_2$ の三角測量により求めた．2点 $\boldsymbol{X}_1,\boldsymbol{X}_2$ は，俯瞰撮影カメラ1，2から三角測量によって求めた任意の点のコート座標を利用することができるが，本研究では，俯瞰撮影カメラ1画像の最も右側と左側の2人の観客の頭部位置を利用した．

③シーンの知識を利用する方法

シーンについての事前知識がある場合，その知識を制約として校正に利用できる．本研究では，観客席がコートと同一平面上にあることを利用して，観客カメラ−俯瞰カメラのホモグラフィー $H_{spec\text{-}over}$ を求め，2.1.1.で得られた俯瞰カメラ−コートのホモグラフィー $H_{over\text{-}court}$ より，観客カメラ−コートのホモグラフィー $H_{spec\text{-}court}=H_{spec\text{-}over}\cdot H_{over\text{-}court}$ を求め，2.1.1.と同様にホモグラフィーから焦点距離を得る．

④頭部の大きさを使ったヒューリスティックによる方法

カメラからの距離が s である大きさ y_o の被写体をカメラで撮影したとき，撮影した像の大きさ y_i は，$s\gg f$ とすると，

$$y_i=y_o\cdot f/(s-f)\approx y_0\cdot f/s \tag{14}$$

と表せる．被写体を観客の頭部として y_o を頭部の大きさとし，同じ観客頭部を観客カメラと俯瞰撮影カメラから撮影したときの観客頭部の大きさをそれぞれ y_i, y_i'，距離を s, s'，俯瞰撮影カメラの焦点距離を f' とすれば，

$$y_i/y_i'=fs'/f's \tag{15}$$

となる．ヒューリスティックに，$s = s'$ とすれば，$f = y_i f'/y_i'$ と求めることができる．

2.2. 視線推定

観客カメラの画像では視線推定が困難であるため，頭部方向を視線方向と近似することとした．頭部方向推定は，顔検知によって得られた顔画像に対して行った．顔検知データセット［5］で訓練済みの顔検知モデル［6］を用い，画像内の観客の顔領域を検知した．検知した顔画像に対し，facial landmark データセット［7］で訓練済みの頭部方向推定モデル［8］を用いて 3 次元頭部方向 $\boldsymbol{h}$ を出力した．

2.3. 視線投影

コート座標系における観客の視線方向 $\boldsymbol{g}$ は，コート座標系での観客カメラの回転 R，観客カメラから推定した観客の視線方向を $\boldsymbol{h}$，z 軸方向の単位ベクトルを $\boldsymbol{u}$ とすると，幾何的な関係から，

$$\boldsymbol{g} = R^{-1} \cdot \mathrm{Rot}(\boldsymbol{h}) \cdot \boldsymbol{u} \tag{16}$$

と書ける．ただし，Rot($\boldsymbol{h}$) は，$\boldsymbol{h}$ と $\boldsymbol{u}$ とのなす角の yaw, pitch, roll 角をそれぞれ θ_y, θ_p, θ_r としたときの回転行列

$$\mathrm{Rot}(\boldsymbol{h}) = \begin{bmatrix} 1 & 0 & 0 \\ 0 & \cos\theta_p & -\sin\theta_p \\ 0 & \sin\theta_p & \cos\theta_p \end{bmatrix} \begin{bmatrix} \cos\theta_y & 0 & \sin\theta_y \\ 0 & 1 & 0 \\ -\sin\theta_y & 0 & \cos\theta_y \end{bmatrix} \begin{bmatrix} \cos\theta_r & -\sin\theta_r & 0 \\ \sin\theta_r & \cos\theta_r & 0 \\ 0 & 0 & 1 \end{bmatrix} \tag{17}$$

である．

注視領域は，観客の視点（＝頭部位置）から視線方向へコート上に投影した領域である．視線投影は，コート座標系の z 方向は考慮せず，視線方向 $\boldsymbol{g}$ を x-y 平面上に投影した 2 次元視線方向 $\bar{\boldsymbol{g}}$ を用いた．人間の視野は点ではなく一定の大きさを持つため，注視領域を視線上にピークを持ち角度方向に広がりがある分布を持っていると仮定するのが自然であろう．具体的には，角度方向の分布を Gauss 分布と仮定し，コート上の点 $\boldsymbol{q}$ での注視領域スコア a($\boldsymbol{q}$) を，

$$a(\boldsymbol{q}) = exp\left(-\frac{\theta^2}{2\sigma^2}\right) \tag{18}$$

とした．ここで，θ は，観客の頭部位置を $\boldsymbol{p}$ としたときの，ベクトル $\bar{\boldsymbol{g}}$ とベクトル $\boldsymbol{q}-\boldsymbol{p}$ とのなす角である．σ は広がりの度合いを表すパラメーターであり，実験的に $\sigma = 0.2$ rad（11.46°）と設定した．観客の頭部位置 $\boldsymbol{p}$ は，観客を撮影する異なる 2 台の俯瞰カメラから検知した顔位置から，三角測量によって推定した．

最後に，複数の観客の注視領域スコアを算出し，それらを合計し，最終的な注視領域スコアとした．

3 実　験

3.1. データセットと精度評価

本実験では，茨城県つくば市に本拠地を置く 3 × 3 バスケットボールチーム「アルボラーダ」主催の 3 × 3 バスケットボールのリーグにおいて，自然に観客を入れた状態で，コート周辺に設置した俯瞰撮影カメラ 2 台，観客カメラ 1 台から撮影した 1 試合分の映像［18］を用いて検証を行った．対象とする観客は，対象とする試合時間内に離席せず終始観戦している観客を 7 人抽出した．対象とする観客のみを抽出するために，対象の観客の顔検知の結果に対してトラッキングを行い，トラッキングがロストした場合は手動で補正を行った．

定量的な精度評価は，ボールを保持しているプレイヤーに注目が集まりやすいことから，注視領域にボールを保持しているプレイヤーが含まれるかどうかを基準として評価した．具体的には，試合全体からランダムにフレームを100フレームサンプリングし，ボールを保持しているプレイヤーの足のコート座標における位置を目視でアノテーションを行った．そして，コート内の領域のうち，注視領域スコア上位50％の領域を抽出し，その領域にアノテーション済みのボール保持プレイヤー座標が含まれるフレームを正解と評価した．なお，試合の展開が停止したフレームおよびパスやシュート動作後にボールが空中に存在しているフレームは評価する100フレームに含めないこととした．

3.2. 結果

焦点距離の推定について，各方法で算出した結果を Table 1に示す．手法①については，実数解を得ることができなかった．

各焦点距離推定手法による注視領域スコアのマップの例を Fig. 3 に示す．また，各焦点距離推定手法における，ボール保持プレイヤーが含まれるかどうかの精度評価結果を Table 2 に示す．なお，比較のため，ランダムに領域を抽出した場合の期待値も Table 2 に示す．

Table 1　各手法で算出した焦点距離（①-1：FundMat（Bougnoux），①-2：FundMat（Hartley): Fundamental matrix から求める方法（それぞれ Bougnoux，Hartley の方法），②Angle：角度を利用する方法，③Scene：シーンの知識を利用する方法，④Heuristic：頭部の大きさを使ったヒューリスティックによる方法）

手法	焦点距離（pixel）
①-1 FundMat（Bougnoux）	NaN
①-2 FundMat（Hartley）	NaN
② Angle	8668.86
③ Scene	15494.6
④ Heuristic	18761.4

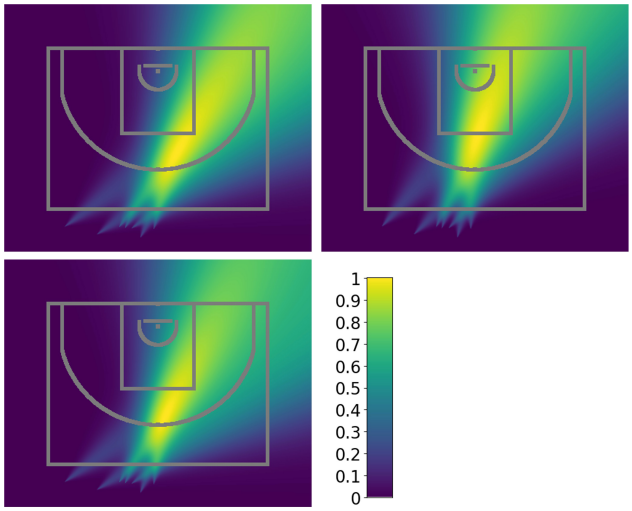

Fig. 3　各手法における注視領域スコアのマップ（左上が② Angle，右上が③ Scene，左下が④ Heuristic）．コートラインをオーバーレイ表示している．

Table 2　各焦点距離推定手法による精度評価結果

手法	精度
② Angle	73%
③ Scene	90%
④ Heuristic	78%
ランダム	50%

どの手法においても，ランダムな領域抽出による精度を上回っていることから，ボール保持プレイヤーを含む領域を有意に抽出できていることが分かる．ゲームフィールドにおいて，注目が集まるのはボールを保持しているプレイヤーの周辺領域であることから，この結果は，本研究で提案する手法によって，注目が集まるフィールド領域を抽出できていることを示す．また，③ Scene の手法の精度が高いことは，焦点距離の推定精度も高いことを示唆している．

4　まとめ

スポーツフィールドにおける観客の注視領域を，１台の観客カメラと２台の俯瞰撮影カメラの組み合わせから自己校正を行い，観客全体の注視領域を推定する手法を提案した．そして，実際の３×３バスケットボール試合の撮影データを用いた検証によって，３台のカメラ入力をもとに合理的なコート上の注視領域マップを得ることができることを示した．ボール保持プレイヤーを含む領域を有意に抽出できていることから，推定された注視領域を撮影領域の決定に用いることが期待できる．

今後の展開としては，コートの z 軸方向も考慮した注視領域の推定，自己校正に利用する対応点の自動検出，撮影領域への応用，スポーツ以外の領域への展開が考えられる．

謝　辞

注視領域に関して，技術的な助言を頂いた株式会社コンピュータマインドの青木渓氏，菅野柊紀氏，山崎貴史氏に感謝を申し上げます．

引　用　文　献

[1] Z. Zhang, “A Flexible New Technique for Camera Calibration,” *IEEE Transactions on Pattern Analysis and Machine Intelligence*, vol. 22, no. 11, pp. 1330–1334, 2000.

[2] D. Nistér, “An efficient solution to the five-point relative pose problem,” *IEEE Transactions on Pattern Analysis and Machine Intelligence*, vol. 26, no. 6, pp. 756–770, 2004.

[3] R. Hartley, “Kruppa’s equations derived from the fundamental matrix,” *IEEE Transaction on Pattern Analysis and Machine Intelligence*, vol. 19, no. 2, pp. 133–135, 1997.

[4] R. Hartley and A. Zisserman, *Multiple View Geometry in Computer Vision*, 2nd ed. Cambridge University Press, 2004.

[5] S. Yang, P. Luo, C. C. Loy, and X. Tang, “Wider face: A face detection benchmark,” in *Proceedings of the IEEE Conference on Computer Vision and Pattern Recognition*, pp. 5525–5533, 2016.

[6] S. Zhang, X. Zhu, Z. Lei, H. Shi, X. Wang, and S. Z. Li, “S3fd: Single shot scale-invariant face detector,” in *Proceedings of the IEEE International Conference on Computer Vision*, pp. 192–201, 2017.

[7] X. Zhu, Z. Lei, X. Liu, H. Shi, and S. Z. Li, “Face alignment across large poses: A 3d solution,” in *Proceedings of the IEEE Conference on Computer Vision and Pattern Recognition*, pp. 146–155, 2016.

[8] N. Ruiz, E. Chong, and J. M. Rehg, “Fine-grained head pose estimation without keypoints,” in *Proceedings of the The IEEE International Conference on Computer Vision and Pattern Recognition Workshops*, pp. 2155–215509, 2018.

[9] S. Bougnoux, “From Projective to Euclidean Space under any practical situation, a criticism of self-calibration,” in *Proceedings of the IEEE International Conference on Computer Vision*, pp. 790–796, 1998.

[10] “AI-Automated Sports Camera, Streaming & Analytics | Pixellot.” Pixellot: AI-Automated Sports Camera, Streaming & Analystics, https://www.pixellot.tv.

[11] M. Merler, D. Joshi, Q. B. Nguyen, S. Hammer, J. Kent, J. R. Smith, and R. S. Feris, “Automatic Curation of Golf Highlights using Multimodal Excitement Features,” *IEEE Transactions on Multimedia*, vol. 21, no. 5, pp. 1147–1160, 2018.

[12] J. Chen and J. J. Little, “Where should cameras look at soccer games, Improving smoothness using the overlapped hidden Markov model,” *Computer Vision and Image Understanding*, vol. 159, pp. 59–73, 2017.

［13］K. K. Rachavarapu, M. Kumar, V. Gandhi, and R. Subramanian, “Watch to edit: Video retargeting using gaze,” In *Computer Graphics Forum*, vol. 37, no. 2, pp. 205–215, 2018.
［14］Y. Sugano, X. Zhang, and A. Bulling, “AggreGaze: Collective Estimation of Audience Attention on Public Displays,” in *Proc. 29 th ACM Symposium on User Interface Software and Technology*, pp. 821–831, 2016.
［15］R. J. K. Jacob, “What you look at is what you get: eye movement-based interaction techniques,” in *Proceedings of the SIGCHI Conference on Human Factors in Computing Systems*, pp. 11–18, 1990.
［16］X. Zhang, Y. Sugano, M. Fritz, and B. Andreas, “Appearance-Based Gaze Estimation in the Wild,” in *Proceedings of the IEEE Conference on Computer Vision and Pattern Recognition*, pp. 4511–4520, 2015.
［17］Y. Kodama, Y. Kawanishi, T. Hirayama, D. Deguchi, I. Ide, H. Murase, H. Nagano, and K. Kashino, “Localizing the Gaze Target of a Crowd of People,” *Asian Conference on Computer Vision workshop*, pp. 15–30, 2018.
［18］K. Abe, C. Nakamura, Y. Otsubo, T. Koike, and N. Yokoya, “Spectator Excitement Detection in Small-scale Sports Events,” in *Proceedings of the 2nd International Workshop on Multimedia Content Analysis in Sports*, pp. 100–107, 2019.
［19］阿部和広，髙山侑也，大坪洋介，小池哲也，“スポーツフィールドにおける自己校正を使った観客の注視領域推定，”*人工知能学会全国大会論文集*，第36回，4Yin2–15, 2022.

阿部和広　Kazuhiro ABE
先進技術開発本部 数理技術研究所
Mathematical Sciences Research Laboratory
Advanced Technology Research & Development Division

大坪洋介　Yosuke OTSUBO
先進技術開発本部 数理技術研究所
Mathematical Sciences Research Laboratory
Advanced Technology Research & Development Division

髙山侑也　Yuuya TAKAYAMA
先進技術開発本部 数理技術研究所
Mathematical Sciences Research Laboratory
Advanced Technology Research & Development Division

小池哲也　Tetsuya KOIKE
先進技術開発本部 数理技術研究所
Mathematical Sciences Research Laboratory
Advanced Technology Research & Development Division


阿部和広
Kazuhiro ABE


髙山侑也
Yuuya TAKAYAMA


大坪洋介
Yosuke OTSUBO


小池哲也
Tetsuya KOIKE

リアルタイムシステム同定法に基づくモデル構築（制御系の異常検知に適したモデル構築手法の提案）†

箱田文彦

Model Construction Based on Real-Time System Identification Method (Proposal of a Model Construction Method for Anomaly Detection of Control Systems)

Fumihiko HAKODA

測定データに基づき制御系設計モデルを構築する手法としてシステム同定法がある．リアルタイムシステム同定法は，システム同定法をハードウェア演算に基づく高速処理で拡張することにより，制御対象の瞬時特性を反映した数値モデルの構築や，実稼働中の制御系のモニタリング，及び異常検知を可能とする手法である．本研究では，システム同定法におけるパラメトリックモデルのうち，最も簡易な ARX モデルを対象にハードウェア設計/実装を行い，パラメーター推定に要する時間を大幅に短縮した．一方，実稼働中システムの特性を推定する場合，必然的に閉ループ条件下でのシステム同定となり，場合によっては装置の駆動指令が一定値となることなどから，推定精度の悪化が問題となる．この問題に対して，入力信号条件を考慮した上で，モデルパラメーターの一部を固定するパラメーター推定手法を考案し，その有効性を実験で検証した．実験結果より，提案手法が推定精度と計算安定性の両立を実現することを確認した．

Real-time system identification is a technique for the monitoring or anomaly detection of control systems, and it enables us to construct numerical models reflecting on the instantaneous properties of control objects by hardware acceleration. In our research, ARX model is selected for the abovementioned purpose and its implementation on field programmable logic devices considerably shortens parameter estimation time. However, in the application of real-time system identification, there arise difficulties derived from closed-loop system identification and the consequent ill-conditions. Real-time system identification is supposed to be used for actual machine operations, therefore, the reference signals for control are sometimes set to constant which are understandably insufficient for system identification. This problem can be addressed by a modified estimation procedure considering input signal conditions and a model with partially fixed parameter values. The effectiveness of the proposed method is investigated by experiments. They show us that both of accuracy and stability in parameter estimation are obtained.

Key words システム同定，信号処理，入力信号条件，ハードウェア設計，異常検知
system identification, signal processing, input signal conditions, hardware design, anomaly detection

1 はじめに

近年，制御系設計においてモデルベースの開発方法が取り入れられており，産業用精密機械における制御系設計プロセスも変わりつつある［2］．モデルベース開発を実現する上で必要となるのが，制御対象の特性を高い精度で表現した数値モデルであり，このモデルを構築する方法の一つに，制御対象の入出力データに基づくシステム同定法がある［3］，［4］．システム同定法は，予め用意した入力データと，その入力によって駆動された装置の出力データをセットにした演算により，制御系設計用の数値モデルを得る手法である．また，上述の産業用機械が多数稼働する工業プラントにおいては，生産性の向上などを目的に装置データが大量に取得されるようになり，得られたデータに基づいて，故障検知，故障予測，生産状況のモニタリングといった解析が行われている［5］，［6］．この異常検知機能は，故障回避による事故対応コストの削減，生産性・安全性の向上などの効果をもたらす可能性がある一方で，検知目的に

† 本稿は，著者の引用文献［1］の式展開の記述を簡略化し，実験を中心に結果を再編したものである．

合ったデータをモニタリングできなければ，誤報（誤った故障通知）によって，現場における混乱，サポートリソースの浪費といった生産性悪化の事態にもつながりかねない．Fig. 1 は産業用機械のモニタリングシステムの例で，位置決め偏差やモーター推力をモニターすることで，モーター故障時にはこれらの値の変化から異常検知が可能である．ただし，モーター推力は装置の稼働条件に応じて大きく変化することから，入力条件をログデータとして出力しないデータ解析系では，装置の稼働条件の変化と異常とを区別できない問題がある．

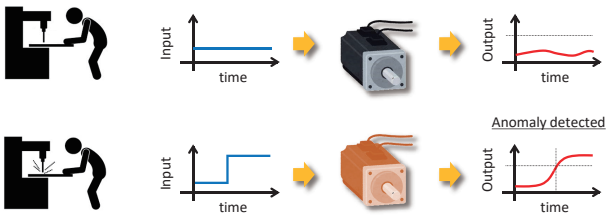

Fig. 1　Data monitoring and analysis in industrial plants.

前述したシステム同定法の適用と工業プラントにおける異常検知の課題に対して，装置の稼働に同期してシステム同定演算を実行可能なリアルタイムシステム同定法の開発を進めている．Fig. 2 はリアルタイムシステム同定法の概略を示したもので，モデル推定を各時刻で行うことにより，装置の稼動状態に応じたモデル更新が可能となる．このリアルタイムシステム同定法によるモデル構築機能を制御器の再設計に用いれば，モデルベース開発を補うことができ，制御系の異常検知に用いれば，入力データと出力データの両方を用いて装置パラメーターを推定していることから，目標値や補正値といった装置の稼働条件に依らない異常検知機能が実現する．

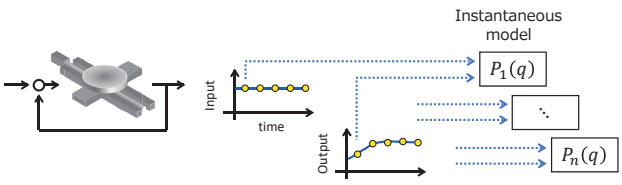

Fig. 2　Real-time system identification.

リアルタイムシステム同定法は上述の利点を有するものの，システム同定法は複雑な演算処理を含み，制御装置上のマイクロプロセッサにそのまま組み込むことは演算負荷上困難である．このため，リアルタイムシステム同定の実現には，システム同定法の演算を高速に実行可能な専用ハードウェアが不可欠と考えられる．本研究では，システム同定法で多用されるパラメトリックモデルの一つである ARX モデルをハードウェア化するとともに，リアルタイムシステム同定の実適用で課題となる閉ループ条件下でのシステム同定，及び入力条件の悪化への対処方法を提案し，その有効性を実験で検証した．

2 リアルタイムシステム同定法

2.1. ARX モデルについて

ARX モデル（Auto-Regressive eXogenous）は，システム同定法で用いられるパラメトリックモデルの中で最も基本的なモデルであり，計算の容易さから幅広く用いられている［7］，［8］．

離散化されたシステムの入出力関係を式（1）によって定義する．ここで，k はサンプル時刻，$y(k)$ は出力，$u(k)$ は入力，$v(k)$ は外乱またはノイズである．

$$\begin{aligned} &y(k)+a_1y(k-1)+\cdots+a_ny(k-n)\\ &=b_1u(k)+b_2u(k-1)+\cdots+b_mu(k-m)+v(k)\end{aligned} \tag{1}$$

q はディジタル信号のシフトオペレーターで，式（2）で定義する．

$$q^{-1}u(k)=u(k-1) \tag{2}$$

多項式の係数パラメーターを式（3）のようにまとめる．

$$\begin{aligned} A(q)&=1+a_1q^{-1}+\cdots+a_nq^{-n}\\ B(q)&=b_1q^{-1}+\cdots+b_mq^{-m}\end{aligned} \tag{3}$$

外乱 $v(k)$ として白色外乱 $w(k)$ を仮定すると，式（1）は式（4）に書き改められる．

$$A(q)y(k)=B(q)u(k)+w(k) \tag{4}$$

Fig. 3 は式（4）をブロック線図で表現したもので，出力側の多項式 $A(q)y(k)$ は自己回帰部分，入力側の多項式 $B(q)u(k)$ は外生入力部分である．このモデルでは，外乱及びノイズが外生入力に直接に加算されず，パラメーターはデータに対して線形であり，一括最小二乗法により計算できる．

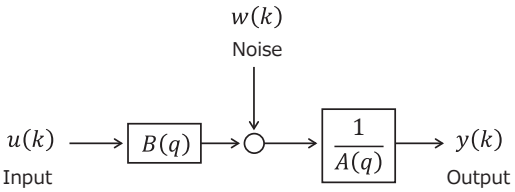

Fig. 3　Block diagram of ARX model.

2.2. ARX モデルのハードウェア化

ARX モデルにおいて，パラメーター推定演算の核となる部分は前述の最小二乗法における逆行列演算である．逆行列演算の解法としては，ガウスの消去法及びその一般形である LU 分解が広く利用されているが，ハードウェア化を考えた場合に必ずしも効率的でない．ここでは，ハード

ウェア化に適した QR 分解を用いる．

QR 分解では，式（5）のように行列 $\boldsymbol{A}$ を直交行列 $\boldsymbol{Q}$ と上三角行列 $\boldsymbol{R}$ の積に分解する．

$$\boldsymbol{A}=\boldsymbol{QR} \tag{5}$$

ここで，直交行列 $\boldsymbol{Q}$ と上三角行列 $\boldsymbol{R}$ は式（6）及び式（7）に示すような行列である．

$$\boldsymbol{Q}=\begin{bmatrix} & & \\ q_1 & \cdots & q_n \\ & & \end{bmatrix} \tag{6}$$

$$\boldsymbol{R}=\begin{bmatrix} r_{11} & & r_{1n} \\ 0 & \ddots & \\ 0 & 0 & r_{nn} \end{bmatrix} \tag{7}$$

直交行列とは列ベクトルの長さが全部 1 で，しかもお互いに直交している行列である．直交行列の条件数は 1 で数値的に常に安定である．直交行列は転置すると逆行列になることから，

$$\boldsymbol{Q}^T\boldsymbol{Q}=\boldsymbol{I} \tag{8}$$

ここで，$\boldsymbol{I}$ は単位行列である．正規方程式として以下の式（9）を考える．

$$\boldsymbol{A\theta}=\boldsymbol{b} \tag{9}$$

式（7）で定義した $\boldsymbol{R}$ を用いると，$\boldsymbol{R}$ は上三角行列なので以下の後退代入により解が求まる．

$$\boldsymbol{QR\theta}=\boldsymbol{b} \tag{10}$$

$$\boldsymbol{Q}^T\boldsymbol{QR\theta}=\boldsymbol{Q}^T\boldsymbol{b} \tag{11}$$

$$\boldsymbol{R\theta}=\boldsymbol{Q}^T\boldsymbol{b} \tag{12}$$

QR 分解を計算する方法として，ギブンス回転，ハウスホルダー変換，グラム・シュミット分解があるが，この内でハードウェア化により演算の高速化が可能となるのはギブンス回転を CORDIC アルゴリズムで実行した場合となる．

2.3. 入力条件に依存した推定精度の悪化

リアルタイムシステム同定は稼働中の装置を対象とした手法であり，必然的に閉ループ条件下のシステム同定となる．閉ループシステム同定は入力信号の加振条件及び観測ノイズ条件により，モデル推定精度に制約を受けることが知られている［9］．Fig. 4 は外部信号と観測ノイズのある閉ループシステムのブロック線図である．ここで，$r(k)$ は外部信号，$F(q)$ は制御器，$G(q)$ は制御対象の伝達関数，$e(k)$ は観測ノイズ，$y(k)$ は観測出力，$u(k)$ は制御入力である．閉ループシステム同定は $F(q)$ による制御の下で，入出力データ $u(k)$ と $y(k)$ から制御対象 $G(q)$ を推定することである．

伝達関数の推定値 $\hat{G}(e^{j\omega})$ は，式（13）に示すように入力のスペクトル密度 $\Phi_{uu}(e^{j\omega})$ と入出力のクロスペクトル密度 $\Phi_{uy}(e^{j\omega})$ の比から計算される．また，$\Phi_r(e^{j\omega})$，$\Phi_e(e^{j\omega})$ はそれぞれ外部信号，観測ノイズのスペクトル密度である．

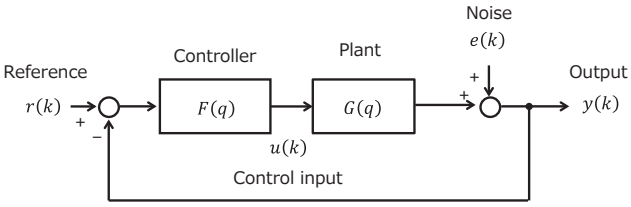

Fig. 4　Close-loop system with external input and noise.

$$\hat{G}\left(e^{j\omega}\right)=\frac{\Phi_{uy}\left(e^{j\omega}\right)}{\Phi_{uu}\left(e^{j\omega}\right)}=\frac{G\left(e^{j\omega}\right)\Phi_r\left(e^{j\omega}\right)+\dfrac{\Phi_e\left(e^{j\omega}\right)}{F\left(e^{j\omega}\right)}}{\Phi_r\left(e^{j\omega}\right)-\Phi_e\left(e^{j\omega}\right)} \tag{13}$$

ここで，観測ノイズの影響が無視できる場合（$\Phi_e(e^{j\omega})=0$）でも，外部信号が帯域制限を受ける場合，すなわち $\Phi_r(e^{j\omega})$ がある周波数領域で値を持たない場合には，次式でゼロ除算が生じ，プラントの推定精度は悪化する．

$$\hat{G}\left(e^{j\omega}\right)=\frac{G\left(e^{j\omega}\right)\Phi_r\left(e^{j\omega}\right)}{\Phi_r\left(e^{j\omega}\right)}\neq G\left(e^{j\omega}\right) \tag{14}$$

外部信号の帯域幅がパラメーター推定精度に影響するのは，開ループのシステム同定でも同様であるが，開ループのシステム同定では必要に応じて外部信号の信号レベルまたは帯域幅を増加させられるのに対し，閉ループ条件下では入力信号を自由に変更することはできない．このことは，リアルタイムシステム同定法の課題であり，以下に示す入力条件に応じた推定演算の修正が必要となる．

2.4. 入力条件を考慮したパラメーター推定

リアルタイムシステム同定法によるモデル推定では，入力条件（外部信号）がモデル推定精度に大きく影響する．ここでは，位置決め制御の場合を例に取り，入力が悪条件となる場合にもモデル推定精度への影響を低減可能な方法を検討する．Fig. 5 は位置決め制御系の外部信号（目標値），推力，位置偏差を示したもので，外部信号は赤太枠の立ち上がり時では大きく変化するものの，赤点線枠の一定速区間で入力は平滑となる．推定モデルの周波数応答は右

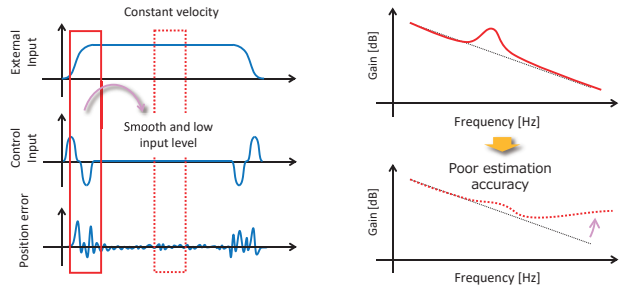

Fig. 5　Input signal condition and parameter estimation accuracy.

図のように立ち上がり時には正常な推定結果が得られるものの，一定速区間では不安定な推定結果となる．同じ制御対象のモデルを推定しているにもかかわらず，推定結果には大きな差異が生じる．

Fig. 6 に入力条件（外部信号）によるモデル推定精度の低下を回避する方法を示す．閉ループ条件において，一定区間のデータに対して入力信号条件を計算することで，パラメーター推定方法を変更する．

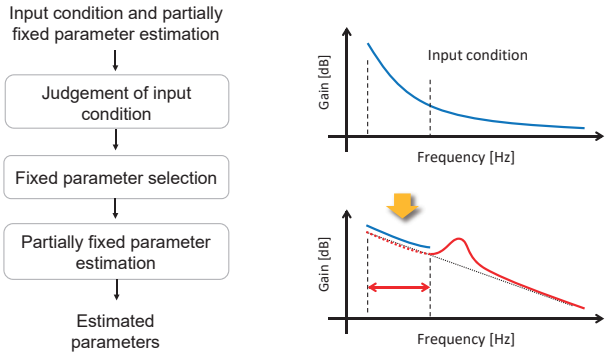

Fig. 6　Partially fixed parameter estimation based on input signal condition.

以下，位置決めステージを例に具体的な手順を説明する．推定対象モデルとして次式を考える．

$$y(k)=G(q)u(k) \tag{15}$$

位置決めステージでは，式（15）の $G(q)$ は剛体特性（剛体モード）を表す $G_{rigid}(q)$ と共振特性（共振モード）を表す $G_{reso}(q)$ の和（剛体モードと共振モードの重ね合わせ）として記述できる．

$$G(q)=G_{rigid}(q)+G_{reso}(q) \tag{16}$$

もし，共振特性を表す $G_{reso}(q)$ が推定済みで既知であれば，その出力 $y(k)$ への寄与分は計算できる．そこで，推定済みモデル $\hat{G}_{reso}(q)$ を用いて，共振特性の出力への寄与分 $y_{reso}(k)$ を計算する．これにより，共振特性を表すモデルは推定対象から外すことができ，そのパラメーターは固定されたことになる．

$$y_{reso}(k)=\hat{G}_{reso}(q)u(k) \tag{17}$$

出力 $y(k)$ の剛体特性分は，出力 $y(k)$ から共振特性分 $y_{reso}(k)$ を差分することで得られる．

$$y_{rigid}(k)=y(k)-y_{reso}(k) \tag{18}$$

剛体特性を表す $G_{rigid}(q)$ は，入力 $u(k)$ と剛体特性分の出力 $y_{rigid}(k)$ から推定できる．

$$y_{rigid}(k)=\hat{G}_{rigid}(q)u(k) \tag{19}$$

以上，パラメーターの一部を固定した手法により，対象モデルは以下の様に推定される．

$$\hat{G}(q)=\hat{G}_{rigid}(q)+\hat{G}_{reso}(q) \tag{20}$$

また，システム同定法における入力条件の判断方法として，入力信号のスペクトル密度を全周波数領域で積分した累積スペクトル密度を指標として用いる．

$$\psi_u=\int_{-\infty}^{\infty}\Phi_{uu}(e^{j\omega})d\omega \tag{21}$$

上式に基づき良条件となるパラメーターに推定を限定することで，推定精度の悪化を回避する．

3 実験検証

3.1. 実験装置

Fig. 7 に示すボールねじ駆動方式の位置決めステージを対象にリアルタイムシステム同定法の有効性を評価する．

まず，リアルタイムシステム同定法の比較対象として，通常のシステム同定法（オフラインシステム同定法）によるモデル推定を行う．システム同定に使用した入力は疑似ランダム信号（M 系列信号）である．モデル次数を 4 次とした推定結果を Fig. 8 に示す．

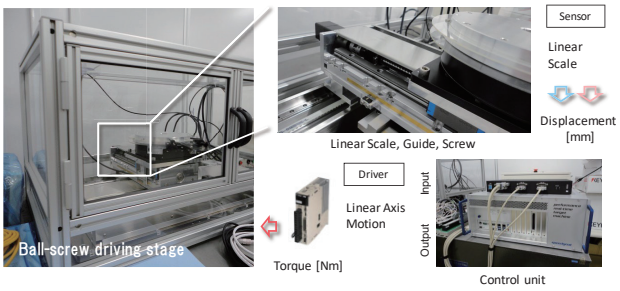

Fig. 7　Ball-screw driving stage for the evaluation of real-time system identification.

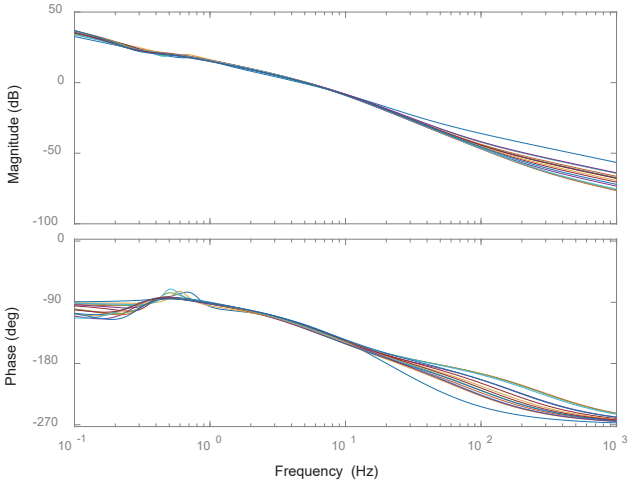

Fig. 8　Frequency responses at multiple stage positions by off-line system identification.

3.2. リアルタイムシステム同定の適用

Table 1 にハードウェア実装対象の FPGA ボード示す．FPGA として用いる Intel 社製 Cyclone V は普及用途向けであり，同社の製品ラインナップでは最も安価に入手可能なデバイスのひとつである．ハードウェア設計には同社の統合開発ツールである Quartus II を用いるとともに，アルゴリズムの高位合成ツールである DSP Builder を使用する．Table 2 に演算負荷の比較対象である CPU ボードの仕様を示す．

Table 1　Specifications of FPGA board.

Items	Description
FPGA device	Intel Cyclone V FPGA
Development software tool	Quartus II DSP Builder（MATLAB/Simulink）

Table 2　Specifications of CPU board.

Items	Description
CPU device	Renesas Electronics SH-4A （R8A77850 600 MHz）
Development software tool	GNU C++ Compiler

Table 3 にリアルタイムシステム同定法による演算処理時間を示す．表中の Step1–5は，Fig. 9 に示した ARX モデルにおけるパラメーター推定の演算フローに対応しており，各処理の内訳を表している．この演算時間は0.1秒間分の入出力データを処理したもので，FPGA を用いた場合には全体で 10.2 μ 秒，CPU を用いた場合には 852 μ 秒を要す．この結果より，FPGA の処理時間は CPU の場合の100分の 1 程度となり，大幅な演算の高速化を実現できることが分かる．たとえば，位置決め制御サーボサイクルを1kHz とした場合，演算処理を CPU で実行すると演算負荷が計算能力を超過するのに対し，FPGA を用いた場合には他の演算処理または信号処理を組み込む余裕を有している．

Table 3　Comparison of calculation time by FPGA and CPU.

Step	Calculation load［usec］		
	FPGA	CPU	ratio［%］
1	0.73	15.24	4.77
2	0.03	1.35	2.05
3	0.80	12.01	6.63
4	0.13	5.89	2.24
5	8.52	817.93	1.04
Total	10.20	852.41	1.20

続いて，パラメーター推定結果について述べる．Fig. 10 は入力条件を考慮せずにパラメーター推定を行った場合で

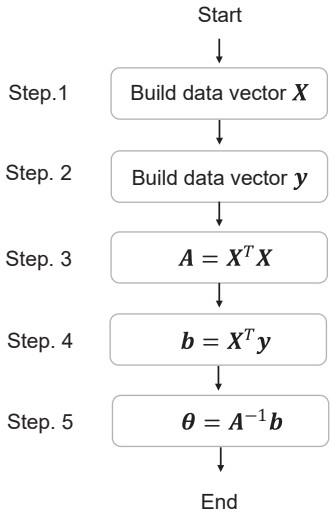

Fig. 9　Flow chart of parameter estimation.
Step.1 and 2: Data vectors $\boldsymbol{X}$ and $\boldsymbol{y}$ are assembled. Step.3 and 4: $\boldsymbol{X}^T\boldsymbol{X}$ and $\boldsymbol{X}^T\boldsymbol{y}$ are calculated. Step.5: Parameters are calculated by solving Linear equation.

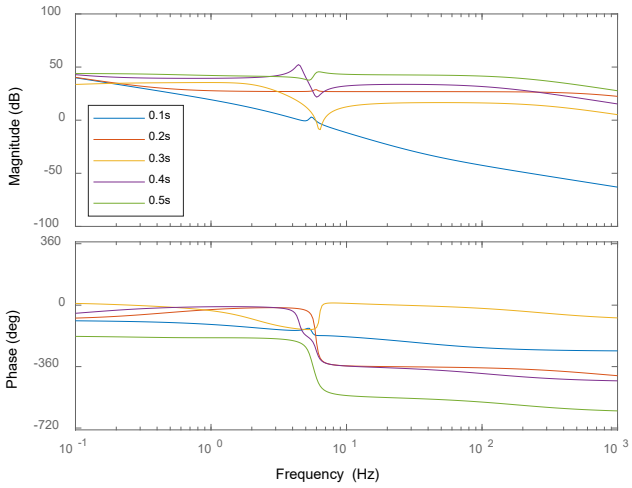

Fig. 10　Frequency responses at multiple stage positions without the consideration of input signal conditions.

ある．外部信号の立ち上がり時である0.1秒までのデータで推定したモデルは Fig. 8 のオフライン推定の結果と同様にステージの質量特性を反映した周波数応答を示しており，妥当な推定結果と判断できる．一方，0.2秒以降のデータを用いて推定したモデルはオフライン推定の結果から大きく乖離しており，入力条件を考慮せずにモデル推定を行う場合に妥当な推定結果は期待できない．

最後に，入力条件を考慮してパラメーターの一部を固定した場合の推定結果を Fig. 11 に示す．0.1秒以降で入力が平滑となった場合でもパラメーター推定は安定しており，閉ループ条件下において入力条件が悪化する問題への有効な対処法になっていると判断できる．また，周波数応答の変動は主に低周波領域で生じており，実システムの特性を反映した結果といえる．本実験結果より，ステージ位置に応じた制御対象特性の推定が可能となり，リアルタイムシ

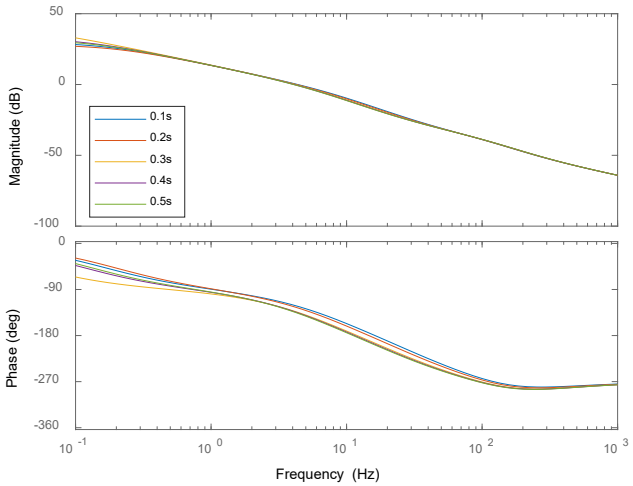

Fig. 11 Frequency responses at multiple stage positions with the consideration of input signal conditions.

ステム同定法の妥当性が検証できた.

4 まとめ

本研究では，ハードウェアを用いてシステム同定演算処理を高速化するリアルタイムシステム同定法を構築し，その有効性を検証した．得られた成果を活用すれば，制御系の異常検知や制御系再設計の端緒として利用するばかりでなく，冒頭に述べたモデルベース開発や工業プラントにおけるデータ解析の進展にも貢献できると考えられる.

引 用 文 献

[1] 箱田文彦，“リアルタイムシステム同定法に基づくモデル構築（制御系の異常検知に適したモデル構築手法の提案），”*日本機械学会論文集*，vol. 88, no. 914, 2022.
[2] 大畠明，“プラントモデリングの地平線，”*計測と制御*，vol. 53, no. 4, pp. 272-277, 2014.
[3] 堀惇史，古井達也，岩倉大輔，野波健蔵，“産業用マルチロータヘリコプタのオンラインシステム同定機構を有する自動チューニング適応 I-PD 制御，”*日本機械学会論文集 C編*，vol. 82, no. 834, 2016.
[4] 高梨宏之，涌井伸二，“多自由度除振装置のシステム同定手順に関する一考察，”*日本機械学会論文集 C編*，vol. 76, no. 764, pp. 851-860, 2010.
[5] 藤巻遼平，中田貴之，塚原英徳，佐藤彰典，山西健司，“障害診断のための異常パタンマイニング，”*情報処理学会 第70回全国大会講演論文集*，pp. 45-46, 2008.
[6] 蛭田智昭，鈴木英明，藤原淳輔，“機械学習を使った異常検知技術のための定常状態の抽出条件の自動生成手法，”*日本機械学会論文集*，vol. 81, no. 826, 2015.
[7] L., Ljung, *System Identification: Theory for the User 2nd Edition*, PTR Prentice Hall, 1999.
[8] 足立修一，*ユーザのためのシステム同定理論*，社団法人計測自動制御学会，1993.
[9] 佐野昭，“ノンパラメトリックモデルの同定，”*計測と制御*，vol. 28, no. 4, pp. 316-322, 1989.

箱田文彦　Fumihiko HAKODA
先進技術開発本部 数理技術研究所
Advanced Technology Development Division
Mathematical Science Research Laboratory

箱田文彦
Fumihiko HAKODA

プロセス機能展開表を活用した光学ガラスの溶解技術開発†

佐藤幸太，嘉指伸一

Development of Optical Glass Melting Technology using a Process Task Visualization Chart

Kota SATO and Shinichi KAZASHI

光学ガラスの新硝種および改良品の開発にあたり，熔解工程における垂直立ち上げを目指し，実験室での小規模評価に品質工学を活用した．従来は，小規模の実験で工程ごとに部分最適を行い，製造条件を定め，次に大規模な実験で量産できるか確認してきた．しかし，小規模の実験結果が大規模の実験で再現せず，量産立ち上げに時間を要すという問題が生じることがあった．この問題を解決するため，はじめに，工程全体を俯瞰し検討すべき因子を抽出するとともに，工程全体での最適化を検討した．次に，評価尺度と誤差因子を工夫し，大規模な実験で再現する小規模評価方法を確立した．この方法を多くの硝種に展開し，製造技術情報として蓄積すると，その情報は同系統の他の硝種に対しても適用できることが分かった．その結果，新たに開発した硝種であっても，直交表実験を行わずに短期間に量産立ち上げを実現した．

In the development of new and improved types of optical glass, we have applied quality engineering to small-scale evaluation in the laboratory, with the goal of vertical ramp-up in the melting process. Previously, we had optimized each process individually in small-scale experiments, determined the optimal production conditions, and then carried out a large-scale experiment to confirm that these conditions were actually suitable for volume production. A problem that had sometimes delayed the start of volume production in the past was that the small-scale experimental results could not be replicated in the large-scale experiment. To solve this problem, we started by surveying the entire process, selecting the factors to be studied, and studying the optimization of the process as a whole. Next we adjusted the evaluation metrics and noise factors to obtain small-scale evaluation methods that would give results that could be replicated in large-scale experiments. By applying this methodology to many types of glass, we obtained a body of production technology information that turned out to be applicable to many types of optical glass in the same family. The result was that we were able to ramp up volume production of even newly developed types of glass quickly, without performing orthogonal array experiments.

Key words 光学ガラス，内部透過率，SN 比，タグチメソッド，品質工学
optical glass, internal transmittance, S/N ratio, Taguchi methods, quality engineering

1 はじめに

1.1. 光学ガラスについて

光学ガラスは，カメラや望遠鏡，顕微鏡など光学機器において像の伝達に用いられるガラスであり，レンズやプリズムとして使用される．光学ガラスの光学的性質を表す光学定数は，Fig. 1 に示すように，d 線（波長 587.6 nm）に対する屈折率 nd と，色分散を表すアッベ数 vd の二つの組合せで分類される．F 線（波長 486.1 nm），C 線（波長 656.3 nm）に対する屈折率をそれぞれ nF, nC で表すと，アッベ数は次式で定義される．

$$\nu_d = \frac{n_d - 1}{n_F - n_C} \tag{1}$$

Fig. 1 中の領域分けは，大別するとクラウン（vd が55以上），フリント（vd が50以下）に分けられる．さらに，特徴的な化学成分によって細かく領域が分けられており［1］，例えば，最も左下の領域は，ふっ化物（F）を加えたクラウン（K）であることから，FK 領域と呼んでいる．

像の精度を高めるためには，収差を取り除く必要がある．例えば，光の屈折率が波長によって違うことに起因する色収差は，光学定数の異なるレンズを組み合わせて除去する．

† 本稿は，著者の引用文献［8］の一般社団法人品質工学会より許諾を得ている．

他にも様々な収差を取り除くため，多くの硝種（ガラス材料の品種）が必要となる．近年の光学機器の高性能化，小型化に伴い，新硝種の開発や既存硝種の改良に対する要求はますます高まっており，それらの硝種を短期間に量産立ち上げすることが極めて重要である．

1.2. 課題に対するアプローチ

従来は，新硝種や既存硝種の改良品を量産立ち上げする場合，小規模実験で工程ごとに制御因子の水準を振って製造条件を定め，大規模な実験で量産性を確認してきた．しかし，小規模と大規模な実験では規模に差があるだけでなく，溶解プロセスも異なるため，小規模実験で得られた結果が大規模実験で再現しないという課題が生じていた．

この課題を解決するため，本研究では，①プロセス機能展開表［2］を活用し，広範囲の工程で同時最適化を検討した．次に，②評価尺度と誤差因子を工夫し，大規模な量産で小規模実験の結果が再現する評価方法を確立した．この評価方法を他の硝種における直交表実験に展開した結果，評価方法の有効性と汎用性を確認できたので，③その実験結果をロバストエンジニアリング（RE）情報［3］として蓄積した．その情報は，同系統の他の硝種に対しても適用できることが分かり，新たに開発した硝種であっても，直交表実験レスで，短期間に量産立ち上げを行うことができたので，以下に報告する．

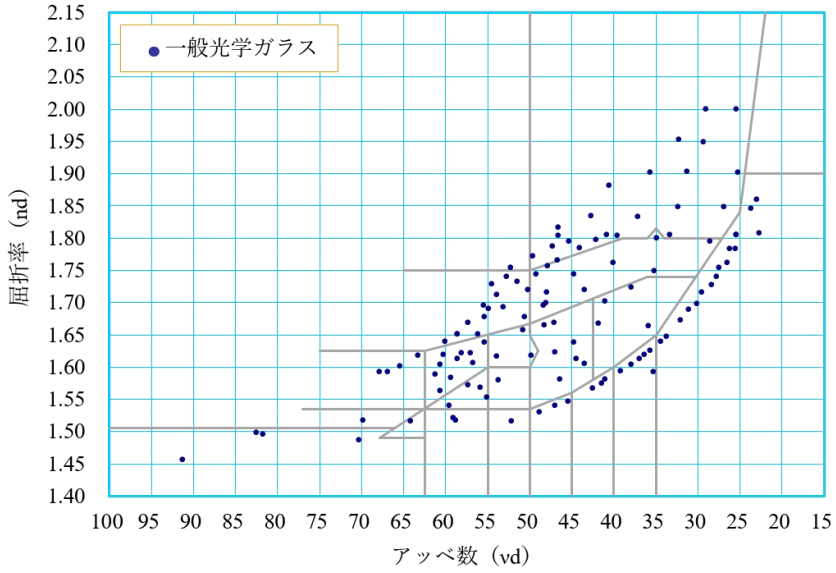

Fig. 1　nd -vd ダイアグラム（光ガラス株式会社）

Table 1　光学ガラスの開発・設計からガラス製造までの横型プロセス機能展開表

工　程	開発・設計		製　造							
	組成設計	調合組成	原料選定	調　合		前溶解	混合・配合	連続溶解	成　形	ラフアニール
				ひょう量	混　合					
工程の目的	顧客要望に沿った光学ガラスの性能になるよう組成を設計する。	設計された組成の元素比率になるよう、使用する原材料の種類や割合を決める。	調合組成で決めた原材料のメーカや純度を選定する。	ガラス種や調合する量によって決められた複数の原料を精度高く計量する。	ひょう量した複数の原料を均一に混ぜ合わせる。	調合した原料を溶解炉に投入し熱を加え均一なガラスフリットを作る。	ガラスフリットを均一に混ぜ合わせる。目標の光学定数になるよう複数のフリットを均一に配合する。	配合されたガラスフリットを再度溶解し泡、脈理の無い均質度と透過率の高いガラス融液にする。	ガラス融液を均一に冷却し目的の形状に成形する。	成形したガラスが割れないように、ゆっくり冷まして均一にひずみを下げる。
工程の機能（働き）	nd, vdなど 元素比率	元素比率 原料比率	比率 投入量	比率 投入量	比率 時間	反応率 熱量	比率 時間	温度 熱量	温度 時間	温度 時間
制御因子	・元素種類 ・元素比率	・塩の種類 炭酸塩など ・添加材種類 脱泡材など ・添加材量	・原料メーカ ・不純物規格 ・結晶系	・ひょう量順序 ・器具種類	・混合機種 ・混合条件	・溶解条件	・混合機種 ・混合条件	・溶解条件 ・撹拌条件	・冷媒種類 ・冷却量 ・温度バランス	・降温速度 ・温度 ・ヒータ距離
工程内の誤差因子		・製法 ・純度	・製法 ・規格内変動	・環境 ・劣化 ・疲労	・場所 ・環境 ・劣化	・場所 ・環境 ・劣化 ・炉体差	・場所 ・環境 ・劣化	・場所 ・環境 ・劣化 ・炉体差	・場所 ・環境 ・劣化 ・機差	・場所 ・劣化
標示因子		・硝種	・硝種	・原料種類	・硝種	・硝種	・硝種	・硝種	・硝種 ・成形サイズ	・硝種
システム分割	従来の範囲 ←----------→					←----------→	←----------→	←----------→	←----------→	
	今回の範囲 ←----------									----------→

2 プロセス機能展開表

Table 1 に，光学ガラスの開発設計からガラス製造までの横型プロセス機能展開表を示す．本表は，開発・設計から製造までのプロセスについて，工程順に，工程の目的とその工程の機能，制御因子，工程内の誤差因子，標示因子，システム分割の範囲を表にしたものである．

工程の目的には，各工程の目的について，理想の状態を表現した．工程の機能には，その工程の目的を達成するための機能を働きとして記述した．制御因子には，その工程で決めなければならない条件をリストアップするとともに，従来は検討していなかった因子も抽出した．工程内の誤差因子には，その工程のばらつき要因をリストアップした．本研究の場合，硝種はある範囲では誤差因子であるが，広い範囲では標示因子とした．また，劣化は，各工程で用いる設備の経年劣化を表し，製造条件のばらつきを生む．ある範囲ではフィードバックを行っているが，そのような環境や装置性能の変化に対してロバストにする必要があると考えた．最後の行には，システム分割の範囲を示した．

この表を用いて全体を俯瞰すると，組成設計で求めた元素の比率は，光学定数や化学的性質，熱的性質，機械的性質などが変化するため，硝種ごとの実験では固定条件となる．その他に硝材に要求される性質（Table 2）については，

Table 2　光学ガラスの硝材に要求される性質［4］

性　質	内　　容
光学定数	屈折率，分散など
化学的性質	耐酸性，耐水性など
熱的性質	ガラス転移点など
機械的性質	摩耗度など
その他	透過率，泡・異物，脈理など

従来の範囲の実験において，範囲外の固定条件が変化すると崩れてしまった．よって，調合組成からラフアニールまでの工程全体を一つのシステムとして，同時に最適化することを検討した．

3 実　験

3.1. 基本機能の検討

溶解の目的は，調合した原材料に熱を加え，均質なガラス融液を得ることである．この融液は，ガラス化反応によって得られることから，Fig. 2 に示す基本機能を考えた．溶解規模差によって生じる熱量の違いを Fig. 3 に，大規模量産における場所 P によるガラス化反応の違いを Fig. 4 に示す．小規模と大規模な量産では，原材料やガラス融液に

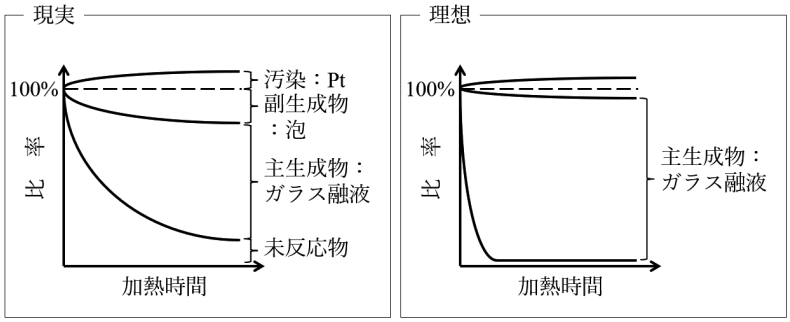

Fig. 2　ガラス溶解の基本機能

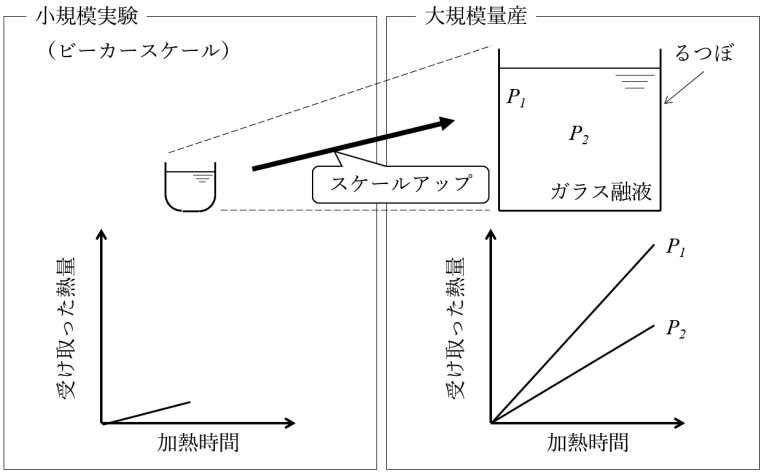

Fig. 3　熱量の溶解規模差

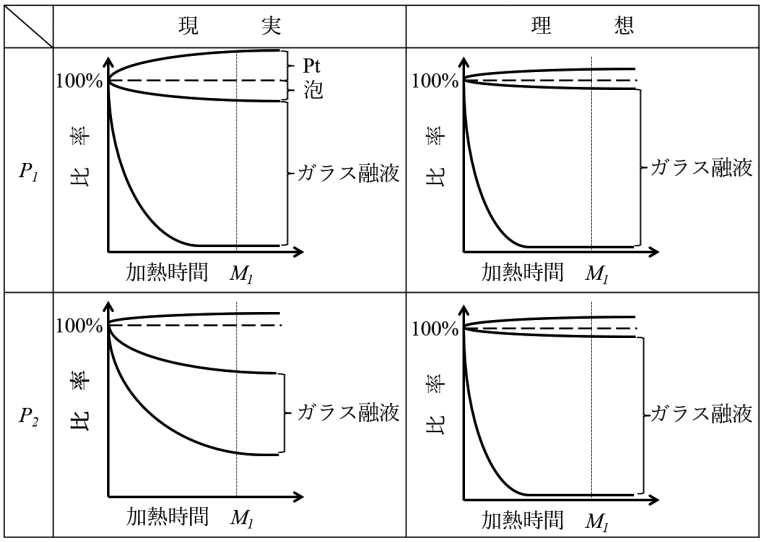

Fig. 4　大規模量産における場所による反応の違い

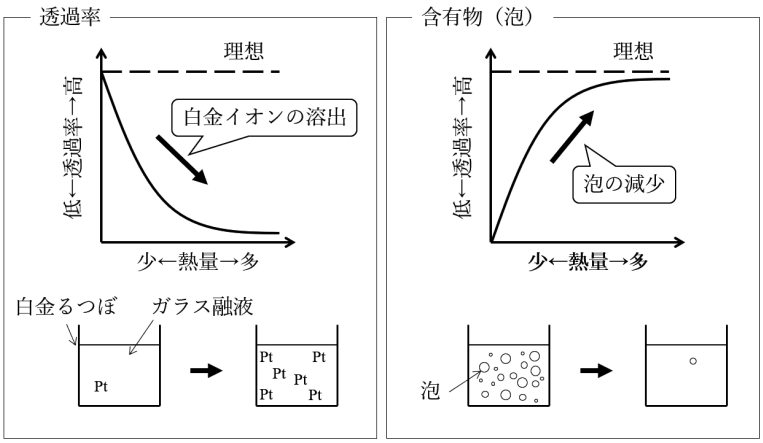

Fig. 5　熱量に対する透過率と含有物の関係

与える熱量に差が生じる．さらに，量産では規模が大きいため，場所によって受け取る熱量の違いが生じやすい．その結果，成分の不均一が生じることで，光を透して屈折させるという機能が低下すると考えた．したがって，熱量によらずガラス化反応が安定し，反応速度が速いことを理想と考えた．

3.2. 評価尺度と直交表の割付け

原材料が受け取った熱量や，反応率の測定は難しいので，その代用として，光を透すという機能に着目した．Table 2 で示した性質の中で，熱が加わる溶解工程では，透過率と泡品質がトレードオフの関係となる（Fig. 5）．熱量を大きくすると，るつぼの材質である白金がイオン化してガラス融液に混入し，近紫外域の透過率が低下するが，泡は清澄により除去できる［4］．この現象は，ほぼ全ての硝種に共通する．そこで，熱量によらずガラスの透過率が常に高いことを理想とした．

実際の評価では，光学ガラスの内部透過率を計測した．内部透過率とは，ガラス表面の反射損失を含まない分光透過率のことで，規格［5］にしたがって測定した．Fig. 6（a）に，硝種01の内部透過率曲線を示す．ここで，N_1 は熱量の少ない条件であり，N_2 は熱量の多い条件である．N_1 では，白金イオンの混入が少ないため，400 nm 以下の波長域の内部透過率が高くなるが，400 nm 以上の波長域では，多く残存した泡が光の透過を阻害し，内部透過率が下がっている．内部透過率を用いることで，一つのテストピースで透過率と泡を同時に評価できると考えた．

信号因子は加熱時間と考えて実験した．信号水準を増やすと実験数が増えてしまうため，1 水準とした．誤差因子は，大規模な量産での場所の違いとして，加熱時間以外で熱量を変化させる因子を Table 1 から抽出し，調合して直交表 L_{18} の外側に割り付けた（2 水準）．誤差因子の水準値 N_1 は，予備実験を行い，ガラス化するのに最低限必要な値とした．

内部透過率は，算術的加法性を持たせるため，式（2）でオメガ変換値 Ω を求めた［6］．ここで p は，内部透過率を表す．

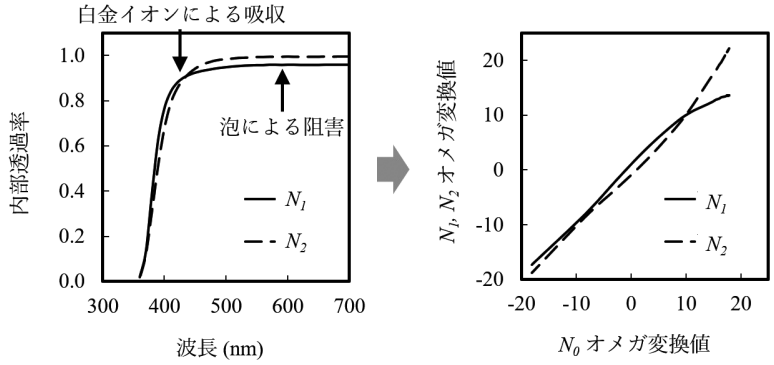

（a）内部透過率曲線　　（b）標準SN比への変換

Fig. 6　内部透過率曲線と標準 SN 比への変換

$$\Omega = 10log\left(\frac{p}{1-p}\right) \qquad (2)$$

オメガ変換値について，N_1，N_2 の平均値 N_0 に対して，N_1，N_2 をプロットしたグラフを Fig. 6（b）に示す．誤差因子に対する内部透過率の安定性は，N_1，N_2 の平均値を標準条件の出力 N_0 とした標準 SN 比で評価した．

制御因子は，Table 1 から各工程の因子をバランスよく選択し，直交表 L_{18} の内側に割り付けた．

4 硝種01の結果

4.1. 標準 SN 比の計算

直交表 L_{18} に従って，小規模実験で硝種01のテストピースを作製し，内部透過率を測定した．測定結果の例を Table 3 に，標準 SN 比の計算方法を下記に示す．

$$S_T = (-17.37)^2 + (-8.18)^2 + \cdots + 22.19^2$$
$$= 16262.2130$$
$$(f = 2 \times 35 = 70)$$

$$r = (-18.086)^2 + (-8.416)^2 + \cdots + 17.887^2$$
$$= 7804.0274$$

$$L_1 = (-18.086) \times (-17.37) + \cdots + 17.887 \times 13.58$$
$$= 6315.4123$$

$$L_2 = (-18.086) \times (-18.80) + \cdots + 17.887 \times 22.19$$
$$= 9292.6425$$

$$S_\beta = \frac{(L_1 + L_2)^2}{2r} = \frac{(6315.4123 + 9292.6425)^2}{2 \times 7804.0274}$$
$$= 15608.0548$$
$$(f = 1)$$

$$S_{N\times\beta} = \frac{(L_1 - L_2)^2}{2r} = \frac{(6315.4123 - 9292.6425)^2}{2 \times 7804.0274}$$
$$= 567.9055$$
$$(f = 1)$$

Table 3　測定結果の例

	波長 (nm)	内部透過率のオメガ変換値		
		N_0	N_1	N_2
1	360	−18.086	−17.37	−18.80
2	370	−8.416	−8.18	−8.65
⋮	⋮	⋮	⋮	⋮
34	690	17.887	13.58	22.19
35	700	17.887	13.58	22.19

$$S_e = S_T - S_\beta - S_{N\times\beta}$$
$$= 16262.2130 - 15608.0548 - 567.9055$$
$$= 86.2527$$
$$(f = 70 - 1 - 1 = 68)$$

$$V_e = \frac{S_e}{f} = \frac{86.2527}{68}$$
$$= 1.26842$$

$$S_N = S_{N\times\beta} + S_e = 567.9055 + 86.2527$$
$$= 654.1582$$
$$(f = 1 + 68 = 69)$$

$$V_N = \frac{S_N}{f} = \frac{654.1582}{69}$$
$$= 9.4805$$

標準 SN 比

$$\eta = 10log\left(\frac{2r}{V_N}\right) = 10log\left(\frac{2 \times 7804.0274}{9.4805}\right)$$
$$= 32.17\,(db)$$

4.2. 要因効果図と最適条件の決定

硝種01の要因効果図を Fig. 7 に示す．この図より SN 比の大きい水準は，$A_2\ B_2\ C_3\ D_2\ E_1\ F_1\ G_1\ H_2$ となる．

内部透過率は，高いことが理想であるため，目的の波長範囲における N_0 のオメガ変換値を感度とした．感度の要因効果図を Fig. 8 に示す．最適条件として，C_3 を C_1，F_1 を F_3 とし，最終的に，$A_2\ B_2\ C_1\ D_2\ E_1\ F_3\ G_1\ H_2$ とした．

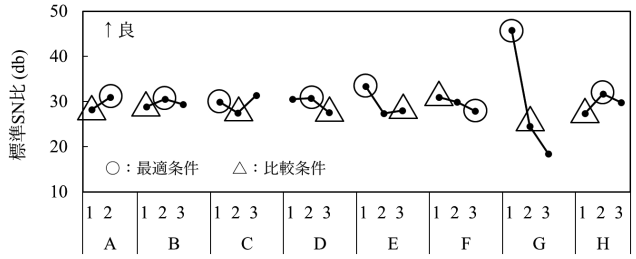

Fig. 7　硝種01における SN 比の要因効果図

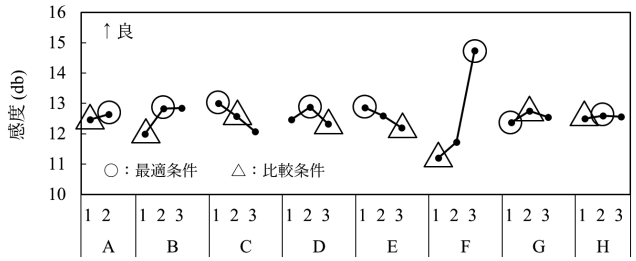

Fig. 8　硝種01における感度の要因効果図

Table 4　推定結果と確認実験の比較

	標準 SN 比（db）		感度（db）	
	推定	確認	推定	確認
最適条件	50.67	48.96	16.05	15.41
比較条件	19.01	17.89	10.13	8.46
利得	31.66	31.07	5.92	6.94

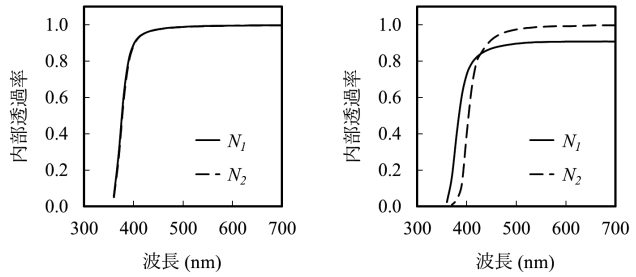

（a）最適条件　（b）比較条件

Fig. 9　確認実験の内部透過率曲線の比較

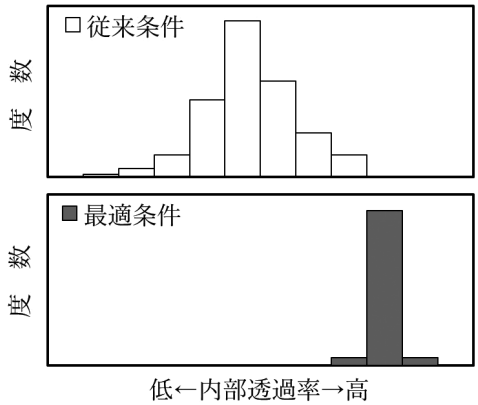

Fig. 10　硝種01における量産再現性の確認
（目的波長の内部透過率のヒストグラム）

4.3. 確認実験

最適条件と比較条件を用いて，確認実験を行った．その結果，再現性が得られた（Table 4, Fig. 9）．最適条件を量産の製造条件に反映すると，大規模な量産でも再現し，従来条件に対して内部透過率の高い硝材を安定して製造することができた（Fig. 10）．

5 直交表実験の多硝種展開とロバストエンジニアリング情報の蓄積

硝種01と同様の直交表実験を，新たに開発した硝種も含め，同系統（γ）の硝種02, 03についても実施した．Table 5 に，各直交表実験の利得再現性を示す．硝種によらず利得再現性が得られたと同時に，量産で高品質の硝材が安定して得られた．硝種01と比較して硝種02以降の利得が小さいのは，制御因子の水準幅を狭めたこと，異なる制御因子も取り上げていることが影響していると考えた．これらより，評価方法の有効性と汎用性を確認できたので，異なる系統（δ）の硝種05～08に対しても直交表実験を実施した．

Table 5　各直交表実験の利得再現性（標準 SN 比）

硝種	直交表	推定利得（db）	確認利得（db）
01	L_{18}	31.66	31.07
02	L_{12}	12.75	13.60
	L_{18}	6.50	6.10
03	L_{18}	12.80	9.95

多くの硝種で実施した直交表実験の結果を技術情報として蓄積するため，一つの表にまとめた（Table 6）．本表は，横型プロセス機能展開表の行列を入れ替え，縦型プロセス機能展開表にし，直交表実験の結果を列に追記した表である．この時，表には，SN 比の情報だけでなく，各制御因子の水準を変えたときの感度やコストの変化も記した．我々は，この表をロバストエンジニアリング（RE）情報と呼んでいる［2］．

RE 情報を俯瞰すると，硝種によらず SN 比に効果のある制御因子や水準の方向を把握できるようになった．これにより，安定性として水準を固定したほうが良い制御因子や，そうでない制御因子が明確になり，次製品に展開可能な汎用性のある製造技術情報が蓄積された．

6 成　果

6.1. 直交表実験レスによる量産立ち上げ

硝種ごとの実験の目的と進め方を Table 7 に示す．RE 情報の要因効果を横展開することで，系統 γ, δ 内の硝種については，直交表実験を行わずに，RE 情報から量産の製造条

Table 6　系統δの縦型プロセス機能展開表と RE 情報

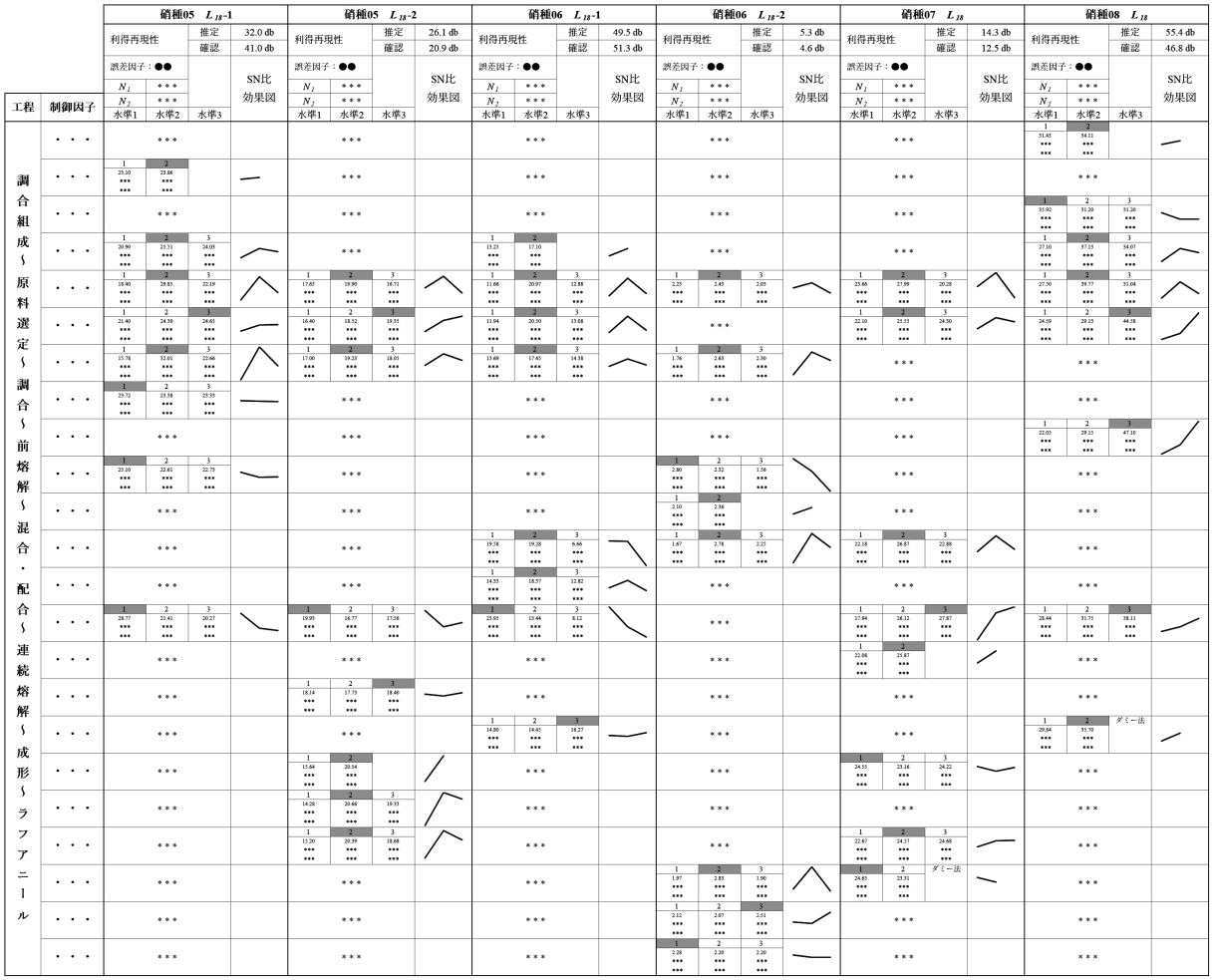

Table 7　硝種ごとの実験の目的と進め方

系統	硝種	目　的	直交表実験
γ	01	高透過率化	1 回
	02	高透過率化	2 回
	03	新規開発	1 回
	04	新規開発	レス
δ	05	高透過率化	2 回
	06	不良削減	2 回
	07	高透過率化	1 回
	08	新規開発	1 回
	09～11	新規開発	レス
	12	不良削減	レス
	13～16	高透過率化	レス

件を決定することができた．実際の評価では，はじめに，小規模実験で目的の性質が得られるか確認し，感度調整が必要な場合は，できるだけ SN 比を犠牲にせずに，小規模実験でチューニングした．次に，大規模な実験で問題なく量産できるか確認した．新規に開発した硝種であっても，RE 情報が蓄積されている系統であれば，直交表実験レスで

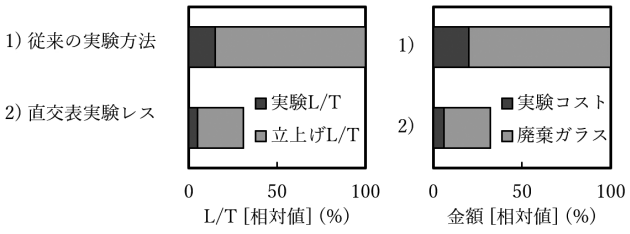

Fig. 11　L/T の短縮とコスト削減の効果

短期間の内に量産の製造条件を決定し，新硝種の垂直立ち上げが可能となった（硝種04, 09～11）.

6.2. リードタイム短縮とコスト削減

本研究の成果について，従来方法との比較を Fig. 11 に示す．実験リードタイム（L/T）が1/4になり，大規模実験から量産までの期間が1/3に短縮でき，実験費用も1/3に削減できた．その結果，実験に関わるエネルギーが CO_2 換算［7］で約35t/年の削減となり，さらに，不良の削減により廃棄物量が CO_2 換算で約 103 t/年の削減となった.

7 まとめ

本研究により，様々な硝種に展開可能な，量産再現性のある小規模実験方法を確立できた．その中で，我々が実施したプロセス機能展開表の活用方法を下記に示す．

(1) 広範囲の工程全体を顕在化し，検討すべき範囲を明確にする（システム分割）．
(2) 評価尺度と誤差因子を検討し，大規模な量産で再現性のある小規模実験を行う．
(3) 多硝種に展開した直交表実験の結果を，縦型プロセス機能展開表に整理し，固定すべき制御因子を明確にする（RE 情報の蓄積）．

この活用方法により，次製品に展開できる汎用性のある製造技術を確立できた．その結果，直交表実験レスで新硝種の垂直立ち上げを実現した．

謝　辞

本研究を進めるにあたり，ご指導頂いた元ニコンの関道子氏に感謝申し上げる．

引　用　文　献

[1] 泉谷徹郎，*光学ガラス*，共立出版，1984.
[2] 嘉指伸一，“プロセス機能展開表の活用とロバストエンジニアリング情報の活用による初期型不良の撲滅と立上げリードタイムの短縮，”*全国能率大会*，63, pp. B73-76, 2012.
[3] 嘉指伸一，“品質工学を実務で活用する「品質工学ステップ展開」，”*標準化と品質管理*，vol. 69, no. 9, pp. 57-69, 2016.
[4] 山根正之 他，*ガラス工学ハンドブック*，朝倉書店，2010.
[5] *光学ガラスの内部透過率の測定方法*，JOGIS 17: 2012.
[6] 田口玄一，*品質工学講座1 開発・設計段階の品質工学*，日本規格協会，1988.
[7] *温室効果ガス排出量算定・報告マニュアル*，Ver 4.0，環境省，経済産業省，2015, pp. II-32−II-33.
[8] 佐藤幸太，嘉指伸一，“プロセス機能展開表を活用した光学ガラスの溶解技術開発，”*品質工学*，vol. 29, no. 1, pp. 30-38, 2021.

佐藤幸太　Kota SATO
光ガラス株式会社
HIKARI GLASS CO., LTD.

嘉指伸一　Shinichi KAZASHI
嘉指技術品質研究所
KAZASHI Technological Quality Research

佐藤幸太
Kota SATO

嘉指伸一
Shinichi KAZASHI

Nikon Research Report Vol. 5
Published September 2023

NIKON CORPORATION